

Accepted by ApJ

Dynamical Mass Constraints on Low-Mass Pre–Main-Sequence Stellar Evolutionary Tracks: An Eclipsing Binary in Orion with a $1.0 M_{\odot}$ Primary and an $0.7 M_{\odot}$ Secondary¹

Keivan G. Stassun^{2,3,4}, Robert D. Mathieu⁴, Luiz Paulo Vaz⁵, Nicholas Stroud⁴, Frederick Vrba⁶

ABSTRACT

We report the discovery of a double-lined, spectroscopic, eclipsing binary in the Orion star-forming region. We analyze the system spectroscopically and photometrically to empirically determine precise, distance-independent masses, radii, effective temperatures, and luminosities for both components. The measured masses for the primary and secondary, accurate to $\sim 1\%$, are $1.01 M_{\odot}$ and $0.73 M_{\odot}$, respectively; thus the primary is a definitive pre–main-sequence solar analog, and the secondary is the lowest-mass star yet discovered among pre–main-sequence eclipsing binary systems. We use these fundamental measurements to test the predictions of pre–main-sequence stellar evolutionary tracks. None of the models we examined correctly predict the masses of the two components simultaneously, and we implicate differences between the theoretical and empirical effective temperature scales for this failing. All of the models predict the observed slope of the mass-radius relationship reasonably well, though the observations tend to favor models with low convection efficiencies. Indeed, considering our newly determined mass measurements together with other dynamical mass measurements of pre–main-sequence stars in the literature, as well as measurements of Li abundances in these stars, we show that the data strongly favor evolutionary models with inefficient convection in the stellar interior, even though such models cannot reproduce the properties of the present-day Sun.

Subject headings: stars: fundamental parameters — stars: pre–main-sequence — stars: low-mass, brown dwarfs — stars: binaries: eclipsing — stars: binaries: spectroscopic

²Visiting Astronomer, Cerro Tololo Inter-American Observatory and Kitt Peak National Observatory. CTIO and KPNO are operated by AURA, Inc. under contract to the National Science Foundation.

³Hubble Fellow

⁴Department of Astronomy, University of Wisconsin—Madison, Madison, WI 53706, and Department of Physics & Astronomy, Vanderbilt University, Nashville, TN 37235; keivan.stassun@vanderbilt.edu

⁵Departamento de Física, Universidade Federal de Minas Gerais, C.P. 702, 30.123-970, Belo Horizonte, MG, Brazil

⁶US Naval Observatory, Flagstaff Station, Flagstaff, AZ

¹Based on data collected with the Hobby-Eberly Telescope and the WIYN Telescope.

1. Introduction

Pre–main-sequence stellar evolutionary models are fundamental to our paradigm of star formation and early stellar evolution. These models are the means by which masses and ages are assigned to young stars and brown dwarfs, and are therefore central to our understanding of physical processes that depend, directly or indirectly, on knowledge of stellar masses and ages. Indeed, pre–main-sequence (PMS) stellar evolutionary models touch upon the most basic questions in star formation research: the nature and origin of the initial mass function; the timescale for circumstellar disk evolution and planet formation; and the initial distribution of stellar angular momentum, its evolution in time, and the dependence of that evolution on stellar mass, accretion, and other mass-dependent properties. Thus, the absolute calibration of PMS evolutionary models with respect to stellar mass is of foundational importance to star formation research.

Empirical mass determinations exist in the literature for 15 individual PMS stars (Popper 1980; Andersen 1991; Casey et al. 1998; Simon, Dutrey, & Guilloteau 2000; Covino et al. 2000; Steffen et al. 2001; Alencar et al. 2003), with only 6 of these in the mass domain of $1 M_{\odot}$ or below. Moreover, many of these measurements, while of high precision, potentially suffer from systematic errors (primarily distance uncertainties) that limit their accuracy. Indeed, there is no PMS star with $M < 1 M_{\odot}$ whose mass has been measured with an accuracy of better than a few percent.

Consequently, the absolute mass calibration of theoretical PMS evolutionary tracks remains weakly constrained by observations. The dearth of accurate measurements below $1 M_{\odot}$ is particularly salient because low-mass stars dominate studies of young stellar populations, and it is in this mass domain that key, outstanding questions remain with respect to, e.g., the nature of the initial mass function (Hillenbrand 1997; Muench et al. 2002) and the evolution of stellar angular momentum (SMMV; Herbst et al. 2002; Rebull 2001).

Eclipsing binary stars provide a uniquely powerful means of determining absolute stellar masses because the mass determinations are distance-independent. Eclipsing binaries also yield direct measurement of the stellar radii, permitting the determination of stellar luminosities that are also distance independent. To date, only four eclipsing binaries with PMS components have been reported in the literature (Andersen 1991; Popper 1980; Casey et al. 1998; Covino et al. 2000).

Here we report the discovery of a previously unknown, double-lined, spectroscopic, eclipsing binary system in the Orion star-forming region, V1174 Ori. We combine time-series photometry with high-resolution spectroscopy to determine all of the fundamental physical properties of the system and of its stellar components. We then use these measurements to test the predictions of a variety of PMS stellar evolutionary models.

We begin by describing the discovery of V1174 Ori and its identification as a PMS eclipsing binary in §2. In §3, we present our photometric and spectroscopic observations and the methods used in their reduction. We analyze these observations in §4 to determine the system ephemeris and to derive a precise double-lined orbit solution, providing absolute stellar masses. We conduct

a thorough spectroscopic analysis that includes determination of the stellar rotational velocities, measurement of the primary-to-secondary flux ratio, spectral classification and determination of effective temperatures, measurement of Li abundances, and measurement of the equivalent width of H α emission. We also present a full analysis of our multi-band time-series photometry using synthetic light-curve fitting to determine precise, absolute stellar dimensions. The results of our analysis are presented in §5, including an independent determination of the distance to V1174 Ori.

In §6 we use our empirically determined stellar masses, radii, effective temperatures, and luminosities to test a variety of PMS stellar evolutionary tracks possessing a variety of characteristics, including different atmosphere models and treatment of convection. We assess the performance of the theoretical models both against the components of V1174 Ori alone as well as against the ensemble of all PMS stars with empirical mass determinations in the literature. We consider how the tracks compare quantitatively to the data in both high- and low-mass regimes, in both binary and single systems, and in both the H-R diagram and mass-radius observational planes. Moreover, we examine the general behavior of the tracks to suggest, in qualitative terms, how their performance against the data might be improved.

In addition, we assay the ensemble of empirical mass determinations independent of the models to explore the degree of internal consistency in the data themselves, and we show how Li abundances can be used in some cases to resolve apparent contradictions. Finally, we discuss more general insights that can be gleaned from the Li abundances, arguing that the data strongly favor models with inefficient convection in the stellar interior during the PMS stage of evolution, even though such models cannot reproduce the properties of the present-day Sun. We present a summary of our conclusions in §7.

2. Discovery

Here we describe the discovery of V1174 Ori as a PMS eclipsing binary system. Its position is $\alpha = 05:34:27.85$, $\delta = -05:41:37.8$ (J2000.0).

2.1. Data from the Literature

V1174 Ori has been included in a number of previous surveys of stars in the vicinity of the Orion Nebula Cluster (ONC), dating back to the catalog of Parenago (1954) (star # 1478). The General Catalog of Variable Stars, whose designation we use in this paper, reports a range of 1.1 mag (in the photographic system) between its high and low states.

More recently, the ROSAT observatory included V1174 Ori (designation ROS-ORI 166) in a deep PSPC pointing centered on the Trapezium region. The analysis of these data by Geier, Wendker, & Wisotzki (1995) assigns a net of 75 X-ray photons to V1174 Ori, for a count rate

of 17.02 cts/ks. This corresponds to an X-ray luminosity of $L_X \approx 1 \times 10^{30}$ erg/s in the ROSAT bandpass (0.07 to 2.4 keV), assuming the ONC distance to V1174 Ori of 470 pc (e.g. Genzel et al. (1981)). V1174 Ori has not been included in any of the *Chandra* observations of the ONC currently in the public archive, but this X-ray luminosity is fairly typical among the PMS stars that have been observed by *Chandra* (e.g. Feigelson et al. (2002)).

V1174 Ori was observed in the *K*-band survey of the Orion A cloud by Ali & Depoy (1995) (# 2176 in their catalog), but their reported *K*-band magnitude of 9.00 is at the bright limit of their survey, making this measurement suspect. More recently, Carpenter, Hillenbrand, & Skrutskie (2001) presented *JHK* light curves of V1174 Ori (star number 4008 in their catalog), as part of their analysis of time-series photometry of the Orion star-forming region, conducted as an extension of the 2MASS project⁷. Their light curves show rms scatters of 0.08–0.09 mag. In addition to low-level variability, their light curves display evidence for a possible eclipse event in the form of a single observation (seen in all three filters) that is 0.3–0.4 mag dimmer than the mean brightness level.

Finally, V1174 Ori was included in the study of Rebull et al. (2000) (# 1-665 in their catalog), whose *UVI* photometry places V1174 Ori on the locus of Orion PMS stars in the $(U - V)$ vs. $(V - I)$ color-magnitude diagram. They report a spectral type for V1174 Ori of M0 on the basis of low-resolution spectroscopy, but derive extinctions of $A_V = -0.50$ and $A_I = -0.31$, indicating potential problems with the spectral classification or photometry. While V1174 Ori was included in the region covered by the time-series study of Rebull (2001), they do not report it as a periodic variable. V1174 Ori was in eclipse during at least 7 of the 30 nights covered by their observations (assuming the ephemeris we adopt in §4), but with only one observation per night their light curves were presumably too sparse to detect periodic behavior (if they detected the eclipses at all).

2.2. Identification as a PMS Double-Lined Eclipsing Binary

We first identified V1174 Ori as a candidate eclipsing binary from an *I*-band light curve obtained by us in 1994 December as part of a photometric study of stellar rotation in the ONC (Stassun et al. 1999; hereinafter SMMV). The discovery light curve was by itself very compelling, showing eclipse-like variability with a period of ≈ 2.63 days.

V1174 Ori was also included in several pointings during our spectroscopic survey of the region with the WIYN⁸ multi-object spectrograph, which showed V1174 Ori to have strong Li absorption (an indicator of stellar youth) and revealed it to be a single-lined spectroscopic binary. We confirmed the spectroscopic presence of the secondary in a spectrum kindly obtained by G. Basri with the Keck HIRES spectrograph, which also clearly revealed the presence of Li absorption due to the

⁷See <http://www.ipac.caltech.edu/2mass> for information about 2MASS

⁸The WIYN Observatory is a joint facility of the University of Wisconsin-Madison, Indiana University, Yale University, and the National Optical Astronomy Observatories.

secondary (Fig. 1). This spectrum also allowed us to determine that the primary was of roughly mid-K spectral type.

3. Observations and Data Reduction

Having identified V1174 Ori as a PMS eclipsing binary and double-lined spectroscopic binary, we obtained multiple high-S/N, high-resolution spectra with which to determine a precise, double-lined orbit solution. We also obtained high-precision, high-cadence light curves at multiple wavelengths in order to (a) firmly establish the system ephemeris, and to (b) determine, via light-curve synthesis and modeling, such parameters as the orbital inclination, component radii, and ratio of component effective temperatures. The one remaining piece of information needed to fully establish all system parameters is the effective temperature of one of the components, a datum also provided by our high-resolution spectroscopy.

Here we present the photometric and spectroscopic data we obtained, and describe the procedures we employed in their reduction.

3.1. Photometry

We observed V1174 Ori photometrically with CCDs at 1m-class telescopes at 6 separate epochs spaced over 8 years. Table 1 summarizes the time-series photometry we obtained. The individual measurements are available electronically and are shown in Figs. 2, 4, and 6.

All CCD data were processed in the manner described in SMMV. Briefly, we reduced our CCD frames using the IRAF⁹ CCDRED or XCCDRED (for CTIO quad-readout data) packages, and performed aperture photometry on all stars in the field of view using the IRAF APPHOT package. We then applied an algorithm similar to that of Honeycutt (1992) to our raw light curves to remove non-cosmic frame-to-frame photometric variations (due to changes in, e.g., seeing, sky brightness, atmospheric transparency). In all cases, the resulting photometric precision in the light curves of V1174 Ori is limited by systematics (flat-fielding, PSF variations, etc.) at the ~ 0.01 mag level, which we determine from inspection of non-variable stars in the field of comparable brightness.

In addition to these differential time-series observations, we obtained calibrated *BVI* photometry of V1174 Ori on 1995 Feb 02 at the USNO 1m telescope. These data were obtained out of eclipse, at orbital phase 0.35, based on the ephemeris presented in §4.1. Calibrated *UVI* photometry of V1174 Ori has been reported by Rebull et al. (2000), and Carpenter, Hillenbrand, & Skrutskie (2001) report *JHK* measurements. These measurements are summarized in Table 2.

⁹IRAF is distributed by the National Optical Astronomy Observatories, which is operated by the Association of Universities for Research in Astronomy, Inc., under cooperative agreement with the National Science Foundation.

Rebull et al. (2000) do not report the precise times of their observations. However, the $V - I$ color reported by them is identical to that measured by us, which leads us to believe that their observations were also obtained out of eclipse. Carpenter, Hillenbrand, & Skrutskie (2001) report mean JHK magnitudes and colors, averaged over all of their observations which span 36 days (excluding the two non-contiguous measurements obtained in 1998 Mar and 2000 Feb). The J magnitude we adopt is the mean of their non-eclipse observations. The $J - H$ and $H - K$ colors do not show significant variations in their observations and so we do not adjust the values reported by those authors.

3.2. Spectroscopy

In order to derive a precise, double-lined orbit solution for V1174 Ori, we obtained 15 high S/N observations in queue observing mode with the High Resolution Spectrograph (HRS) on the Hobby Eberly Telescope¹⁰ (HET) on 15 different nights between 2001 Nov 22 and 2002 Feb 23. The spectrograph setup we used yielded a resolving power of $R \approx 30000$, with wavelength coverage from 5095Å to 8860Å, and centered at 6948Å. The 51 echelle orders in each spectrum are imaged onto two CCDs, with the “blue” chip imaging the 32 orders from 5095Å to 6803Å and the “red” chip imaging the remainder. The spectrograph was also set up with a single sky fiber so that simultaneous sky spectra could be obtained with each observation. The CCD images were binned on readout such that a spectral resolution element corresponds to approximately 3 pixels in the extracted spectra.

The exposure times were initially $3 \times 600 = 1800$ sec, and later increased to $3 \times 800 = 2400$ sec, and we combined the individual exposures in each set with cosmic-ray rejection. Each observation of V1174 Ori was bracketed by an observation of a ThAr lamp. In addition, all but one observation was accompanied by an observation of a bright radial-velocity standard star (typically obtained shortly after the V1174 Ori exposure) in order to closely monitor and correct for instrumental drifts in the radial velocities.

In addition, we obtained a single, very high S/N (~ 250) observation of a late-type radial-velocity standard star for use as a radial-velocity template in our cross-correlation analysis (§4.2.2). Once we had established the approximate spectral types of the components of V1174 Ori (§4.3), we also obtained single observations of two appropriate spectral-type standard stars, of types K3 and K7¹¹. Table 3 summarizes our spectroscopic observations with HET HRS.

¹⁰The Hobby-Eberly Telescope is operated by McDonald Observatory on behalf of The University of Texas at Austin, the Pennsylvania State University, Stanford University, Ludwig-Maximilians-Universität München, and Georg-August-Universität Göttingen. The observations described here were obtained through community access made possible by NOAO.

¹¹More careful analysis of the V1174 Ori spectra after the observations were obtained indicates that the components of V1174 Ori have spectral types of K4.5 and \sim M1.5 (see §4.3.3), but this does not significantly affect our analysis.

Table 1. Photometric time-series observations of V1174 Ori

UT Dates	N (nights)	Range of Julian Dates (2400000+)	Observatory	Filter	# of obs.	Ref.
1994 Dec 11–27	16	49698.340–49714.491	KPNO 0.9m, USNO 1m, Wise 1m	I_C	128	SMMV
2001 Jan 20–27	8	51929.588–51936.775	CTIO 0.9m	I_C	152	this study
		51929.608–51936.768		V	144	this study
		51929.590–51936.776		Str. y	158	this study
		51929.594–51936.783		Str. b	154	this study
		51929.623–51936.735		Str. v	130	this study
2001 Jan 31	1	51940.591–51940.819	USNO 1m	I_C	20	this study
		51940.589–51940.817		V	20	this study
2001 Nov 14–24	9	52227.746–52237.996	WIYN 0.9m	I_C	78	this study
2002 Nov 17–26	10	52595.745–52605.000		I_C	110	this study
		52595.802–52605.004		V	96	this study
		52595.806–52604.984		B	96	this study
2002 Dec 05–16	11	52613.810–52624.946		I_C	24	this study

Table 2. Calibrated photometry of V1174 Ori

Filter(s)	Mag./Color observed	Mag./Color calculated ^a	UT Date(s)	Ref.
V	13.95 ± 0.03	13.95	1995 Feb 02	1
$B - V$	1.25 ± 0.02	1.24		1
$V - I$	1.62 ± 0.02	1.48		1
	1.61 ± 0.02		1998 Jan	2
$U - V$	2.22 ± 0.02	2.33		2
J^1	11.22 ± 0.05	11.52	2000 Mar 04 – Apr 08 ²	3
$J - H$	0.65 ± 0.02	0.65		3
$H - K$	0.19 ± 0.03	0.14		3

References. — 1: this study, 2: Rebull et al. (2000), 3: Carpenter, Hillenbrand, & Skrutskie (2001)

^aAssuming main-sequence colors, bolometric corrections, and $R_V = 3.12$. See §5.1.

¹Value adjusted from that reported in Carpenter, Hillenbrand, & Skrutskie (2001), in order to account for eclipses.

²Contiguous portion of light curve only.

Table 3. Log of HET HRS Observations

#	UT Date	HJD ¹	Object	Exp. Time (s)	S/N ²	Comments
0	2001 Oct 29	2212.74347	HD 18884	30	245	R.V. template, SpT = M2 III
1	2001 Nov 22	2235.85217	V1174 Ori	1800	85	
		2235.87681	HD 26162	5	120	R.V. standard, SpT = K2 III
2	2001 Nov 23	2236.84827	V1174 Ori	1800	80	
		2236.89321	HD 26162	15	145	
3	2001 Dec 10	2253.80559	V1174 Ori	1800	60	
		2253.82748	HD 26162	10	85	
4	2001 Dec 18	2261.78887	V1174 Ori	1800	40	
		2261.80695	HD 26162	10	90	
5	2001 Dec 21	2264.77976	V1174 Ori	1800	80	
		2264.79712	HD 26162	10	95	
6	2001 Dec 22	2265.76822	V1174 Ori	1800	75	
		2265.83415	HD 26162	10	95	
7	2001 Dec 23	2266.76687	V1174 Ori	1800	105	
		2266.81776	HD 26162	10	120	
8	2002 Jan 26	2300.67336	V1174 Ori	2400	125	
9	2002 Jan 27	2301.66941	V1174 Ori	2400	95	
		2301.72972	HD 26162	10	100	
10	2002 Jan 28	2302.66839	V1174 Ori	2400	105	
		2302.72798	HD 26162	10	140	
11	2002 Feb 07	2312.64124	V1174 Ori	2400	100	
		2312.70694	HD 26162	10	105	
12	2002 Feb 09	2314.63298	V1174 Ori	2400	120	
		2314.69301	HD 26162	10	160	
13	2002 Feb 13	2318.63282	V1174 Ori	2400	95	
		2318.68518	HD 26162	10	130	
14	2002 Feb 21	2326.61211	V1174 Ori	2400	90	
		2326.62791	HD 26162	10	115	
15	2002 Feb 23	2328.60823	V1174 Ori	1800	100	
		2328.62179	HD 26162	10	110	
16	2002 Mar 07	2340.93213	HD 110463	180	140	SpT standard, SpT = K3 V
		2340.64503	HD 237903	240	160	SpT standard, SpT = K7 V

¹ Heliocentric Julian Date (2450000+)² Signal-to-noise is per 3-pixel resolution element, measured near 6500Å.

All spectra were processed with the IRAF `CCDPROC` and `ECHELLE` packages. The steps involved in producing the final spectra include bias subtraction, flat-fielding, bad-column interpolation, order tracing (for both object and sky apertures), sky subtraction, wavelength calibration, and heliocentric velocity correction. Extraction of the spectra from the raw data was not straightforward, particularly with respect to order tracing which required a high degree of manual intervention. The orders are highly angled on the CCD, have flat-topped profiles in the cross-dispersion direction, and are separated from the sky orders by only a few pixels. We thus encountered difficulties with the automated order-finding and tracing frequently “skipping” between the object and sky apertures. However, we found that these problems could be circumvented manually.

ThAr arc spectra were extracted similarly. We found that relatively high-order polynomials both along and across the orders were required to provide a good mapping between pixel, order number, and wavelength. In the end we adopted third-order and seventh-order polynomial fits along and across the orders, respectively. The wavelength solutions were applied to the object spectra by taking an average of the ThAr spectra taken before and after the object spectra, weighted by their proximity in time to the object spectra.

Heliocentric velocity and date corrections were computed via the IRAF `RV` package. We carefully assigned mid-exposure observation times to each combined spectrum, taking into account the flux levels of the 3 sub-exposures (which occasionally differed from one another) and their time spacing relative to one another.

As ours was the first community program to use HET HRS, we unfortunately encountered an unforeseen problem that rendered the “red” orders in our spectra unusable. The “red” HRS CCD in use at the time of our observations suffers from severe fringing, which would normally be removed by a spectrum of a bright continuum source such as an internal lamp. However, in the case of the HRS, the fringing pattern produced by the internal flat-field calibration lamp is different from the pattern present in the data. This is in part due to the fact that a different fiber is used for calibration purposes, which results in the flat-field beam having a different f -ratio as compared to the science-object beam (M. Shetrone, priv. comm.). Thus in our spectroscopic analyses we use only the orders on the “blue” CCD, which show no such fringing problems.

4. Analysis

4.1. Eclipse timings: System ephemeris

We use eclipse timing measurements from our photometric light curves (§3.1) to determine a precise period and ephemeris for V1174 Ori. Our I -band data, which span a total of 2927 days, include 7 primary and 5 secondary eclipses. Some of these eclipses were also observed in other filters, providing additional (though not fully independent) eclipse timing information. We measure the time of each eclipse minimum by fitting a gaussian to the points in the light curve in and around

the eclipse. These eclipse timings and their uncertainties are reported in Table 4.

We searched the combined I -band lightcurves for a period via the Phase-Dispersion Minimization (PDM) technique (Stellingwerf 1978), and found a best period of 2.61156 days. However, visual inspection of the combined data folded on this period revealed that the algorithm had chosen a beat period whereby the primary eclipses from the 2001 data were overlaid on the secondary eclipses from the 1994 data. Thus we refined the period by searching our radial-velocity measurements (§4.2.2) for periods near this value. This yielded a best period of 2.63469 ± 0.00012 days. A final visual inspection of the light curve folded on this period suggested a small manual refinement to $P = 2.634727 \pm 0.000004$ days.

In Fig. 8 we show the $O - C$ phase residuals of the eclipse timings from Table 4 using this period. To show the residuals of the secondary eclipse together with those of the primary, we have subtracted 0.5 phase from the secondary residuals, which assumes a circular orbit. These residuals have an r.m.s. of 0.0015 in phase (5.5 min), and show no trends over the 2900-day span (some 1100 cycles) of the data. While there appears to be a weak effect in the Jan 2001 data for the primary eclipse ($O - C$) values to be systematically negative and for the secondary eclipse ($O - C$) values to be systematically positive, it should be borne in mind that the eclipse timings from the different filters in Jan 2001 are not truly independent, as these light curves share a common sampling pattern. The eclipse timings are therefore consistent with the assumption of a circular orbit.

We thus adopt the following ephemeris for the remainder of our analysis:

$$\text{Min I : HJD } 2,449,703.7504(15) + 2.634727(4)E,$$

where E is the epoch number, and the zero-point corresponds to primary eclipse (i.e. the deeper minimum).

4.2. Radial velocities and orbit solution

We use our HET HRS observations (Table 3) to measure precise radial velocities for both components of the V1174 Ori binary. Here we describe our procedure for measuring radial velocities, and discuss our assessment of potential systematic effects that may degrade the accuracy of the masses that we derive from them.

4.2.1. Radial velocities

We measure radial velocities by cross-correlating each V1174 Ori spectrum with a high-S/N spectrum of the radial-velocity standard HD 18884 (see Table 3), for which we adopt the heliocentric radial velocity of -26.1 km s^{-1} as determined by Udry et al. (1999), whose long-term monitoring of this star shows it to be non-variable to a precision level of 0.3 km/s over nearly 300 observations.

Table 4. Times of Eclipse Minima

UT Date	HJD ¹	Filter	Eclipse type	$O-C$ (phase)
1994 Dec 11	49698.4867 ± 0.0102	I_C	Primary	0.0022
1994 Dec 13	49699.7974 ± 0.0193	I_C	Secondary	−0.0004
1994 Dec 15	49702.4341 ± 0.0027	I_C	Secondary	0.0004
1994 Dec 17	49703.7433 ± 0.0010	I_C	Primary	−0.0027
1994 Dec 21	49707.7129 ± 0.0158	I_C	Secondary	0.0040
1994 Dec 27	49714.2850 ± 0.0011	I_C	Primary	−0.0016
2001 Jan 23	51932.7275 ± 0.0004	I_C	Primary	−0.0007
	51932.7284 ± 0.0003	V		−0.0004
	51932.7274 ± 0.0003	y		−0.0008
	51932.7276 ± 0.0002	b		−0.0007
	51932.7278 ± 0.0003	v		−0.0006
	51932.72774 ± 0.00020	mean ^a		−0.00065
2001 Jan 27	51936.6835 ± 0.0009	I_C	Secondary	0.0008
	51936.6833 ± 0.0014	V		0.0007
	51936.6859 ± 0.0013	y		0.0017
	51936.6830 ± 0.0011	b		0.0006
	51936.6775 ± 0.0026	v		−0.0015
	51936.68264 ± 0.00155	mean ^a		0.00042
2001 Jan 31	51940.6324 ± 0.0004	I_C	Primary	−0.0005
	51940.6331 ± 0.0003	V		−0.0002
	51940.63275 ± 0.00049	mean ^a		−0.00033
2001 Nov 14	52227.8162 ± 0.0011	I_C	Primary	−0.0010
2001 Nov 18	52231.7679 ± 0.0032	I_C	Secondary	−0.0012
2001 Nov 22	52235.7250 ± 0.0026	I_C	Primary	0.0007

¹Heliocentric Julian Date (2400000+)

^aMean of the measurements obtained from the individual filters.

Note. — $O-C$ values are with respect to the ephemeris for primary minimum HJD 2,449,703.7504 + 2.634727 E (see text).

We chose this late-type (M2) template in the hopes of maximizing the cross-correlation peak of the faint, late-type secondary star.

We cross-correlate each of the 32 spectral orders in a given spectrum separately, and measure the centroid of the primary and secondary star peaks (see Fig. 9a). For each spectrum we thus in principle have 32 separate (but not independent) radial-velocity determinations for each of the primary and secondary. In practice, however, some orders consistently produce poor radial velocities, typically due to the presence of very broad lines (e.g. the Na D lines) which result in cross-correlation peaks that do not lend themselves well to centroiding. In addition, we were unable to securely identify the peak corresponding to the secondary star in most orders, due to other low-level structure in the cross-correlation function. To be conservative, we thus typically only accepted a few very good orders, orders where the spectral features of the secondary are particularly strong. Finally, we found that it was necessary to avoid spectral regions with strong nebular emission, which often subtracted poorly. By carefully selecting the spectral regions to be used in each order for each spectrum, we were able to maximize the number of orders yielding radial velocities.

For the secondary star, we use all orders that unambiguously show a secondary peak to define a mean radial velocity in each spectrum. With the primary star, for which most of the spectral orders yield a velocity measurement, we can be even more discriminating to maximize our precision. As shown in Fig. 9b, the scatter in the primary radial velocities produced by the different spectral orders is a function of correlation peak height; empirically, we find that the scatter is smallest among spectral orders that yield correlation peak heights above a certain threshold value, typically around 0.6 (as in the example of Fig. 9b). We thus determine primary radial velocities from each spectrum by taking the mean of only those spectral orders with correlation peak heights greater than this threshold. Finally, we further refined the primary velocities by iteratively excluding orders that deviated by greater than 2σ from the mean, which typically resulted in the rejection of at most one order per spectrum.

In Table 5 we report the primary and secondary radial velocities that we derive in this manner. In addition to the mean velocities adopted for each star, we give the number of spectral orders participating in defining the mean. In addition, we report the $O - C$ velocity residuals compared to our best-fit orbit solution (see below) for each of the primary and secondary velocities. The uncertainty reported with each velocity is simply the standard deviation of the mean. These uncertainties, which average around 0.3 km/s for the primary and 1.4 km/s for the secondary, thus represent an estimate of our internal errors only; we discuss instrumental and systematic errors in §§4.2.3 and 4.2.4.

Some of our observations were taken at orbital phases near eclipse, resulting in blended cross-correlation peaks that were difficult to separate securely. Indeed, the velocity centroids in these cases can be adversely affected for at least a couple of reasons. Cross-correlation peaks in close proximity to one another can suffer from “peak pulling”, whereby blending of the two components can cause apparent shifts in the peak centroids. In addition, partial blocking of the stellar disc

of one star by the other causes the stellar line profiles of the blocked star to become asymmetric, narrower, and shifted with respect to the center-of-mass velocity. For our orbit solution analysis we thus discarded measurements obtained within 0.05 phase of either eclipse, thereby ensuring that the correlation peaks would be reasonably well separated and that occultation effects would not be a concern. The only exception to this is the spectrum obtained on UT 2002 Feb 21, which occurs at the phase where the secondary is almost completely eclipsed by the primary, so that the secondary spectrum is practically not present in the observed light.

The presence of spots on the stellar surfaces can also introduce distortions that affect the observed radial velocities. The importance of this effect for our observations can be evaluated from the light curve solutions discussed below, which include the effects of spots. Our model fits to the light curves obtained in January 2001 show that the effect is rather small. The theoretical radial-velocity distortions due both to stellar occultation (the Schlesinger-Rossiter effect; Rossiter (1924); Schlesinger (1909)) and the presence of surface spots are shown in Fig. 10. For the primary star, the radial velocity distortions due to spots are undetectable at the precision of our study, having an amplitude of at most 0.2 km/s, and less at most orbital phases. For the secondary star, the distortions are more pronounced, but still have an amplitude no larger than 1 km/s, and only at certain phases. As the light curve data were not obtained simultaneously with the radial velocity data, we do not correct the observed velocities for these distortions, noting again that the effect is in any case probably negligible.

4.2.2. *Orbit solution*

We determined an orbit solution to the radial-velocity measurements in Table 5 by applying a least-squares fit simultaneously to the primary and secondary velocities. The orbit solution involves seven parameters: the mass ratio, q ; the orbital period, P ; the semi-amplitudes of the primary and secondary velocities, K_A and K_B ; the eccentricity, e ; the center-of-mass velocity, γ ; and the time of primary minimum, T_0 .

With the system ephemeris determined precisely from the eclipse timing data (see §4.1), we chose to fix the values of P and T_0 to those determined photometrically, and forced the orbit to be exactly circular (i.e. $e \equiv 0$). The assumption of circularity is corroborated by the eclipse timings analysis (§4.1), and is certainly expected for a short-period binary such as this. In any case, we did try a solution with e as a free parameter, but found a best-fit value that was statistically insignificantly different from zero.

Using all of the radial velocities resulted in a fit with r.m.s. residuals for the primary and secondary of $\sigma_A = 0.66$ km/s and $\sigma_B = 2.55$ km/s, respectively. However, the measurement of the secondary's velocity from the UT 2001 Dec 18 spectrum showed a residual of -5.75 km/s, considerably larger than the other measurements. Indeed, a close look at the distribution of the secondary residuals revealed this measurement to be a clear outlier; excluding this measurement

yielded a fit with $\sigma_B = 1.41$ km/s, consistent with the internal errors of the measurements.

We carefully re-examined (and even reprocessed) the spectrum of UT 2001 Dec 18 and the cross-correlation functions to see if we could discern any reasons for the large discrepancy of this measurement. The primary's measurement is not obviously discrepant, and neither is the velocity of the standard star observed on this night (see §4.2.4). We note however that this spectrum does have the poorest S/N of all our HET HRS observations (Table 5). Interestingly, our light curve analysis (§4.4) suggests that spots might be significant near the orbital phase of this measurement (see Fig. 10).

In Table 6 we present the orbital parameters of V1174 Ori resulting from our best-fit orbit solution, and display this solution along with the radial-velocity measurements in Fig. 11.

4.2.3. *Instrumental stability*

Our spectroscopic observations allow us to determine an orbit solution with high precision, that in turn results in very precise ($\sim 1\%$) determination of the stellar masses (Table 6). As noted above, the residuals of the radial velocity measurements about the best-fit orbit solution are $\sigma_A = 0.66$ km s $^{-1}$ and $\sigma_B = 1.41$ km s $^{-1}$ for the primary and secondary, respectively. Evidently, the instrumental stability of the HET HRS is at least as good as 0.65 km s $^{-1}$.

To assess the instrumental stability more carefully, we analyzed our observations of the radial-velocity standard star HD 26162, which was observed along with V1174 Ori, in the same way as our V1174 Ori observations. Specifically, we cross-correlated each HD 26162 spectrum against the same radial-velocity template (HD 18884) that we used to derive the V1174 Ori velocities. The results are tabulated in Table 7 and shown graphically in Fig. 12.

The velocity deviations of HD 26162 relative to its published velocity of 24.8 km s $^{-1}$ (Udry et al. 1999) reveal a high level of stability of the HET HRS system over the 90-day timescale spanned by our observations. As Fig. 12 shows, the system does exhibit low-level, secular drifts, but the dispersion of these drifts is small. The deviations have an rms of 0.52 km s $^{-1}$ when we consider all of the nights on which V1174 Ori was observed, and an rms of 0.26 km s $^{-1}$ when we consider only those nights used in our orbit solution¹².

This rms of 0.26 km s $^{-1}$ is only about 1/2 of the rms residuals in our orbit solution fit to the primary velocities (0.65 km s $^{-1}$), and about 1/5 of the secondary (1.41 km s $^{-1}$). Evidently, some other source of measurement uncertainty dominates the errors in the radial velocity measurements of V1174 Ori. These could include: the lower S/N of the V1174 Ori spectra as compared to the HD 26162 spectra (Table 3), particularly for the secondary star; the double-peaked nature of the

¹²The lower rms of this subset of the radial-velocity measurements could be due to chance, given the apparently non-random nature of the deviations shown in Fig. 12.

Table 5. Radial velocities of V1174 Ori

# ^a	UT Date	HJD ^b	Phase	R.V. _P (km/s)	(O–C) _P (km/s)	R.V. _S (km/s)	(O–C) _S (km/s)	N _P	N _S
2	2001 Nov 23	2236.84827	0.427	-9.87 ± 0.44	-0.14	71.48 ± 1.56	-2.16	11	2
3	2001 Dec 10	2253.80559	0.863	83.44 ± 0.27	0.02	12	0
4	2001 Dec 18	2261.78887	0.893	72.91 ± 0.19	0.04	-46.57 ± 1.23	-5.75^c	11	3
6	2001 Dec 22	2265.76822	0.404	-19.90 ± 0.32	-0.14	88.17 ± 1.29	0.68	15	6
7	2001 Dec 23	2266.76687	0.783	101.81 ± 0.34	0.73	-80.36 ± 1.29	-0.91	15	7
8	2002 Jan 26	2300.67336	0.652	88.81 ± 0.22	-0.57	-62.39 ± 1.43	0.89	17	2
10	2002 Jan 28	2302.66839	0.409	-16.27 ± 0.23	1.31	86.28 ± 1.91	1.81	20	3
11	2002 Feb 07	2312.64124	0.194	-48.06 ± 0.24	-0.87	126.16 ± 1.29	0.77	17	3
12	2002 Feb 09	2314.63298	0.950	48.14 ± 0.30	-0.73	-5.87 ± 0.98	1.45	17	2
14	2002 Feb 21	2326.61211	0.497	23.23 ± 0.29	-0.34	20	0
15	2002 Feb 23	2328.60823	0.254	-52.17 ± 0.27	0.30	131.84 ± 1.36	-0.85	17	8

^aSee Table 3.

^bHeliocentric Julian Date (2450000+)

^cMeasurement discarded in preferred solution (see text).

Table 6. Results of V1174 Ori orbit solution

Parameter	Value
P (d)	2.634727 ± 0.000004
σ_A (km s ⁻¹)	0.66
σ_B (km s ⁻¹)	1.41
q	0.7238 ± 0.0057
e	0 ^a
γ (km s ⁻¹)	25.27 ± 0.19
K_A (km s ⁻¹)	77.75 ± 0.29
K_B (km s ⁻¹)	107.41 ± 0.67
$a \sin i$ (R _⊕)	9.638 ± 0.041
$M_A \sin^3 i$ (M _⊕)	1.005 ± 0.015
$M_B \sin^3 i$ (M _⊕)	0.728 ± 0.008

^aAdopted.

V1174 Ori cross-correlation functions; differences in the track length of the V1174 Ori observations as compared to the HD 26162 observations (1800 sec vs. 10 sec); a source of astrophysical noise (e.g. surface activity such as spots, flares, etc.); and/or the presence of an unseen tertiary companion (see §5.1). In any case, instrumental stability does not appear to be the dominant source of uncertainty in our radial velocity measurements.

4.2.4. Systematic errors

For this experiment, where the primary goal is to determine *accurate* stellar dimensions for comparison to stellar evolutionary models, it is critical that we ascertain the extent to which systematic effects may limit the accuracy of the absolute stellar dimensions that we determine.

The semi-amplitudes of the primary and secondary velocities (K_A and K_B) are the parameters from the spectroscopic orbit solution that directly determine the stellar masses, so the masses are directly sensitive to systematics in these quantities. One possible source of systematic error in these quantities is spectral-type mismatch between V1174 Ori and the radial-velocity template.

There is in fact some evidence for a systematic offset of the secondary velocities relative to the primary. As Fig. 12a shows, the velocities of the radial-velocity standard HD 26162 show a median velocity in our observations that is 0.36 km/s larger than the published value. We speculate that this offset is due to the fact that HD 26162 has an earlier spectral type (SpT = K2 III) than the radial-velocity template star (SpT = M2 III). Our best estimate for the spectral types of the components of V1174 Ori are K4.5 and M1.5 (see §4.3.3), so a similar systematic shift might be expected between the measured velocities for the two components of V1174 Ori, leading to systematic errors in the radial velocity semi-amplitudes.

We tried an orbit solution where we allowed for an arbitrary systematic offset between the primary and secondary velocities to be fit. We find a best-fit value of 0.35 ± 0.55 km s⁻¹ for the offset, which is interesting in its similarity to the offset of 0.36 km s⁻¹ we find above. Including this free parameter and its uncertainty results in slightly different stellar masses than those listed in Table 6, and with slightly larger uncertainties: $M_A \sin^3 i = 1.004 \pm 0.016$ M_⊙ and $M_B \sin^3 i = 0.727 \pm 0.009$ M_⊙. Thus, while our orbit solution formally allows for an offset of order 1 km s⁻¹ at the 2σ level, it is not statistically significant and its effect on the final uncertainties on the derived stellar masses is very small. For our subsequent analyses and discussion, we adopt the orbit solution provided in Table 6.

4.3. Spectral analysis

Having determined precise dynamical masses from our spectroscopic orbit solution, we now require stellar radii and effective temperatures for a complete analysis of the V1174 Ori system

and for comparison with PMS stellar evolutionary tracks. Our light curve analysis (§4.4) provides precise values for the radii, the inclination, and the *ratio* of effective temperatures. Thus we need to establish the effective temperature of one of the components independently.

In this section we conduct a more detailed spectral analysis to determine the primary star’s effective temperature. To begin, we measure the rotational velocities of the two stars and determine their flux ratio. This information guides our spectral classification of the primary by establishing the rotational broadening of the primary spectrum and the extent to which the secondary spectrum contaminates the lines that we use to classify the primary. The rotational velocity and flux ratio information will also prove useful in constraining our light curve analyses below. Finally, we measure the strength of two spectral features of interest in studies of young stars, Li and H α , the former of which serves to establish stellar youth and the latter of which serves as a proxy for chromospheric activity and/or accretion.

4.3.1. Rotational velocities

We measure the rotational velocities, $v \sin i$, of the two components of V1174 Ori in two ways. First, the cross-correlation functions we used to measure radial velocities (§4.2.1) contain rotational information in the sense that the peak widths are related to $v \sin i$. Second, we use the ratio of the widths of the primary and secondary Li lines to constrain the ratio of $v \sin i$ of the two components.

Because the widths of the cross-correlation peaks reflect the convolution of the intrinsic stellar $v \sin i$ with both the instrumental response function and the radial-velocity template spectrum, the peak widths do not directly yield a measure of $v \sin i$. We calibrated the width of the cross-correlation peak to $v \sin i$ by artificially rotationally broadening our narrow-lined (lines unresolved) spectral standards (see Table 3) and then cross-correlating these broadened spectra against the same radial-velocity template used with our V1174 Ori spectra. This was done separately for each spectral order. We find that our cross-correlation functions permit us to discern $v \sin i$ values of $\gtrsim 10$ km/s.

Using this calibration, we measured $v \sin i$ values for the components of V1174 Ori from each spectrum, averaging together the values from the multiple orders in a given spectrum. The resulting $v \sin i$ values are 26.2 ± 0.6 km/s and 20.5 ± 1.6 km/s for the primary and secondary, respectively. Here the uncertainties are the standard deviation of the mean.

We wish to emphasize that the uncertainties quoted above are strictly internal. Furthermore, we caution that we have not used $v \sin i$ standards for an external calibration. For our present purposes, what is robust here is that the rotational velocities for the stars are ~ 20 – 25 km/s, and that the primary star rotates more rapidly than the secondary. This latter point is corroborated by our analysis of the primary and secondary Li lines below (§4.3.4).

4.3.2. Flux ratio

We use the temperature-insensitive Ca II lines at $\lambda\lambda 6102, 6122$ to measure the flux ratio between the primary and secondary components of V1174 Ori. We fit the V1174 Ori spectrum of UT 2002 Feb 07 by adding together at various ratios the spectra of our K3 and K7 standards¹³ (see Table 3) at the appropriate radial velocities and with the appropriate rotational broadening. We chose the UT 2002 Feb 07 spectrum because on this date the secondary was shifted a full 174 km/s (3.5Å at this spectral region) redward of the primary. The two components are thus well separated, and the $\lambda 6102$ line of the secondary is shifted into a region of the spectrum (6105.5Å) that is free of lines from the primary.

We find a best fit to the Ca II lines in the V1174 Ori spectrum when we combine the two templates in a 6:1 ratio, (Fig. 14), although ratios of 5:1 and 7:1 also fit the observed spectrum reasonably well.

4.3.3. Spectral classification

Our high-resolution HET HRS spectra permit spectral classification of the primary from careful examination of temperature-sensitive line ratios. As demonstrated by Basri & Batalha (1990) and by Lee (1992), the ratio of Ni I $\lambda 6108$ to V I $\lambda 6112$, the ratio of V I $\lambda 6040$ to Fe I $\lambda 6042$, the ratio of V I $\lambda 6058$ to Fe I $\lambda 6056$, and the ratio of Sc I $\lambda 6210$ to Fe I $\lambda 6200$ provide a good determination of spectral class from high-resolution spectra. These line ratios were also used by Steffen et al. (2001) in their analysis of the PMS binary NTT 045251+3016.

We have carefully examined these line ratios in our spectra that have the secondary sufficiently Doppler-shifted with respect to the primary. We find a spectral type for the primary of K4–K5, with an uncertainty of $\sim 1/2$ subclass. As an example, in Fig. 13 we compare the first line pair above from our HET HRS spectrum of UT 2002 Feb 07 with four spectral standards of type K1, K3, K4, and K5. The observed line ratio indicates a K4.5 spectral type, but after correcting the primary’s V I line for contamination by the secondary’s Ni I line (using the flux ratio determined above), we find a K4 spectral type in this spectrum.

Taking all of these line-pair ratios from all of our observations into account, we find a mean spectral type for the primary of $K4.5 \pm 0.1$. Due to the quantized nature of the spectral classification process (0.5 sub-type), this uncertainty is likely unrealistically small, so we adopt a more conservative uncertainty of 0.5 spectral sub-type. Using the SpT- T_{eff} conversion of Schmidt-Kaler (1982), this implies an effective temperature for the primary of $T_{\text{eff}} = 4470 \pm 120$ K.

¹³Our use of the K3 and K7 standards is based on the preliminary spectral types that we determined for the two components of V1174 Ori, but as the Ca lines used are temperature-insensitive any two standards of roughly mid-K to early-M spectral type would suffice.

Using this together with the ratio of T_{eff} determined from our light curve analysis below (§4.4), we infer that the secondary has an effective temperature of $T_{\text{eff}} = 3615$ K, implying a spectral type of \sim M1.5.

4.3.4. Lithium

The $\lambda 6708$ line of Li is a commonly used indicator of stellar youth, as stars rapidly destroy their natal Li content during the first \sim few $\times 10^7$ yr of their evolution. For very young stars, the Li line at 6708\AA can be very strong, with equivalent widths from ~ 300 mÅ for early K stars to ~ 750 mÅ for mid-M stars (Dolan & Mathieu 1999). Indeed, in our HET HRS spectra, the Li line is one of the few lines from the secondary that can be unambiguously identified by eye.

We have measured the equivalent widths of the primary and secondary Li lines in those spectra where the two stars are sufficiently Doppler-shifted relative to one another. As an example, the spectrum of UT 2002 Jan 28 has the secondary at a radial velocity of +102.55 km/s relative to the primary. The Li equivalent width (EQW) we measure for the primary star in this spectrum is $\text{EQW}(\text{Li})_A = 398$ mÅ. We measure the Li EQW of the secondary star to be $\text{EQW}(\text{Li})_B = 78$ mÅ after correcting for the contribution of spectral features from the primary. These EQW measures also include a 5% correction for the presence of third light, based on our light curve analysis (§4.4.3) which indicates 0% third light at V and 10% at I .

If intrinsically equal, these EQW values would imply a flux ratio of 5.1. However, adopting spectral types of K4.5 and M1.5 for the two components implies that the intrinsic EQW of the secondary’s Li line is $\sim 25\%$ greater than that of the primary (Dolan & Mathieu 1999). Correcting the secondary’s $\text{EQW}(\text{Li})$ accordingly results in a flux ratio of 6.3, consistent with that derived from our analysis of the temperature-insensitive lines above (§4.3.2). Thus from this spectrum we infer intrinsic equivalent widths for the two stars of $\text{EQW}(\text{Li})_A \approx 465$ mÅ and $\text{EQW}(\text{Li})_B \approx 545$ mÅ. The other spectra for which we could cleanly separate the primary and secondary Li features yield values consistent with these. Adopting a flux ratio of 6:1, we find from the ensemble of our spectra $\text{EQW}(\text{Li})_A = 480 \pm 14$ mÅ and $\text{EQW}(\text{Li})_B = 537 \pm 26$ mÅ.

We can use these EQW measurements to infer Li abundances for the two stars. From the Li curve-of-growth analysis of Pavlenko & Magazzu (1996), we find $N(\text{Li})_A = 3.08 \pm 0.04$ and $N(\text{Li})_B = 2.20 \pm 0.06$ assuming LTE, and $N(\text{Li})_A = 3.00 \pm 0.05$ and $N(\text{Li})_B = 1.98 \pm 0.09$ for the non-LTE case. Note that these abundance estimates are likely to be slightly lower than the actual abundances, as the curve-of-growth values used assume $\log g = 4.5$, whereas the components of V1174 Ori have $\log g \approx 4.2$ (see §5.1). In addition, the uncertainties listed reflect only the error in the measurement of the EQW; including the uncertainty in the stellar T_{eff} increases the abundance uncertainties to 0.2 dex.

Thus, the primary star’s Li abundance is consistent with at most 0.2–0.3 dex of depletion (assuming a “cosmic” Li abundance of $\log N(\text{Li}) = 3.3$), whereas the secondary shows > 1 dex of

depletion. As discussed by D’Antona & Montalbán (2003) the pattern of PMS Li depletion as a function of stellar mass and age can provide important constraints on PMS tracks. We will return to the issue of Li abundances in §6.5.

Finally, we can also use the primary and secondary Li lines to infer the relative rotation rates of the two stars. We have already derived $v \sin i$ values from the widths of the cross-correlation peaks (§4.3.1). Using the ratio of the widths of the Li lines, we can independently infer the ratio of $v \sin i$. We have measured this ratio from our spectra that have the primary and secondary Li lines sufficiently well separated to allow a clean measurement of their FWHM, and find a $v \sin i$ ratio of 1.21 ± 0.04 , consistent with the $v \sin i$ values determined from the cross-correlation analysis.

4.3.5. $H\alpha$

Emission of the $H\alpha$ line is also of interest in studies of young stars. Indeed, emission stronger than $\text{EQW}(H\alpha) \approx 10 \text{ \AA}$ is a defining criterion for classical TTS, which are believed to be PMS stars actively accreting from circumstellar disks. Even non-accreting TTS often show some amount of $H\alpha$ in emission, which is thought to indicate the presence of strong chromospheric activity.

Based on the strength of $H\alpha$ emission, V1174 Ori does not appear to be an actively accreting system, with neither component exhibiting $H\alpha$ emission in excess of a few \AA EQW in any of our spectra. In Fig. 15, we show the spectrum of UT 2002 Feb 23 in the vicinity of $H\alpha$. This spectrum has the components of V1174 Ori at their greatest radial-velocity separation, making it possible to detect their individual $H\alpha$ emission apart from the very strong nebular emission. The observed equivalent widths measure $\text{EQW}(H\alpha)_A = -0.4 \text{ \AA}$ and $\text{EQW}(H\alpha)_B = -4.2 \text{ \AA}$, after correcting for the continuum of the companion.

4.4. Light curve synthesis and modeling

Having determined an ephemeris for V1174 Ori, and having conducted a thorough spectral analysis of the system including determination of a double-lined orbit solution, we now analyze our multi-epoch, multi-band light curves (Table 1, Figs. 2–7) in detail to determine the orbital inclination of the system, T_{eff} for the secondary, and absolute radii for both components. Our analysis procedure makes use of a Wilson-Devinney (WD) based algorithm that models the observed photometric variations with synthetic light curves that include the effects of limb darkening, gravity brightening, mutual illumination and occultation, and spots. In addition, the code permits the use of either simple Planckian fluxes or detailed model atmospheres. Along the way, we use information provided by our spectroscopic analyses ($v \sin i$, flux ratio, primary T_{eff}) to further constrain the model light curve parameters.

4.4.1. Initial considerations

Although the light curves shown in Figs. 2, 4 and 6 are typical for a system with non-distorted components, apparently well-detached from their Roche lobes, they also reveal the presence of variations not related to the eclipses. From careful inspection of the light curves it becomes evident that these variations are most likely due to star spots that change from one epoch to the next, hindering the use of our photometric data from all epochs in a single, integrated analysis.

Thus, to begin, we used the data from the epoch with the most complete set of light curves—those obtained in Jan 2001 in 5 filters (*vbyVI*)—to produce an initial set of light curve solutions. These initial light curve solutions were calculated without spots by fitting simultaneously the 5 light curves from Jan 2001 together with the radial velocity data from Table 5.

Our analysis was performed with the WD light-curve synthesis program (Wilson & Devinney 1971; Wilson 1993a,b). Besides other modifications (Vaz et al. 1995; Casey et al. 1997), our version of the WD code was implemented with the possibility of using the SIMPLEX solution method (Kallrath & Linnel 1987; Vieira 2003) as an alternative to the traditional least-squares method. Limb-darkening coefficients for both eclipsing components were described using the data from van Hamme (1993). All three limb-darkening laws (linear, linear-log, and linear-square root) were examined, with the coefficients calculated by bi-linear interpolations using the current values of $\log g$ and T_{eff} . The linear law gave marginally better solutions and was therefore adopted. Bolometric albedoes for both components were set equal to 0.5 as appropriate for atmospheres in convective equilibrium. Gravity-brightening exponents were calculated using the local value of T_{eff} for each point on the stellar surfaces, taking into account mutual illumination, according to Alencar & Vaz (1997) and Alencar et al. (1999). The radiated flux of both stars is described using the atmosphere model tables of Buser & Kurucz (1992), updated relative to the original versions of the WD code. As the T_{eff} of the secondary is lower than the minimum T_{eff} included in the published tables (4000 K), we extrapolated linearly in a $\log(\text{theoretical magnitude})$ vs. $\log(\text{temperature})$ scale. Both the radial velocities and the photometric times of minima indicated no sign of orbital eccentricity, so we assumed circular orbits in the light curve analysis.

In performing these initial calculations, we applied least-squares differential corrections between successive iterations to the orbital inclination, the secondary T_{eff} , the primary luminosity, both stellar surface gravitational pseudopotentials (stellar radii), the center-of-mass radial velocity, the mass ratio and an arbitrary phase shift to be added to the observations. The luminosity of the secondary was calculated from its size and T_{eff} . In addition, the limb-darkening coefficients, normalization magnitudes, surface gravities, and individual velocity amplitudes were all updated between successive runs to correspond to the solution from the previous iteration.

Initially, the WD code settled on a solution in which the secondary star was larger than the primary. However, this solution violated the observed luminosity ratio (§4.3.2) as well as the observed rotational velocities if synchronous rotation is assumed. By forcing the luminosity ratio constraint, the code found another solution in which the primary is larger. This solution matches

the observed luminosity ratio and predicts rotational velocities similar to those observed. This solution thus served as a starting point for introducing additional parameters into the analysis, such as spots, as we now describe.

4.4.2. Star spots

After determining an initial solution as described above, we introduced spots in the WD calculation in order to model the out-of-eclipse variations observed. We started by introducing one cold spot on each component. For each spot on each star, four parameters are added to the WD calculation: the longitude and co-latitude of the spot, the spot radius (as seen from the center of the star), and the spot temperature factor (< 1 for cold spots and > 1 for hot spots).

In this phase of the calculation, we found the SIMPLEX method to be much more efficient in finding best-fit solutions than the least-squares method, the latter being very sensitive to small corrections to the spot parameters, leading to frequent divergence of the solution. Although the WD algorithm can deal with spots that move in longitude across the surface of the star, we assumed that the spots rotate with the same angular velocity as the star. After convergence of each set of spots, we tried many different combinations of spot number and configurations, trying to minimize the number of spots on each star. Note that the WD code treats regions in which multiple spots overlap by multiplying their temperature factors¹⁴.

Ultimately, both “cold” and “hot” spots were needed on each star to reproduce the light curves of Fig. 2. The cold spots made it necessary to extrapolate in the atmosphere tables, as mentioned above for the secondary star, for some points on the surface of the primary star as well. The calculations with atmosphere tables were compared with calculations using blackbodies, and we concluded that the extrapolation done (linearly in a logarithmic scale) was reasonable. Thus, except for the *JHK* light curves for which Buser & Kurucz (1992) did not publish atmosphere calculations, we thus chose to use atmosphere models instead of simple Planck functions.

There exist multiple combinations of spots that can reproduce the observed out-of-eclipse variations reasonably well. We believe that the 3 spots on each star used in our final solution (Table 9) are physically realistic. Moreover, our use of light curves in five different bands makes the spot solution more robust, as we insisted that one spot configuration reproduce all of the light curves simultaneously. In any case, the goal of including spots in the light curve modeling is not to determine the properties of the spots per se, but rather to better constrain the morphology of the light curves around the eclipses and thereby to minimize the uncertainty in the parameters of true import: the system inclination, the ratio of T_{eff} , and the stellar radii.

¹⁴This differs from, e.g., the *Nightfall* program, which uses the average of the temperature factors. See <http://www.lsw.uni-heidelberg.de/users/rwichman/Nightfall.html> .

4.4.3. Third light

The Jan 2001 light curves proved impossible to fit together unless we included $\sim 10\%$ third light in I . The V light curve required a slightly *negative* amount of third light, which is physically meaningless. We thus forced $L_3(V) \equiv 0$, but left this parameter free to be adjusted at the other wavelengths. The final solution is shown in Figs. 2 and 3 and in Tables 8 and 9. With the exception of I , the significance of the L_3 values found for the light curves is questionable as they do not follow a Planckian distribution with wavelength. They are probably artifacts of the data-reduction process (e.g. background subtraction in the aperture photometry, scattered light, etc.).

4.4.4. Final solutions

In order to test the validity of the stellar parameters found above from the light curve solutions for the Jan 2001 data, we applied the same analysis procedure to the other sets of light curves (Table 1), now forcing all the parameters, except those corresponding to the star spots, to remain fixed. The resulting fits for the I light curves obtained in Nov 2001 and the BVI light curves obtained in Nov–Dec 2002 are shown in Figs. 4 and 5. The characteristics of the spots used are given in Table 9. The amount of third light at the different wavelengths were left as free parameters. $L_3(V)$ and $L_3(B)$ tended to become slightly negative, while $L_3(I)$ was once again $\sim 10\%$. We thus used no third light for V and B , and adopted the value for $L_3(I)$ shown in Table 8.

The I -band discovery light curve obtained in Dec 1994 (Table 1) was also fit with the solution of Table 8 and a different spot configuration. The amount of third light was again fixed at the value shown in Table 8. Similarly, the JHK light curves from Carpenter, Hillenbrand, & Skrutskie (2001), while not providing complete phase coverage, were also fit with this solution. No third light was included in the JHK light curves because the third light parameter mainly affects the depth of the minima, and unfortunately the minima were not covered by the Carpenter, Hillenbrand, & Skrutskie (2001) observations. The solutions are shown in Figs. 6 and 7, and the spots used are listed in Table 9.

Overall, the quality of the synthetic light curve fits to the data is excellent. Indeed, all 5 bands from the Jan 2001 observations are fit extremely well, with only minor systematic effects visible in the residuals (Fig. 3). Small systematic residuals do persist in some of the light curves at other epochs. For example, in the Nov–Dec 2002 I -band data there are 2 points that deviate by more than 0.02 mag relative to the theoretical light curve near secondary minimum (Figs. 4 and 5). The data points close to secondary minimum in V and B also show small deviations, although at only ~ 0.01 mag these are not by themselves statistically significant. A few deviant data points also appear at other phases (e.g. phase 0.3 in I). These might be indicative of erratic variations as have been reported in, e.g., AK Sco (Alencar et al. 2003) and TY CrA (Casey et al. 1997). Indeed, the most discrepant point near phase 0.5 in the Nov–Dec 2002 I -band light curve was obtained by itself more than two weeks later than the other points near that phase; perhaps there was small amount

of spot evolution or some other small change in the system over the course of the Nov–Dec 2002 epoch.

A limitation in our ability to analyze small-scale photometric variability over long timescales is that our differential photometric observations were not all reduced in one integrated procedure, but separately for each epoch. The Honeycutt (1992) algorithm we employ determines the differential photometric variations relative to a statistically defined ensemble of comparison stars, and this statistical ensemble is not necessarily common to all epochs. Consequently, the photometric calibrations from one epoch to the next are not absolutely tied to one another. In both AK Sco and TY CrA, secular changes in system brightness from one epoch to the next have been attributed to variable obscuration by dust. Unfortunately, we cannot determine from our current analysis whether such global changes in system brightness are taking place in V1174 Ori over long timescales.

Even so, the light curve analyses presented here show clear evidence for changes with time in both the number and the characteristics of the spots on both components. The time coverage of the observations was not adequate to follow the evolution of the spots in detail, but there are hints in Table 9 that some of the spots may persist on month timescales, drifting across the surfaces of the stars. The hot spots apparently come and go more sporadically and, besides occurring more frequently on the secondary than on the primary, they tend to be smaller than the cold spots. Finally, although the rotation rates of Table 8 indicate orbital synchronism within the errors, one of the reasons for spot drifting may be that the stars are not yet completely synchronized. The stars may also present differential rotation, as in the Sun and as recently determined for the rapidly-rotating RS CVn binary UZ Librae (Oláh et al. 2003).

In the end, while some questions remain as to the origin of the variability observed in some of our light curves at the finest level of detail, the overall match between the synthetic light curves and the data is excellent (Figs. 2–7), and for the remainder of our analysis we adopt the solution listed in Table 8.

5. Results

5.1. Fundamental stellar parameters

Combining our spectroscopic and photometric analyses presented above, we can establish all of the fundamental stellar properties for both components of V1174 Ori. We report these parameters in Table 10.

We can in principle determine the extinction, A_V , toward the system by fitting the observed colors (Table 2), assuming main-sequence intrinsic colors (Kenyon & Hartmann 1995) and bolometric corrections (Popper 1980) for the primary and secondary components of V1174 Ori. There is not a single value of A_V that simultaneously reproduces all of the observed colors. Formally,

however, we find a best-fit value of $A_V = 0.32$, which results in a distance to the system of 419 pc when we normalize to the observed V magnitude (see §5.2 below). The colors calculated with this extinction and distance are compared to the observed values in Table 2.

The agreement between the observed and calculated colors is best in $B - V$, where the observed flux is dominated by that of the primary star, and in $J - H$ and $H - K$, where the colors become largely degenerate for dwarfs of mid-K to early-M spectral type. The observed $U - V$ color is bluer than predicted by 0.11 mag, perhaps the result of a mild UV excess from one or both of the stars, as is common among chromospherically active PMS stars, and possibly consistent with the observed $\text{H}\alpha$ emission (see §4.3.5) and hot spots (§4.4.2).

The observed $V - I$ color is somewhat redder than predicted (by 0.14 mag), roughly consistent with the level of third light inferred from our light curve modeling (§4.4) in the I band ($\sim 10\%$). Similarly, the observed J magnitude is 0.30 mag brighter than predicted.

We can improve slightly the fit to the observed $V - I$ color and J magnitude by increasing the A_V . For example, adopting $A_V = 0.42$ would predict $V - I = 1.52$ and $J = 11.46$. Of course, this worsens the agreement in the other colors, most notably in $U - V$, and results in a distance (401 pc) less compatible with that typically assumed for the ONC (≈ 470 pc).

Together, the $V - I$ and J discrepancies suggest the presence of a third, low-mass star in the system that contributes flux noticeably only at $\lambda \gtrsim 0.9\mu\text{m}$. This would imply that V1174 Ori is in fact a hierarchical triple system, with the tertiary in a sufficiently wide orbit so as to not manifest itself in the observed radial velocities (§4.2.1). Curiously, TY CrA (Casey et al. 1998), one of the other three PMS eclipsing binaries in the literature, is also reported to be a triple system.

5.2. Distance to V1174 Ori

Since we measure the luminosities of the components of V1174 Ori directly from T_{eff} and R , we can infer a distance to the system assuming a particular A_V derived from the system colors (see above). The distance we derive to V1174 Ori of 419 ± 21 pc differs somewhat from that which has been quoted for the ONC in the recent literature. For example, Hillenbrand (1997) adopt a distance of 470 pc, and Bally, O'Dell, & McCaughrean (2000) use a distance of 460 pc.

Various other authors have determined distances to the ONC and to the various subgroupings of Orion OB1, ranging from 400–500 pc. Based on photometry of several tens of bright O and B stars, Warren & Hesser (1978) find a distance of 480 pc to the Trapezium cluster (Ori OB1d) and 430 pc to the foreground Ori OB1c, while Anthony-Twarog (1982), using the same data, find a distance of 434 pc for Ori OB1d. Using different photometric indices, Brown, de Geus, & de Zeeuw (1994) find a distance of only 400 pc for Ori OB1c. Perhaps the most robust constraint is that provided by the BN-KL masers, situated just behind the ONC, at 480 pc (Genzel et al. 1981).

Given precisely determined luminosities for the two eclipsing components of V1174 Ori, our

distance determination depends primarily upon A_V , with lower values placing the system farther from the Sun. Based on our analysis of the observed colors, we do not believe that A_V can be much lower than what we report above. Using the value of A_V reported in Table 2, the discrepancy between the observed and predicted $V - I$ color is already consistent with the amount of third light that we find for the I band from our light curve analysis. Decreasing A_V would increase the discrepancy in $V - I$, which would be incompatible with our light curve solution.

Once the value of A_V is determined, we compute the distance via the distance modulus in V . Our V -band measurement has a formal uncertainty of 0.03 mag, which translates into an additional distance uncertainty of 6 pc. Of course, this uncertainty does not include any possible influence of spots which, from our analysis above (§4.4.2) has been observed to be ~ 0.1 mag peak-to-peak in V . Our calibrated photometry was obtained in 1995, an epoch at which we unfortunately do not have light curves that could inform us as to the influence of spots on the calibrated magnitudes. If, for example, a cool spot were acting to depress the V -band flux by 0.1 mag, then our derived distance would be underestimated by 20 pc.

Another, if subtler, consideration in our distance determination is the value assumed for the solar bolometric magnitude, $M_{\text{bol},\odot}$. Lower values of $M_{\text{bol},\odot}$ (i.e. brighter) result in V1174 Ori being farther from the Sun. We have adopted the value of $M_{\text{bol},\odot} = 4.59$ used by Caloi, D'Antona, & Mazzitelli (1997), which produces a distance roughly consistent with the other distance determinations discussed above. However, the value currently adopted by the IAU, $M_{\text{bol},\odot} = 4.75$, results in a distance to V1174 Ori of 390 pc.

Based on this discussion, we consider it likely that V1174 Ori is a member of the older, foreground Ori OB1c at a distance of ~ 400 pc, consistent with the slightly older age (~ 10 Myr) that we find below. Indeed, the position of V1174 Ori approximately 0.3 degrees to the south of $\Theta^1\text{C}$ Ori places it just outside the region defined as Ori OB1d by Blaauw (1964) and in the region defined as Ori OB1c.

6. Comparison to theoretical pre-main-sequence evolutionary tracks

In this section, we use the empirically determined masses, radii, effective temperatures, and luminosities of the primary and secondary components of V1174 Ori to test the predictions of PMS stellar evolutionary models. We consider in turn four sets of PMS tracks commonly used in the literature: Baraffe et al. (1998) (§6.1), Palla & Stahler (1999) (§6.2), Siess, Dufour, & Forestini (2000) (§6.3), and Montalbán et al. (2003) (more recent version of the D'Antona & Mazzitelli (1997) tracks; §6.4).

These models differ primarily in their choice of atmospheres/opacities, the equation of state, and in their treatment of convection. With respect to the former, the models essentially differ in terms of whether the atmosphere models used are gray or non-gray, and whether molecular opacity effects are included at low effective temperatures. The differences with respect to convection are

somewhat more subtle. Except for one set of models that uses the Full Spectrum Turbulence (FST) formalism of Canuto et al. (1996), the models we consider in this paper use a mixing-length theory (MLT) approach, typically characterized by the mixing parameter, α , defined as the ratio of the convective mixing length to the pressure scale-height, i.e. $\alpha \equiv l_{\text{mix}}/H_p$. But as discussed by Montalbán et al. (2003) and D’Antona & Montalbán (2003), to fully characterize an MLT model requires specification of a larger set of ingredients than just the single parameter α . These are: the mixing parameter used in the atmosphere calculation (α_{atm}); the mixing parameter used in the calculation of the interior (α_{in} , which can be set equal to α_{atm}); and the optical depth in the atmosphere at which these two calculations are matched up (τ_{ph}). Requiring a fit to the present-day Sun generally requires more efficient convection in the interior than in the atmosphere, that is, $\alpha_{\text{in}} > \alpha_{\text{atm}}$ (Baraffe et al. 1998; Montalbán et al. 2003). For a given choice of α_{atm} and α_{in} , larger τ_{ph} produce lower temperatures at the base of the convection zone, resulting in less Li depletion prior to the main sequence. The parameters used by the various models considered below are summarized in Table 11. All of the tracks considered assume solar metallicity.

For each set of tracks, we first consider the positions of the components of V1174 Ori in the H-R diagram (T_{eff} vs. $\log L$) and compare the stellar masses inferred from the models to those we have measured. We also consider whether the theoretical isochrones lie parallel to the observed positions.

Comparing the observations to the models in the plane of the H-R diagram is not necessarily the most robust test of the models, however, and certainly does not take full advantage of the accuracy of the measurements. Placing the stars in the H-R diagram requires deriving L from R and T_{eff} . While the measurement errors in the radii are small, the T_{eff} values have not been determined directly but rather converted from the observed spectral type (for the primary) and then from the T_{eff} ratio determined from the light curve analysis (for the secondary). Consequently, the uncertainties in the derived luminosities are relatively large. Thus for each set of tracks we also do the comparison in the mass-radius plane. In this way, not only do we preserve the accuracy of the empirical masses and radii, we also test what is perhaps the most fundamental prediction of the models: the mass-radius relationship.

One final comment is in order, regarding the placement of the primary and secondary stars in the H-R diagrams shown in Figs. 16–21. In each H-R diagram we plot two nested boxes around the measured position of the primary star. The inner box represents the region of the $(\log L, T_{\text{eff}})$ space allowed by the combination of the uncertainty in the primary star’s T_{eff} (0.5 spectral subtype; §4.3.3) and 1σ uncertainty in its radius ($0.015 R_{\odot}$; Table 10). The outer box corresponds to twice the uncertainty in T_{eff} and 2σ uncertainty on the radius. This outer box should thus be regarded as the region of high confidence for the location of the primary star in the H-R diagram. We plot similar nested boxes about the position of the secondary star, but the range of T_{eff} here is determined by keeping the secondary-to-primary T_{eff} ratio fixed at the value determined from the light curve analysis (§4.4), the uncertainty of which is minuscule compared to the uncertainty in the T_{eff} of the primary star. Because the two stars’ positions are linked via the T_{eff} ratio, it

is important to bear in mind that the positions of the two stars in the H-R diagram are very strongly correlated. While it may be tempting to adjust the position of each star within its own bounding box independently, the positions of the two stars *relative to one another* are in fact rigidly constrained.

6.1. BCAH98

We begin by considering the PMS tracks of Baraffe et al. (1998). Of the models that we consider here, these are perhaps the most generally favored in the recent literature (White et al. 1999; Simon, Dutrey, & Guilloteau 2000; Luhman et al. 2003). The tracks use the non-gray NextGen atmospheres of Hauschildt, Allard, & Baron (1999) and treat convection using MLT. These models are shown in Figs. 16 and 17 for two different values of α_{in} (1.0 and 1.9, respectively). Note that both models use NextGen atmospheres computed with $\alpha_{\text{atm}} = 1.0$ (see Table 11); thus, these models differ in their convection properties only interior to an optical depth of $\tau_{\text{ph}} = 100$. The tracks with $\alpha_{\text{in}} = 1.9$ are designed to match the properties of the present-day Sun.

Neither of these Baraffe et al. (1998) models succeed in simultaneously reproducing the observed positions of both components of V1174 Ori in the H-R diagram. The tracks with $\alpha_{\text{in}} = 1.0$, favored by Steffen et al. (2001) in their analysis of the PMS binary NTTS 045251+3016, predict a mass for the V1174 Ori primary of $\gtrsim 1.1 M_{\odot}$. The position of the primary excludes the $1.01 M_{\odot}$ track with $> 3\sigma$ confidence. Meanwhile, the $0.73 M_{\odot}$ track is consistent with V1174 Ori secondary at the $\sim 1.5\sigma$ level.

The tracks with $\alpha_{\text{in}} = 1.9$, favored by the recent analysis of Luhman et al. (2003), are possibly consistent with the position of the $1.01 M_{\odot}$ primary of V1174 Ori, but only by pushing the primary near the lower extreme of its 2σ bounding box. Forcing agreement with the primary in this way necessarily forces the secondary to the lower extreme of its 2σ bounding box as well. This would imply a mass for the secondary star of $\sim 0.4 M_{\odot}$, completely inconsistent with its measured mass of $0.73 \pm 0.01 M_{\odot}$. The $0.73 M_{\odot}$ track is ~ 400 K too hot relative to the position that the secondary would take if the primary were forced into agreement with its mass track.

Of the BCAH98 models considered here, only the $\alpha_{\text{in}} = 1.9$ tracks possess an isochrone in the H-R diagram (at ~ 7 Myr) consistent with coevality for the components of V1174 Ori. The other tracks make the secondary appear over-luminous relative to the primary.

In the mass-radius (M - R) plane, both sets of tracks imply an age for the V1174 Ori system of ~ 10 Myr, though none of the tracks possess an isochrone precisely parallel to the empirical isochrone defined by the components of V1174 Ori. Interestingly, this is true of the $\alpha = 1.9$ tracks as well, despite the fact that these tracks yield coevality for the two stars in the H-R diagram. Apparently, the empirical measurements and the theoretical isochrones translate differently between the M - R plane and the H-R diagram, almost certainly the result of differences in the T_{eff} scale. This is most readily seen in the $\alpha_{\text{in}} = 1.0$ tracks where, in the M - R plane, the secondary is situated

below the 10 Myr isochrone and the primary is above it; in the H-R diagram their positions relative to this isochrone are reversed.

6.2. PS99

The PMS tracks of Palla & Stahler (1999) have been found to show reasonably good agreement with PMS mass measurements in a number of previous analyses (Steffen et al. 2001; Simon, Dutrey, & Guilloteau 2000; Palla & Stahler 2001). These models arguably use the most physically realistic initial conditions of any of the models, that of the stellar birthline (Stahler 1983). They use a gray atmosphere approximation, and use the Alexander & Ferguson (1994) and Iglesias & Rogers (1996) opacities for T_{eff} below and above 10^4 K, respectively. Convection is treated with MLT and $\alpha_{\text{in}} = 1.5$. These tracks are compared with the observations of V1174 Ori in Fig. 18.

The PS99 models show good agreement with the position of the primary star in the H-R diagram, with the $1.01 M_{\odot}$ track passing within the inner bounding box of the primary's position. However, the position of the secondary star excludes the $0.73 M_{\odot}$ track with $> 3\sigma$ confidence. As with the BCAH98 tracks, the $0.73 M_{\odot}$ track is ~ 400 K too hot compared to the position of the V1174 Ori secondary.

The PS99 models moreover yield ages for the two components of V1174 Ori that are non-coeval. The tracks give ages of 10 Myr and 5 Myr for the primary and secondary, respectively. Interestingly, this non-coevality in the H-R diagram is not borne out in the M - R plane, where the components lie precisely parallel to the theoretical isochrones (9 Myr in this case). Indeed, of the models considered in this paper, these models show the best agreement with the slope of the M - R relationship as defined by the components of V1174 Ori.

6.3. SDF00

Next, we consider the PMS models of Siess, Dufour, & Forestini (2000). These models, shown in Fig. 19, use the Alexander & Ferguson (1994) and Iglesias & Rogers (1996) opacities, and the model atmospheres of Plez (1992) and Kurucz (1991). They treat convection with MLT and $\alpha_{\text{in}} = 1.6$ to match the present-day Sun.

These tracks behave in a similar fashion as the PS99 tracks. In particular, the position of the V1174 Ori primary is precisely matched by the theoretical $1.01 M_{\odot}$ track, but the agreement with the location of the V1174 Ori secondary is extremely poor. Indeed, the theoretical $0.73 M_{\odot}$ track is a full ~ 500 K too hot compared to the observed position of the secondary star. These tracks, like the others considered above, appear to be too compressed in T_{eff} to simultaneously fit the primary and secondary of V1174 Ori.

As with the Palla & Stahler (1999) models, these tracks yield non-coeval ages for the two

components of V1174 Ori. Once again, the inferred ages for the primary and secondary stars differ by a factor ~ 2 : in this case, ~ 7 Myr and ~ 3 Myr for the primary and secondary, respectively. But as with the PS99 models, despite non-coevality in the H-R diagram, these models produce isochrones in superb agreement with the observations in the M - R plane (7 Myr).

6.4. MDKH03

Finally, we consider the new PMS evolutionary tracks of Montalbán et al. (2003), descended from the earlier models of D’Antona & Mazzitelli (1997). These authors have produced a variety of models that treat convection via MLT or FST, with the non-gray atmospheres from Hauschildt, Allard, & Baron (1999) or Heiter et al. (2002), respectively. For the models using the NextGen atmospheres of Hauschildt, Allard, & Baron (1999), the authors compute families of models with different values of τ_{ph} . Here we consider three models as listed in Table 11. These models are compared with the measured positions of the components of V1174 Ori in Figs. 20–21.

The MLT models with NextGen atmospheres and $\alpha_{\text{in}} = 1.0$ are most comparable to the BCAH98 tracks in Fig. 16. As the only substantial difference between these models is the depth of the outer atmosphere ($\tau_{\text{ph}} = 3$ for MDKH03 tracks vs. 100 for BCAH98 tracks), these tracks yield very similar results. The only notable difference appears to be in the rate at which the models contract, with the $\tau_{\text{ph}} = 3$ tracks yielding slightly younger ages, as seen in the M - R plane.

In contrast, both the MLT and FST models, with the ATLAS9 atmospheres of Heiter et al. (2002), show excellent agreement with the position of the V1174 Ori in the H-R diagram, with the FST models being ~ 100 K hotter. Unfortunately, these models do not permit a comparison with the V1174 Ori secondary as the Heiter et al. (2002) atmospheres do not extend below 4000 K. However, the general behavior of these tracks in the H-R diagram suggests that the $0.73 M_{\odot}$ track could intersect the position of the secondary if the calculation were extended to lower T_{eff} .

Indeed, these ATLAS9-based models differ qualitatively from all of the other models considered above in terms of the general shape of the tracks. These models exhibit a dramatic sweep to cooler T_{eff} , and then back to hotter T_{eff} , as the stars descend their tracks, particularly for $M < 0.8 M_{\odot}$. The effect is to spread the mass tracks over a larger range of T_{eff} at ages between 3–30 Myr, possibly consistent simultaneously with the primary and secondary of V1174 Ori.

6.5. Other mass measurements of PMS stars

As we have seen, the empirical mass measurements of V1174 Ori provide important constraints on the absolute mass calibration of PMS evolutionary tracks, both in the H-R diagram and in the M - R plane, between $0.7 M_{\odot}$ and $1.0 M_{\odot}$. In this section, we combine our measurements of V1174 Ori with extant mass measurements of other PMS stars in order to extend our analysis to

a larger range in stellar mass and to compare our findings among stars in both binary and single systems.

Empirical mass determinations exist in the literature for twelve¹⁵ other PMS stars—8 in binary systems, 4 single—with masses accurate to better than $\sim 10\%$ and that are within the range covered by the PMS tracks considered above ($\lesssim 1.6 M_{\odot}$). These are: TY CrA B with $M = 1.64 \pm 0.01 M_{\odot}$ (Casey et al. 1998); AK Sco A and B, both with $M = 1.35 \pm 0.07 M_{\odot}$ (Alencar et al. 2003); EK Cep B with $M = 1.12 \pm 0.01 M_{\odot}$ (Popper 1987); NTT 045251+3016 A and B with $M_A = 1.45 \pm 0.19 M_{\odot}$ and $M_B = 0.81 \pm 0.09 M_{\odot}$ (Steffen et al. 2001); RXJ0529.4+0041 A and B with $M_A = 1.25 \pm 0.05 M_{\odot}$ and $M_B = 0.91 \pm 0.05 M_{\odot}$ (Covino et al. 2000); Lk Ca 15 with $M = 0.97 \pm 0.03 M_{\odot}$ (Simon, Dutrey, & Guilloteau 2000); GM Aur with $M = 0.84 \pm 0.05 M_{\odot}$ (Simon, Dutrey, & Guilloteau 2000); DL Tau with $M = 0.72 \pm 0.11 M_{\odot}$ (Simon, Dutrey, & Guilloteau 2000); and DM Tau with $M = 0.55 \pm 0.03 M_{\odot}$ (Simon, Dutrey, & Guilloteau 2000).

In Figs. 22–26 we show all of these stars together on H-R diagrams with the different PMS tracks discussed above. Binary and single stars are plotted separately in each figure. This ensemble of T_{eff} , luminosities, and the uncertainties therein are taken from the compilation of Luhman et al. (2003), which used the same temperature scale used in this study. To this compilation we have added the secondary of TY CrA (Casey et al. 1998), the two (identical) components of AK Sco (Alencar et al. 2003), and the two components of V1174 Ori. Thus the measurements represented in Figs. 22–26 are all based on a consistent T_{eff} scale.

We note that the listed uncertainties in the masses of the single stars do not include systematic uncertainties on the distances to those stars, which can amount to an additional $\sim 15\%$ uncertainty on the masses (Simon, Dutrey, & Guilloteau 2000). We note also that the meanings of the error bars in L and in T_{eff} take on somewhat different meanings for the binary and single stars. For the single stars and the components of the astrometric binary NTT 04251+3016, these quantities are measured independently, whereas for stars in eclipsing binaries these quantities are coupled because L is derived from T_{eff} and the stellar radii. Finally, we note that for the binary stars the individual masses are coupled to one another by virtue of the measured mass ratio; adjusting the mass of one component necessarily adjusts that of the other. These considerations constrain the extent to which individual objects can be “fine-tuned” into agreement with the models.

We do not find a set of tracks that reproduces the observed locations of these stars simultaneously at both high and low masses, and in both binary and single systems.

Consider the BCAH98 tracks with $\alpha_{\text{in}} = 1.0$ (Fig. 22), which have the coolest temperatures of all the tracks we have examined. These tracks agree with most of the binary stars, so long as the masses of individual objects are in some cases adjusted within their uncertainties. For example,

¹⁵We exclude from this discussion RS Cha A and B ($M = 1.86 M_{\odot}$ and $1.82 M_{\odot}$ respectively), because of their high masses. We also exclude BP Tau ($M = 1.32 M_{\odot}$) because of the large uncertainty on the mass determination ($\pm 0.2 M_{\odot}$) and the large uncertainty on its distance (Simon, Dutrey, & Guilloteau 2000).

for the tracks to be consistent with the primary of NTT 045251+3016, its mass must be adjusted downward by 1σ . Of course, doing this requires that the mass of the secondary also be adjusted downward by 1σ , implying a true mass of $0.72 M_{\odot}$ for the secondary. Even so, the tracks miss this star by $\sim 1.5\sigma$. The greatest challenge to these tracks among the binaries is the $1.01 M_{\odot}$ primary of V1174 Ori, which has the most accurate mass determination of the lot. This failure to match the V1174 Ori primary is amplified by the position of LkCa 15; with a very similar mass of $0.97 \pm 0.03 M_{\odot}$, it is located at almost precisely the same position in the H-R diagram. And like V1174 Ori A, LkCa 15 is not matched by these models.

Indeed, none of the single stars are matched by these tracks, the tracks being systematically too cool. The single stars are better matched by the BCAH98 $\alpha_{\text{in}} = 1.9$ tracks (Fig. 23), which are ~ 200 K warmer, a conclusion also reached by Luhman et al. (2003). However, these tracks have difficulty when compared against the binaries, especially for those with $M < M_{\odot}$.

The other models show similarly mixed success in reproducing the observations. The PS99 tracks (Fig. 24) perform comparably to the BCAH98 $\alpha_{\text{in}} = 1.9$ tracks, matching the positions of all of the single stars and, with the notable exception of NTT 045251+3016 A, matching the binaries with $M \geq M_{\odot}$ (including the primary of V1174 Ori) very well. However, the lower-mass binary components—including the secondary of V1174 Ori—are poorly matched by these tracks. The results for the SDF00 models (Fig. 25) are very similar as well, though with the warmest and most closely spaced tracks of those considered here, the discrepancies among the lowest-mass stars are particularly severe, even for the single star DM Tau. Finally, a full evaluation of the MDKH03 MLT ATLAS9 tracks (Fig. 26) is not possible because they do not extend below 4000 K. However, based on the qualitative behavior of these tracks it appears possible that they could perform well over a broad range of masses and for both binary and single stars. The lower temperatures of these tracks means that they agree with many of the higher-mass binary stars (though again with NTT 045251+3016 A being a clear outlier), and with their horizontal sweep in T_{eff} —effectively stretching the T_{eff} scale for stars with $M < M_{\odot}$ —may be able to simultaneously match the positions of the lower-mass binaries and single stars.

For completeness, we show in Figs. 27–28 the mass-radius relation for the three PMS binaries for which empirical mass measurements exist for both components (V1174 Ori, NTT 045251+3016, and RXJ0529.4+0041). With the relatively large error bars on the components of NTT 045251+3016 and RXJ0529.4+0041, we can draw limited conclusions here. All of the models show qualitative agreement with the general slope of the mass-radius relationship. However, the agreement does appear to be best among the tracks with low values of α_{in} , with the BCAH98 $\alpha_{\text{in}} = 1.0$ tracks and the PS99 $\alpha_{\text{in}} = 1.5$ tracks providing the best fit to the observations. The SDF00 $\alpha_{\text{in}} = 1.6$ tracks perform reasonably well, whereas the tracks with large α_{in} (e.g. BCAH98 with $\alpha_{\text{in}} = 1.9$) are least consistent with these measurements.

It is valuable and instructive to consider what insights can be gained from the observations alone, independently of the models. First of all, it appears clear that the masses of the components

of NTT 045251+3016 are over-estimated. The primary star is at a very similar position in the H-R diagram to that of the $1.01 M_{\odot}$ primary of V1174 Ori, despite having a measured mass that is considerably larger. It does have a somewhat higher luminosity, so it is possible that it does indeed have a slightly higher mass than does V1174 Ori A. This conclusion is bolstered by the secondary of NTT 045251+3016; its position in the H-R diagram, suggesting a mass slightly less than the $0.73 M_{\odot}$ secondary of V1174 Ori, belies its measured mass of $0.81 M_{\odot}$. That NTT 045251+3016 may be an outlier may not be surprising given the large uncertainties inherent to the analysis of this astrometric binary, for which only $\sim 1/4$ of the orbit has been mapped (Steffen et al. 2001). Indeed, simply adjusting the mass of the NTT 045251+3016 primary down by $1-2\sigma$, while keeping the mass ratio fixed, would appear to bring the measurements of NTT 045251+3016 and V1174 Ori into closer empirical agreement.

Similar concerns arise with the components of the eclipsing binary RXJ0529.4+0041. Here, the position of the primary star in the H-R diagram coincides closely with that of TY CrA B, despite the latter having a precisely determined mass that is 30% larger. At the same time, however, the secondary of RXJ0529.4+0041 is located between the two components of V1174 Ori, which is appropriate for its measured mass intermediate between those of V1174 Ori A and B. This suggests that the primary (and perhaps the secondary as well) are simply over-luminous, which would tend to implicate the stellar radii in this case since, again, the T_{eff} of the secondary appears approximately correct relative to the components of V1174 Ori. Upon re-examination of the Covino et al. (2000) results for RXJ0529.4+0041, it appears that the uncertainties they report for the luminosities are underestimated. For example, the fractional uncertainty reported by them for the luminosity of RXJ0529.4+0041 A (8%) is smaller than the fractional uncertainty they report (11%) for the radius alone. Including the uncertainty in T_{eff} as well gives a more appropriate uncertainty in the luminosity of $\sim 15\%$.

In some cases, the observations place objects of similar masses at similar positions in the H-R diagram, bolstering their credibility. For example, the primary of V1174 Ori and LkCa 15, both with $M \approx 1.0 M_{\odot}$, have very nearly the same T_{eff} and L . The same is true for RXJ0529.4+0041 B and GM Aur, both with $M \approx 0.87 M_{\odot}$. Even though these latter measurements have somewhat larger uncertainties, the lower luminosity of RXJ0529.4+0041 B relative to (the presumably younger) GM Aur in effect provides an empirical mass track for $M \approx 0.87 M_{\odot}$ between $\sim 3-10$ Myr.

But there are also cases where the data seem at odds with one another. For example, V1174 Ori B and DM Tau occupy similar positions in the H-R diagram despite having masses of $0.73 \pm 0.01 M_{\odot}$ and $0.55 \pm 0.03 M_{\odot}$, respectively. This is worrisome. One way to reconcile this apparent contradiction is to have mass tracks, like the MLT ATLAS9 tracks of Montalbán et al. (2003), that are double-valued in T_{eff} at low masses, allowing stars with different masses to have similar T_{eff} at certain times. While these tracks do not presently extend to the masses of V1174 Ori B and DM Tau, inspecting these tracks in Fig. 26 one can imagine that these stars' positions would be well matched by their respective tracks, particularly with DM Tau being somewhat more luminous than V1174 Ori B.

Another possible explanation for the discordance between these measurements is that the uncertainties in the masses for the single stars are underestimated. Indeed, in contrast to the distance-independent masses derived for V1174 Ori, the masses determined for the single stars (from spatially resolved disk rotation profiles; Simon, Dutrey, & Guilloteau (2000)) depend directly upon the distance assumed. As noted by Simon, Dutrey, & Guilloteau (2000), the distance uncertainty to any particular star in Taurus may be as large as $\sim 15\%$, manifesting itself as a systematic error in the dynamical mass determination.

DL Tau may serve as a case in point. Its measured mass of $0.72 M_{\odot}$ is similar to the mass of $0.73 M_{\odot}$ we have measured for the secondary of V1174 Ori. Yet DL Tau is 450 K hotter than V1174 Ori B, suggesting a mass more comparable to that of V1174 Ori A. An important additional clue to the relative masses of these two objects is provided by their relative Li abundances. In Fig. 29 we show the Li abundances, $\log N(\text{Li})$, for all of the PMS stars discussed above for which Li measurements exist in the literature. These stars exhibit a clear correlation of $\log N(\text{Li})$ with stellar mass: Stars with $M \gtrsim 1.2 M_{\odot}$ show undepleted levels of Li, while less massive stars show a trend of monotonically decreasing Li abundance with decreasing stellar mass. DL Tau is a clear outlier in this trend. Its measured $\log N(\text{Li})$, even with its large uncertainties, is too high for its mass. In contrast, V1174 Ori B follows the empirical trend nicely. The observed Li abundance of DL Tau implies a lower limit to its mass of $\gtrsim 0.9 M_{\odot}$, consistent with its location in the H-R diagram relative to V1174 Ori A. Whether the masses of V1174 Ori B and DM Tau can be similarly reconciled is unknown; there is no published Li abundance for DM Tau.

The observed pattern of Li depletion with stellar mass provides more general constraints on PMS evolutionary tracks, particularly with respect to the efficiency of convection. As discussed in detail by D'Antona & Montalbán (2003), models with more efficient convection (i.e. larger α) result in dramatically more Li depletion than do models with less efficient convection.

Consider a star like V1174 Ori A, having $M = 1.0 M_{\odot}$ and situated near the bottom of its Hayashi phase of evolution. Assuming an initial Li abundance of $\log N(\text{Li}) = 3.3$, a model with $\alpha_{\text{in}} = 1.9$ will have $\log N(\text{Li}) \approx 2.5$ whereas a model with a more modest $\alpha_{\text{in}} = 1.0$ will have $\log N(\text{Li}) \approx 3.2$ (D'Antona & Montalbán 2003). The primary of V1174 Ori is more consistent with the low Li depletion predicted by the $\alpha_{\text{in}} = 1.0$ model. At lower masses, the depletion predicted for models with highly efficient convection becomes ever more severe. A star with $M = 0.7 M_{\odot}$ is predicted to have $\log N(\text{Li}) \approx -1.5$ by the $\alpha_{\text{in}} = 1.9$ models, completely inconsistent with the modest depletion levels seen in Fig. 29, which agree with the predicted levels of depletion for $\alpha_{\text{in}} = 1.0$ models (D'Antona & Montalbán 2003). Thus the Li depletion measurements strongly favor models with low α_{in} .

At low masses, the Li depletion levels predicted by the models also become strongly dependent upon the parameter τ_{ph} . Larger values of τ_{ph} result in a larger fraction of the over-adiabatic region being computed with the low value of α adopted in the model atmosphere. This produces a reduced temperature at the base of the convection zone, resulting in lower levels of Li depletion.

A more detailed analysis of the observed Li abundances as a function of stellar mass is beyond the scope of this paper. But coupled with the precise mass determinations for PMS stars, such as we have determined here, the clear pattern of Li depletion with stellar mass should in principle provide important additional constraints on various key parameters of PMS evolutionary models. Moreover, as we have seen here, Li abundances can provide valuable, independent mass constraints as well when systematic uncertainties (e.g. distance) may limit the accuracy of the dynamical measurements.

7. Summary and Conclusions

We have identified the star V1174 Ori as a previously unknown, double-lined, spectroscopic, pre-main-sequence (PMS) eclipsing binary system in the Orion star-forming region.

From high-cadence, multi-epoch, multi-band, time-series photometry spanning 2900 days, we find the period of the system to be 2.634727 days. From multi-epoch, high-resolution spectroscopy, we determine a precise, double-lined orbit solution which constrains the absolute masses of the primary and secondary components to be $1.01 M_{\odot}$ and $0.73 M_{\odot}$, respectively, accurate to $\sim 1\%$. Synthetic light-curve modeling and analysis provides absolute stellar dimensions. We find the stars to have radii of $1.34 R_{\odot}$ and $1.06 R_{\odot}$, respectively, again with uncertainties of $\sim 1\%$. These empirical mass and radius measurements are distance-independent. The secondary is thus the lowest-mass PMS star yet discovered in an eclipsing binary system, and the first sub-solar PMS star with an empirically determined mass accurate to better than a few percent.

We determine the distance to the system to be ~ 400 pc which, together with the system's center-of-mass radial velocity, makes V1174 Ori a likely member of the Ori OB1c region. It is therefore likely slightly in the foreground of, and slightly older than, the Orion Nebula Cluster (ONC) proper. Given the spread of available estimates for the bolometric magnitude of the Sun, we cannot currently constrain the absolute distance to V1174 Ori more stringently.

Analysis of the system colors suggests the presence of an unseen tertiary companion in a wide orbit. Follow-up photometry in the near-IR is underway, and should reveal substantial third light, which we predict to be $\sim 30\%$ in J .

We compare the empirically determined stellar dimensions with a variety of PMS stellar evolution models in both the H-R diagram (T_{eff} , L plane) and the mass-radius plane. In all cases, the models yield an age for V1174 Ori of $\sim 5\text{--}10$ Myr, consistent with membership in the slightly evolved Ori OB1c region, just in the foreground of the ONC.

While all of the models predict the slope of the mass-radius relationship reasonably well, those with less efficient convection (i.e. small convection parameter α) are the most consistent with our measurements, even though larger values of α are required to match the present-day Sun. While some models are consistent with the mass of the V1174 Ori primary, and others are consistent

with the mass of the V1174 Ori secondary, none of the models correctly predict the masses of both stars simultaneously. This appears to be the result of the theoretical mass tracks between 0.7–1.0 M_{\odot} being too compressed in T_{eff} relative to the components of V1174 Ori. Recent models by Montalbán et al. (2003) employing the ATLAS9 atmospheres of Heiter et al. (2002) seem to show a larger spread of T_{eff} in this mass range, and could possibly fit both components of V1174 Ori, but these models do not presently extend to masses low enough to test against the V1174 Ori secondary.

Potential problems with the T_{eff} scale are also implicated by a curious effect in which the theoretical tracks and the empirical measurements translate differently between the mass-radius plane and the H-R diagram. Some of the tracks show the components of V1174 Ori to be coeval in the H-R diagram but non-coeval in the mass-radius plane, and vice-versa for others.

Analysis of the H-R diagram positions of all PMS stars with empirical mass measurements yields mixed results for all of the PMS models we examined, with no one set of models clearly superior to the others. However, the ensemble of observations appear to be least compatible with the tracks of Siess, Dufour, & Forestini (2000), which have the hottest and most compressed T_{eff} scale of any of the tracks we examined. Again, the ATLAS9-based models of Montalbán et al. (2003) show promise of being able to reproduce most of the empirical measurements, and we encourage the extension of these models to lower T_{eff} .

We have carefully scrutinized the ensemble of empirical PMS mass measurements for consistency with one another, independent of the models. Encouragingly, we find instances of superb agreement between independent mass determinations, such as V1174 Ori A and LkCa 15 (a single star in Taurus), which have identical masses and are at identical positions in the H-R diagram. But, disconcertingly, we also find instances of apparent contradiction, such as V1174 Ori B and DM Tau, which are at similar (though not identical) positions in the H-R diagram yet have very different masses.

These apparently discordant empirical measurements may be reconcilable, however. PMS evolutionary models that are double-valued in T_{eff} , such as the ATLAS9-based models of Montalbán et al. (2003), may in fact predict the H-R diagram positions observed for these stars. In some cases, such as the astrometric binary NTT 045251+3016 and the eclipsing binary RXJ0529.4+0041, we reconcile the disagreements by adjusting the masses of the stars within the uncertainties. In another case—the single star DL Tau—we find compelling evidence in the form of an anomalous Li abundance that the reported mass is incorrect, most likely the result of a systematic error in the assumed distance.

Indeed, we find that the ensemble of PMS stars with empirical mass determinations possess a remarkably well-defined pattern of Li depletion as a function of stellar mass. The mild amount of depletion observed in the lowest-mass star, V1174 Ori B, strongly constrains the efficiency of convection that can be acting in the interiors of these stars, and argues strongly in favor of models with small convection parameters, α . Thus, as argued by D’Antona & Montalbán (2003), Li

abundance determinations in PMS stars promise to provide an important observational window into the interior structure of PMS stars. And, as we have shown in the case of DL Tau, Li can provide a valuable means for triangulating against the dynamical masses of these stars in the presence of systematic errors.

We acknowledge the support of a Hubble Fellowship (KGS) and NSF grant AST-0098417 (RDM). We also gratefully acknowledge support from the Brazilian institutions CNPq, FAPEMIG, and CAPES (LPRV). We are grateful to the staff of the Hobby Eberly Telescope (HET), particularly M. Shetrone, for generous assistance with the reduction of the HRS spectra, which were obtained through the first NOAO community program on the HET HRS, and D. Bell for patient support in coordination of this program which spanned multiple observing seasons. We are also grateful to NOAO for its commitment to maintaining community access to the small telescopes upon which this project relied heavily. Finally, we thank J. Montalbán for illuminating discussions on the PMS evolutionary models and for providing new model calculations in advance of publication.

REFERENCES

Alencar, S. H. P., Melo, C. H. F., Dullemond, C. P., Andersen, J., Batalha, C., Vaz, L. P. R., & Mathieu, R. D. 2003, *A&A*, 409, 1037

Alencar, S.H.P. & Vaz, L.P.R. 1997, *A&A* 326, 257

Alencar, S.H.P., Vaz, L.P.R., & Nordlund Å. 1999, *A&A* 346, 556

Alexander, D. R. & Ferguson, J. W. 1994, *ApJ*, 437, 879

Andersen, J. 1991, *A&A Rev.*, 3, 91

Ali, B. & Depoy, D. L. 1995, *AJ*, 109, 709

Anthony-Twarog, B. J. 1982, *AJ*, 87, 1213

Bally, J., O'Dell, C. R., & McCaughrean, M. J. 2000, *AJ*, 119, 2919

Baraffe, I., Chabrier, G., Allard, F., & Hauschildt, P. H. 1998, *A&A*, 337, 403

Basri, G. & Batalha, C. 1990, *ApJ*, 363, 654

Basri, G., Martín, E. L., & Bertout, C. 1991, *A&A*, 252, 625

Blaauw, A. 1964, *ARA&A*, 2, 213

Brown, A. G. A., de Geus, E. J., & de Zeeuw, P. T. 1994, *A&A*, 289, 101

Buser R. & Kurucz R.L., 1992, *A&A* 264, 557

Caloi, V., D'Antona, F., & Mazzitelli, I. 1997, *A&A*, 320, 823

Canuto, V. M., Goldman, I., & Mazzitelli, I. 1996, *ApJ*, 473, 550

Carpenter, J. M., Hillenbrand, L. A., & Skrutskie, M. F. 2001, *AJ*, 121, 3160

Casey B.W., Mathieu R.D., Vaz L.P.R., Andersen J. & Suntzeff N.B., 1997, *AJ* 115, 1617

Casey, B. W., Mathieu, R. D., Vaz, L. P. R., Andersen, J., & Suntzeff, N. B. 1998, *AJ*, 115, 1617

Covino, E., et al. 2000, *A&A*, 361, L49

D'Antona, F. & Mazzitelli, I. 1997, *Memorie della Societa Astronomica Italiana*, 68, 807

D'Antona, F. & Montalban, J. 2003, *A&A*, in press

Dolan, C. J. & Mathieu, R. D. 1999, *AJ*, 118, 2409

Feigelson, E. D., Broos, P., Gaffney, J. A., Garmire, G., Hillenbrand, L. A., Pravdo, S. H., Townsley, L., & Tsuboi, Y. 2002, *ApJ*, 574, 258

Geier, S., Wendker, H. J., & Wisotzki, L. 1995, *A&A*, 299, 39

Genzel, R. et al. 1981, *ApJ*, 247, 1039

Hauschildt, P. H., Allard, F., & Baron, E. 1999, *ApJ*, 512, 377

Heiter, U. et al. 2002, *A&A*, 392, 619

Herbst, W., Bailer-Jones, C. A. L., Mundt, R., Meisenheimer, K., & Wackermann, R. 2002, *A&A*, 396, 513

Hillenbrand, L. A. 1997, *AJ*, 113, 1733

Honeycutt, R. K. 1992, *PASP*, 104, 435

Iglesias, C. A. & Rogers, F. J. 1996, *ApJ*, 464, 943

Kallrath J. & Linnel A.P., 1987, *ApJ* 313, 346

Kenyon, S. J. & Hartmann, L. 1995, *ApJS*, 101, 117

Kurucz R.L. 1991, *Stellar Atmospheres: Beyond Classical Models*. eds. Crivallery L., Hibeny I., Hammer D.G., NATO ASI Series, Kluwer, Dordrecht

Lee, C. 1992, Ph.D. Thesis, University of Wisconsin

Luhman, K. L., Stauffer, J. R., Muench, A. A., Rieke, G. H., Lada, E. A., Bouvier, J., & Lada, C. J. 2003, *ApJ*, 593, 1093

Martin, E. L., Rebolo, R., Magazzu, A., & Pavlenko, Y. V. 1994, A&A, 282, 503

Mochnacki S.W., 1984, ApJS 55, 551

Montalban, J., D'Antona, F., Kupka, F., & Heiter, U. 2003, A&A, submitted

Muench, A. A., Lada, E. A., Lada, C. J., & Alves, J. 2002, ApJ, 573, 366

Oláh K., Jurcsik J., & Strassmeier K.G., 2003, A&A 410, 685

Palla, F. & Stahler, S. W. 1999, ApJ, 525, 772

Palla, F. & Stahler, S. W. 2001, ApJ, 553, 299

Parenago, P. P. 1954, Trudy Gosudarstvennogo Astronomicheskogo Instituta, 25, 1

Pavlenko, Y. V. & Magazzu, A. 1996, A&A, 311, 961

Plez B. 1992, A&A, 94, 527

Popper, D. M. 1987, ApJ, 313, L81

Popper, D. M. 1980, ARA&A, 18, 115

Rebull, L. M. 2001, AJ, 121, 1676

Rebull, L. M., et al. 2000, AJ, 119, 3026

Rossiter, R. A. 1924, ApJ, 60, 15

Schlesinger, F. 1909, Publ. Allegheny Obs., 1, 134

Schmidt-Kaler, T. 1982, in Landolt-Bornstein, Group VI, Vol. 2, ed. K.-H. Hellwege (Berlin: Springer) 454

Siess, L., Dufour, E., & Forestini, M. 2000, A&A, 358, 593

Simon, M., Dutrey, A., & Guilloteau, S. 2000, ApJ, 545, 1034

Stahler, S. W. 1983, ApJ, 274, 822

Stassun, K. G., Mathieu, R. D., Mazeh, T., & Vrba, F. J. 1999, AJ, 117, 2941 (SMMV)

Steffen, A. T. et al. 2001, AJ, 122, 997

Stellingwerf, R. F. 1978, ApJ, 224, 953

Udry, S. et al. 1999, ASP Conf. Ser. 185: IAU Colloq. 170: Precise Stellar Radial Velocities, 383

Walter, F. M., Brown, A., Mathieu, R. D., Myers, P. C., & Vrba, F. J. 1988, AJ, 96, 297

Warren, W. H. & Hesser, J. E. 1978, *ApJS*, 36, 497

White, R. J., Ghez, A. M., Reid, I. N., & Schultz, G. 1999, *ApJ*, 520, 811

Wilson R.E., 1993a, Documentation of Eclipsing Binary Computer Model (Revision of 1992 May, updated 1993 Jan), personal communication

Wilson R.E., 1993b, in *New Frontiers in Interacting Binary Star Research*, eds. K.-C. Leung & I.-S. Nha, *ASP Conference Series* 38, 91

Wilson R.E. & Devinney E.J., 1971, *ApJ* 166, 605

van Hamme W., 1993, *AJ* 106, 2096

Vaz L.P.R., Andersen J.A. & Rabello Soares M.C.A., 1995, *A&A* 301, 693

Vieira L.A., MSc Dissertation, Departamento de Física, Universidade Federal de Minas Gerais

Table 7. Radial velocities of HD 26162

# ^a	Radial Velocity (km/s)
1	25.03 ± 0.08
2	25.33 ± 0.08
3	25.17 ± 0.07
4	24.76 ± 0.07
5	23.61 ± 0.08
6	25.20 ± 0.07
7	25.35 ± 0.07
9	25.51 ± 0.07
10	25.38 ± 0.07
11	24.96 ± 0.08
12	24.74 ± 0.09
13	24.33 ± 0.07
14	25.24 ± 0.07
15	25.49 ± 0.08

^aSee Table 3.

Table 8. Final light curve solution for V1174 Ori

parameter	value	parameter	value
i (°)	86.974 ± 0.035	r_A pole	0.1384 ± 0.0006
Ω_A	7.942 ± 0.026	point	0.1392 ± 0.0006
Ω_B	7.705 ± 0.022	side	0.1387 ± 0.0006
TA (K)	4470. (fixed)	back	0.1391 ± 0.0006
TB (K)	3615.0 ± 9.5	r_B pole	0.1101 ± 0.0012
$L_3(I)$ (%)	9.90 ± 0.71	point	0.1106 ± 0.0012
$L_3(V)$ (%)	0.00 (fixed)	side	0.1103 ± 0.0012
$L_3(y)$ (%)	1.73 ± 0.65	back	0.1106 ± 0.0012
$L_3(b)$ (%)	0.03 ± 0.65	$F_{out,A}$	0.4247 ± 0.0012
$L_3(v)$ (%)	2.47 ± 0.66	$F_{out,B}$	0.4548 ± 0.0014
$v_{ratio,A}$	1.017 ± 0.026		
$v_{ratio,B}$	1.001 ± 0.079		

Note. — WD solutions for V1174 Ori, based on the observations from Jan 2001. Parameters like the limb darkening coefficients, gravity darkening exponents, and surface gravities were kept consistent during iterations. The solutions were attained by combining both the least-squares and the SIMPLEX methods. The errors quoted are the internal least-squares estimations, which are typically around 3-5 times larger than those estimated from the vertices of the SIMPLEX hyperpolyhedron after convergence. The third light contributions are given as percentages of the eclipsing system total light at the normalization phase (0.25). The radii resulting from the gravitational effective equipotentials (in terms of the orbital separation) and the fill-out factors, F_{out} (Mochnacki 1984), are given, which indicate that the eclipsing components are well inside their Roche lobes. The errors quoted on the radii and fill-out factors represent the deviations caused by the uncertainties in the pseudopotentials and in the mass ratio. The rotation rates, calculated from the solutions and the measurements of §4.3.1 are shown, justifying the assumption of synchronism with the orbit.

Table 9. Spot parameters used in light curve solutions

epoch	bands	spot/star	co-latitude (°)	longitude (°)	radius (°)	T_{factor}
Dec/1994	<i>I</i>	1 / A	69. \pm 13.	140.5 \pm 8.6	7.2 \pm 1.6	0.69 \pm 0.24
		1 / B	70.4 \pm 7.3	25.3 \pm 5.5	11. \pm 11.	1.44 \pm 0.32
2MASS	<i>JHK</i>	1 / A	21. \pm 16.	101.9 \pm 9.6	27. \pm 5.3	0.88 \pm 0.18
		1 / B	23. \pm 13.	336. \pm 21.	48. \pm 4.2	0.61 \pm 0.14
Jan/2001	<i>vbyVI</i>	1 / A	18.2 \pm 7.4	78. \pm 10.	15.2 \pm 4.6	1.58 \pm 0.74
		2 / A	16.2 \pm 5.7	110.8 \pm 6.2	26.0 \pm 4.7	0.76 \pm 0.25
		3 / A	13.34 \pm 0.69	159.6 \pm 1.3	31.2 \pm 1.5	0.508 \pm 0.042
		1 / B	155. \pm 10.	97.1 \pm 5.5	30.2 \pm 5.1	0.76 \pm 0.12
		2 / B	67. \pm 19.	246. \pm 10.	17.4 \pm 4.6	1.18 \pm 0.11
		3 / B	76. \pm 17.	297.4 \pm 5.6	26.0 \pm 5.6	0.662 \pm 0.091
		1 / A	48. \pm 10.	136.8 \pm 9.6	21.4 \pm 5.2	0.74 \pm 0.41
Nov/2001	<i>I</i>	1 / B	70. \pm 17.	134.6 \pm 9.7	12.4 \pm 6.6	1.45 \pm 0.91
		1 / A	22.41 \pm 0.42	93.3 \pm 7.2	31.6 \pm 1.2	0.851 \pm 0.057
Nov/2002	<i>BVI</i>	1 / B	16.35 \pm 4.1	306.1 \pm 9.1	56.1 \pm 5.7	0.69 \pm 0.11
		2 / B	21.99 \pm 4.2	348.2 \pm 9.8	44.7 \pm 8.4	0.605 \pm 0.095

Note. — The characteristics of the star spots used in the solution of the light curves from Table 1 and for the *JHK* light curves from 2MASS (one point obtained at March 19th, 1998 and 23 points from February 6th to March 28th, 2000). The spots are listed for each component in each epoch with increasing longitudes. As in Table 8, the errors quoted are those internal to the least squares method. The standard deviation of the corresponding variables of the SIMPLEX method, after convergence, are much smaller: of the order of 10^{-3} degree for the angular parameters and of 10^{-5} for the temperature factor for both components. T_{factor} gives the spot temperature in units of T_{eff} .

Table 10. Fundamental stellar properties of V1174 Ori

	Primary	Secondary
M (M_{\odot})	1.009 ± 0.015	0.731 ± 0.008
R (R_{\odot})	1.339 ± 0.015	1.065 ± 0.011
T_{eff} (K)	$4470^{\text{a}} \pm 120$	$3615^{\text{b}} \pm 100^{\text{c}}$
$\log L$ (L_{\odot})	-0.193 ± 0.048	-0.761 ± 0.058
$\log g$	4.19 ± 0.01	4.25 ± 0.01
v_{rot} (km/s)	26.2 ± 0.6	20.5 ± 1.6
A_V	0.32	
Dist. (pc)	419 ± 21	

^aFrom measured spectral type of K4.5 \pm 0.5, and SpT– T_{eff} conversion of Schmidt-Kaler (1982).

^bImplies a spectral type of M1.5.

^cNote that the internal uncertainty on T_{eff} for the secondary is minuscule. The uncertainty we assign here is inherited from the uncertainty in the determination of T_{eff} for the primary, keeping the T_{eff} ratio fixed at the value determined in §4.4.

Table 11. Parameters of PMS Evolution Models

Authors	Atmosphere	Convection	α_{atm}	α_{in}	τ_{ph}	Matches	Sun?
MDKH03	ATLAS9	FST	10	Y	
	ATLAS9	MLT	0.5	2.3	10	Y	
	NextGen	MLT	1.0	1.0	3^a	N	
BCAH98	NextGen	MLT	1.0	1.0	100	N	
	NextGen	MLT	1.0	1.9	100	Y	
PS99	gray approx.	MLT	...	1.5	$\frac{2}{3}$	N	
SDF00	Plez, Eriksson	MLT	...	1.6	10	Y	

^aThese authors have also computed NextGen-based models with $\tau_{\text{ph}} = 100$, but these are equivalent to the BCAH98 tracks.

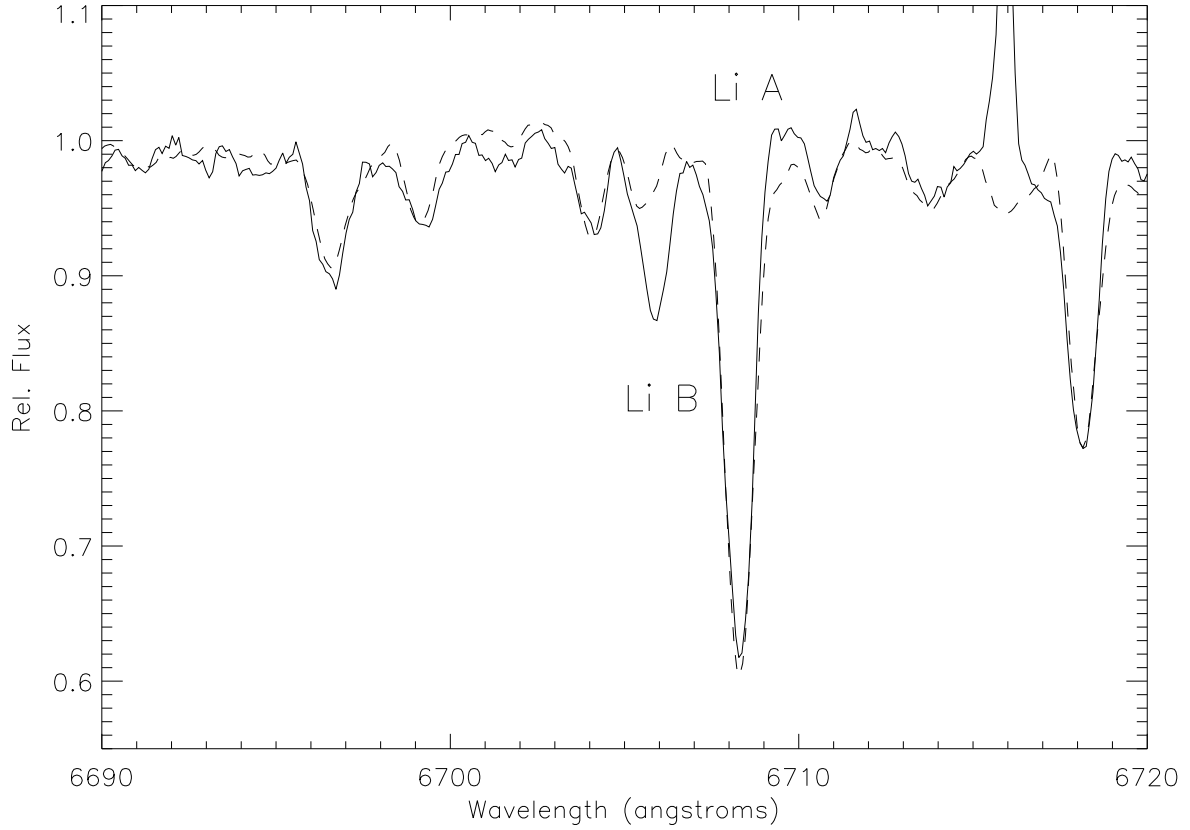


Fig. 1.— Keck HIRES spectrum of V1174 Ori, in the vicinity of the Li $\lambda 6708$ line, is shown as a solid curve. The dashed curve is a spectrum of the V1174 Ori primary, obtained by averaging together all of the HET HRS spectra. The Li line from the secondary (labeled Li B) is clearly present, in this case blueward of the primary's Li line (labeled Li A) and partially blended with an Fe line from the primary. The emission feature near $\lambda 6716$ is nebular [S II].

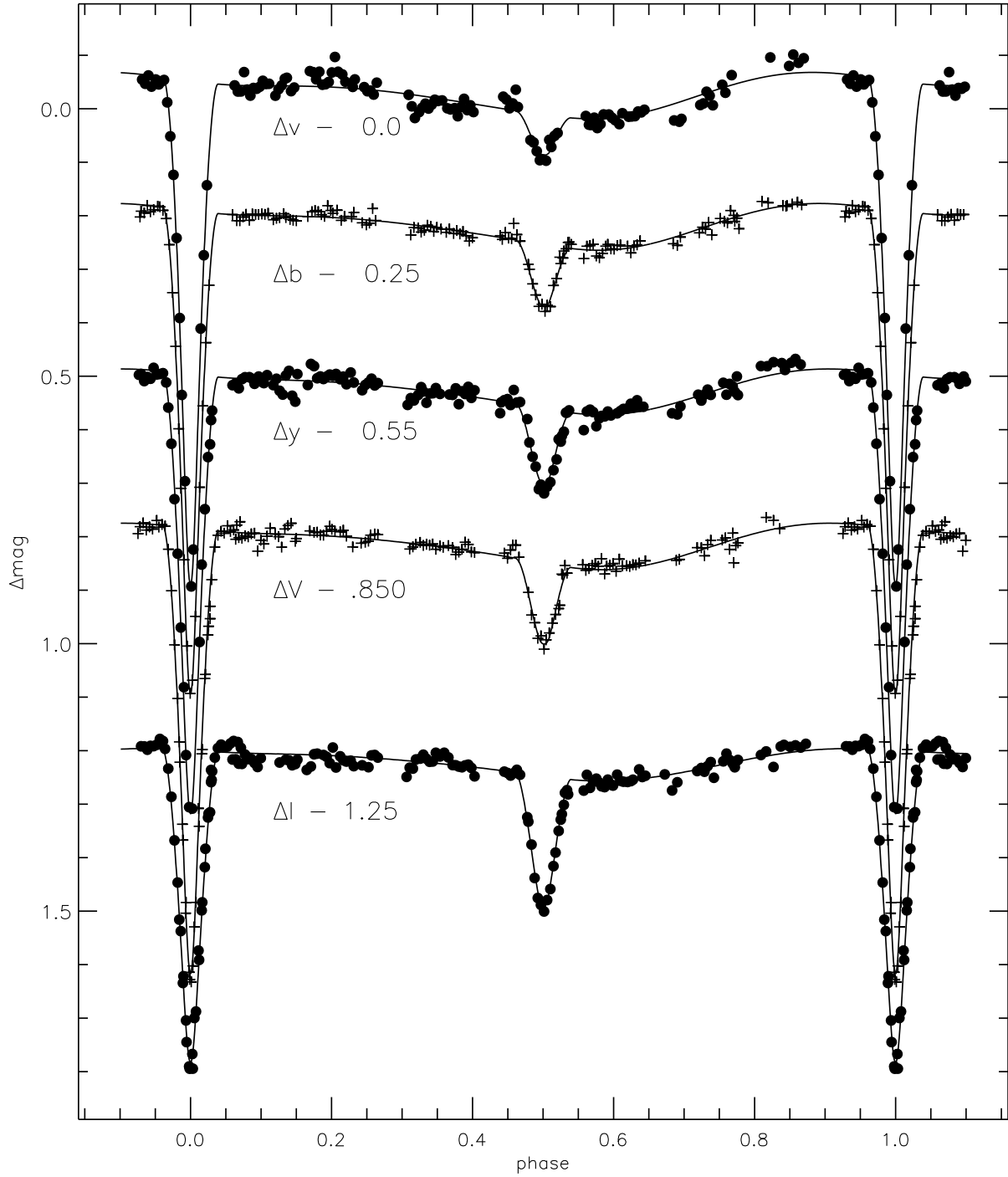


Fig. 2.— The $vbyVI$ light curves observed in Jan 2001 together with the theoretical light curves synthesized with a Wilson-Devinney based algorithm (see Tables 8 and 9). For clarity, the light curves were shifted by the amount indicated in the figure, but the relative scale is the same for all passbands. Note the changes in the depths of both eclipses with wavelength.

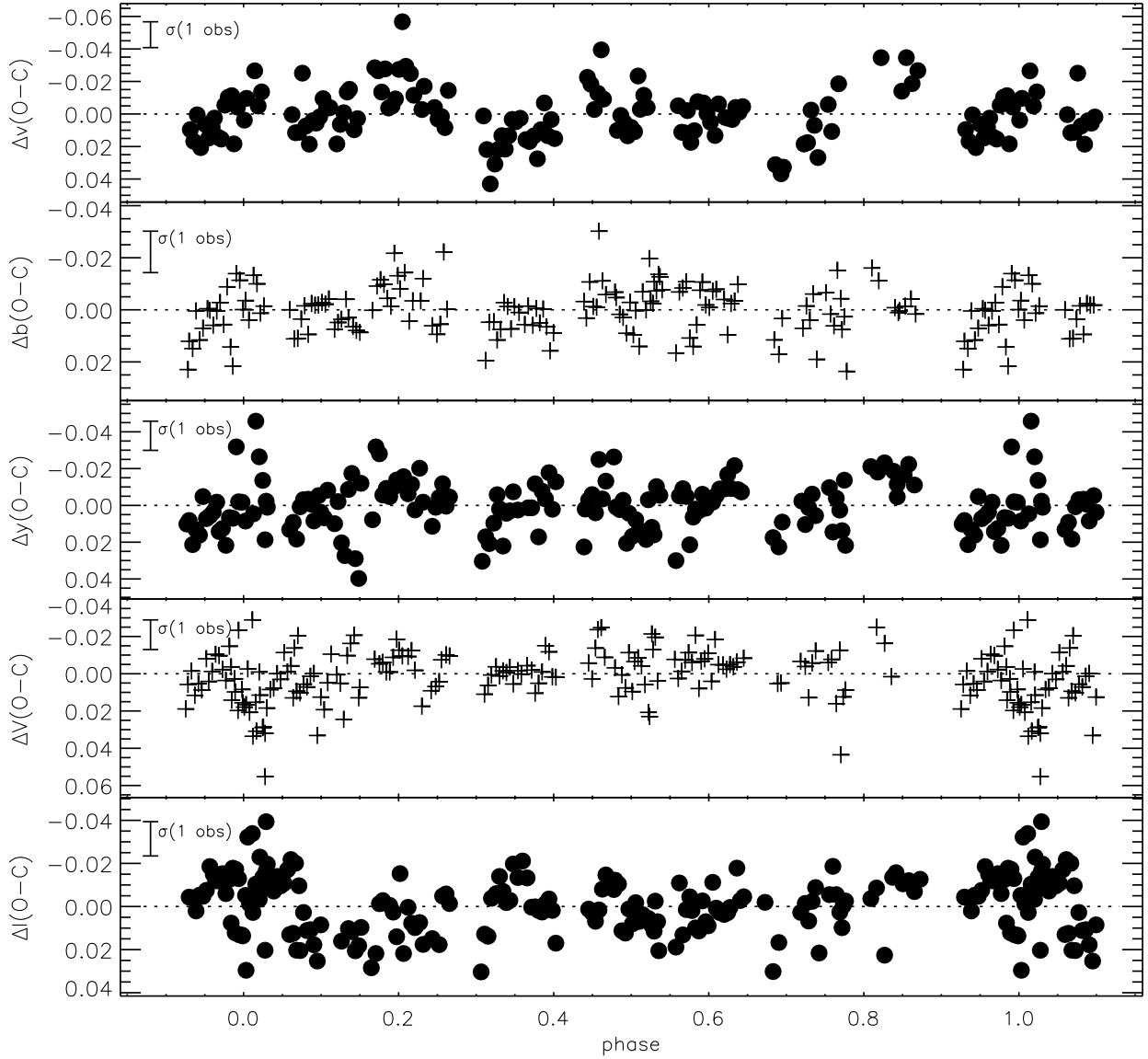


Fig. 3.— The $O - C$ residuals for the solutions of Fig. 2 and Tables 8 and 9. The vertical bar at the left of each panel is the standard deviation of the residuals.

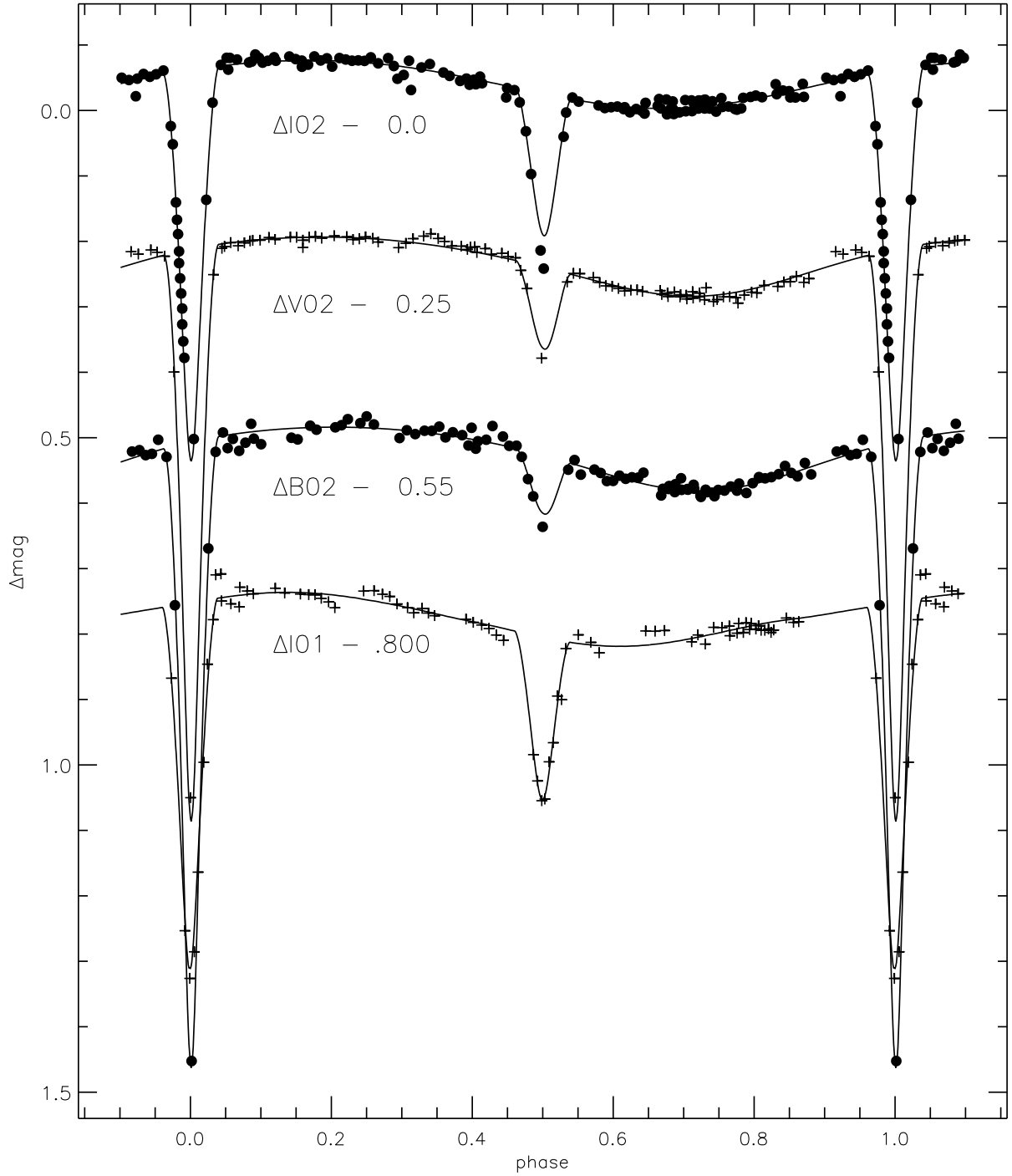


Fig. 4.— The IVB light curves observed in 2002 and the I light curve obtained in 2001 (Table 1) together with the theoretical light curves obtained with the WD algorithm (Tables 8 and 9). The light curves are shifted by the amount indicated in the figure for clarity, but the relative scale is the same for all passbands. Note the changes in the depth of both eclipses with wavelength and the clear change in the form of the light curve outside eclipse from 2001 to 2002.

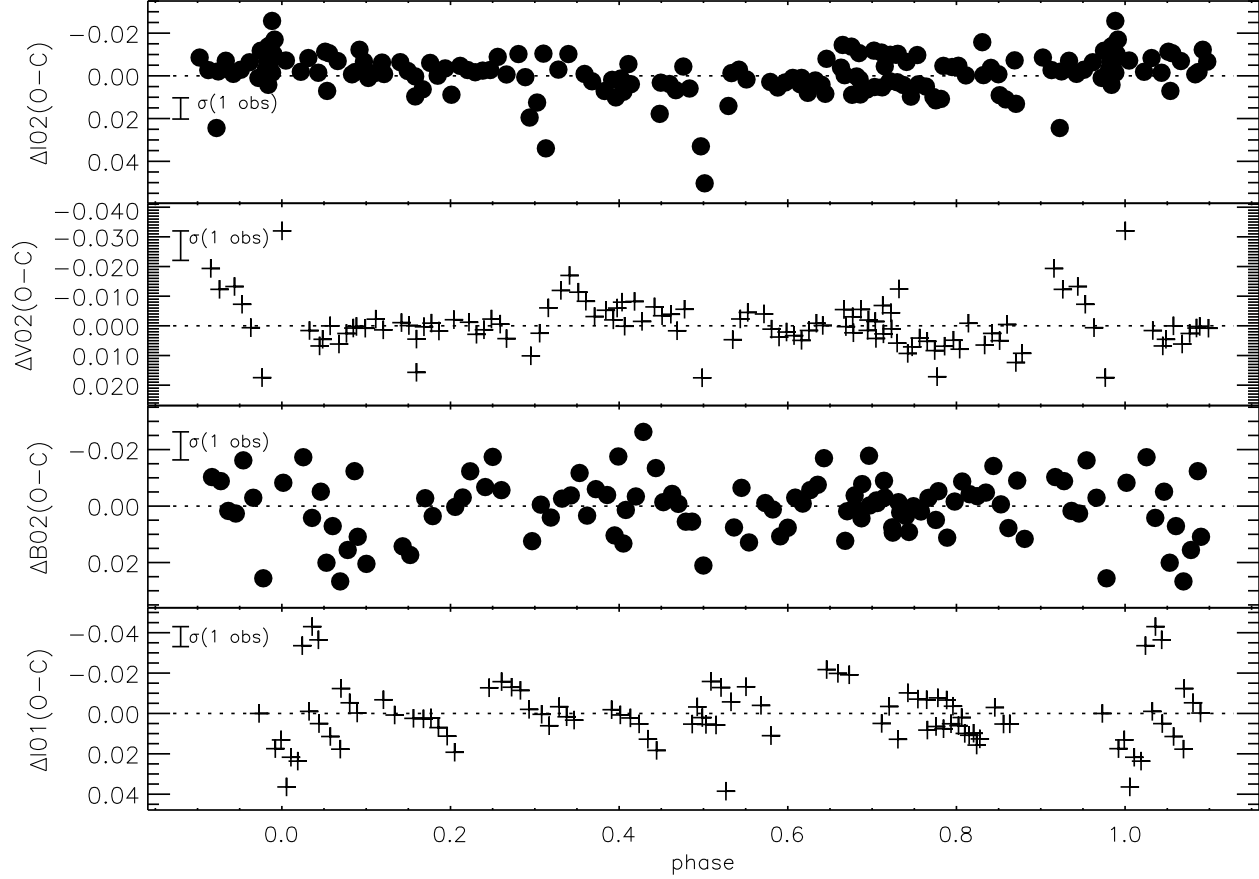


Fig. 5.— The $O - C$ residuals for the solutions of Fig. 4 and Tables 8 and 9. The vertical bar at the left of each panel is the standard deviation of the residuals.

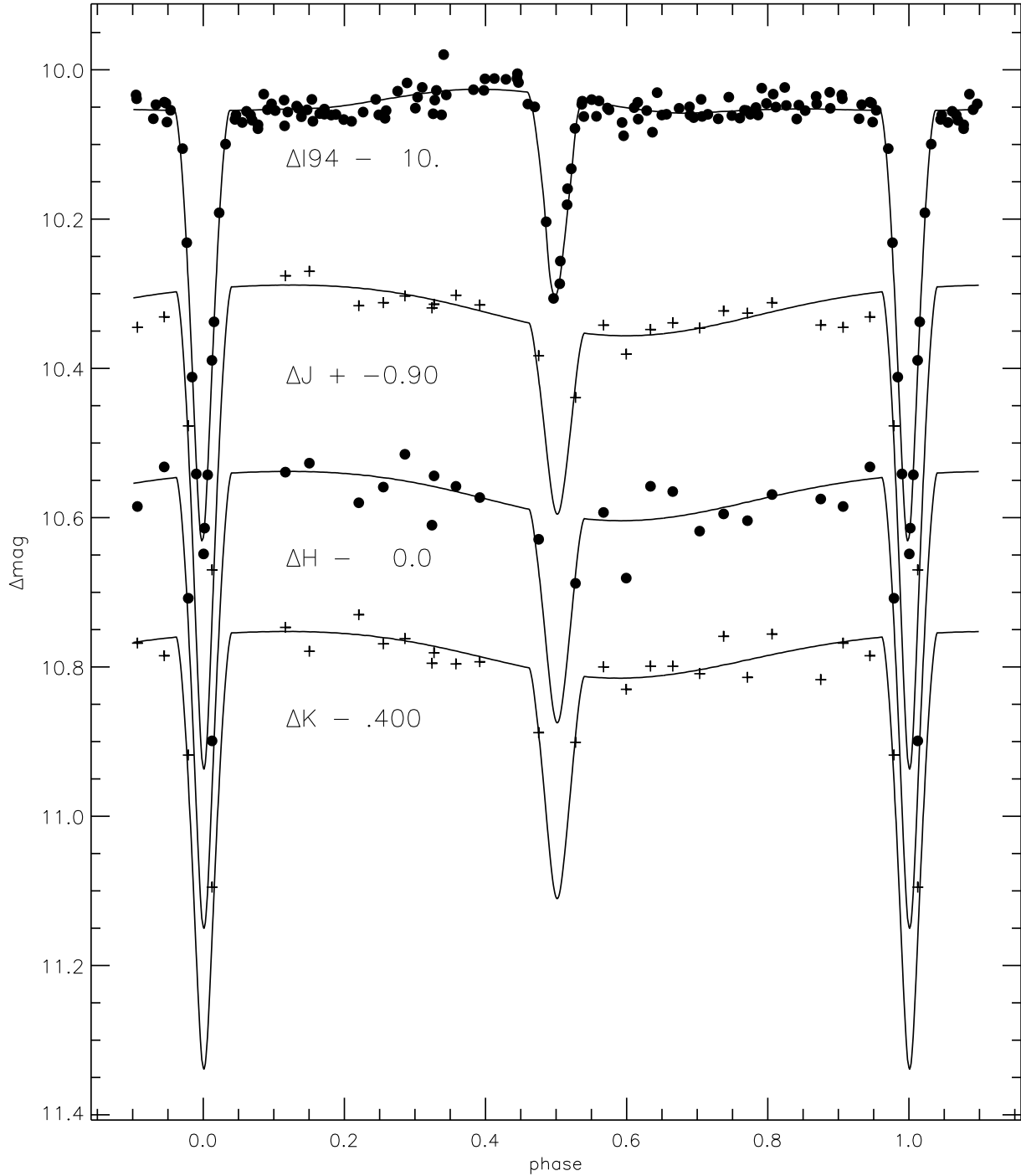


Fig. 6.— The I light curve obtained in Nov 1994 (Table 1) and the JHK light curves obtained by Carpenter, Hillenbrand, & Skrutskie (2001) together with the theoretical light curves synthesized by the WD algorithm (Tables 8 and 9). The light curves are shifted by the amount indicated in the figure for clarity, but the relative scale is the same for all passbands. Note the changes in the depth of both eclipses with wavelength and the clear change in the form of the light curves outside eclipse from 1994 to 2000.

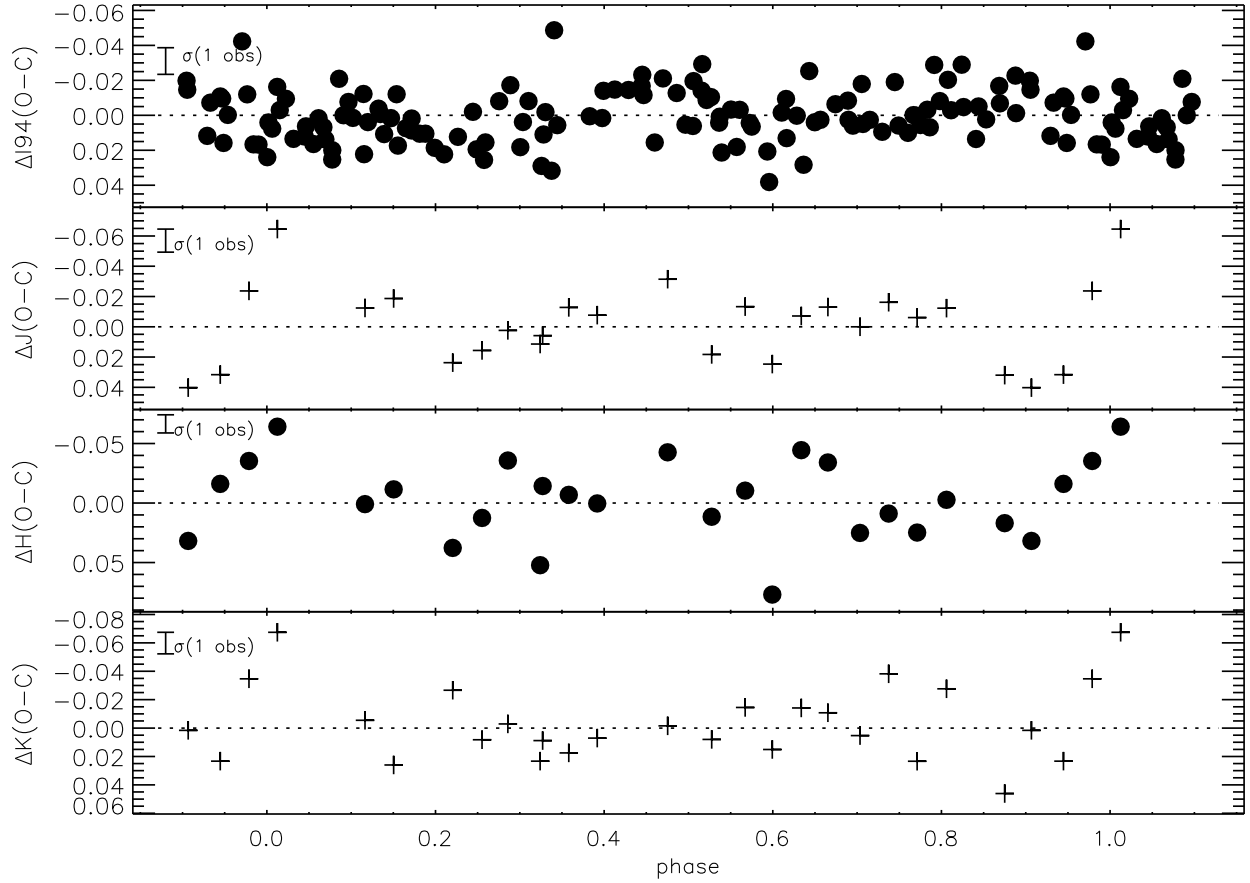


Fig. 7.— The $O - C$ residuals for the solutions of Fig. 6 and Tables 8 and 9. The vertical bar at the left of each panel is the standard deviation of the residuals.

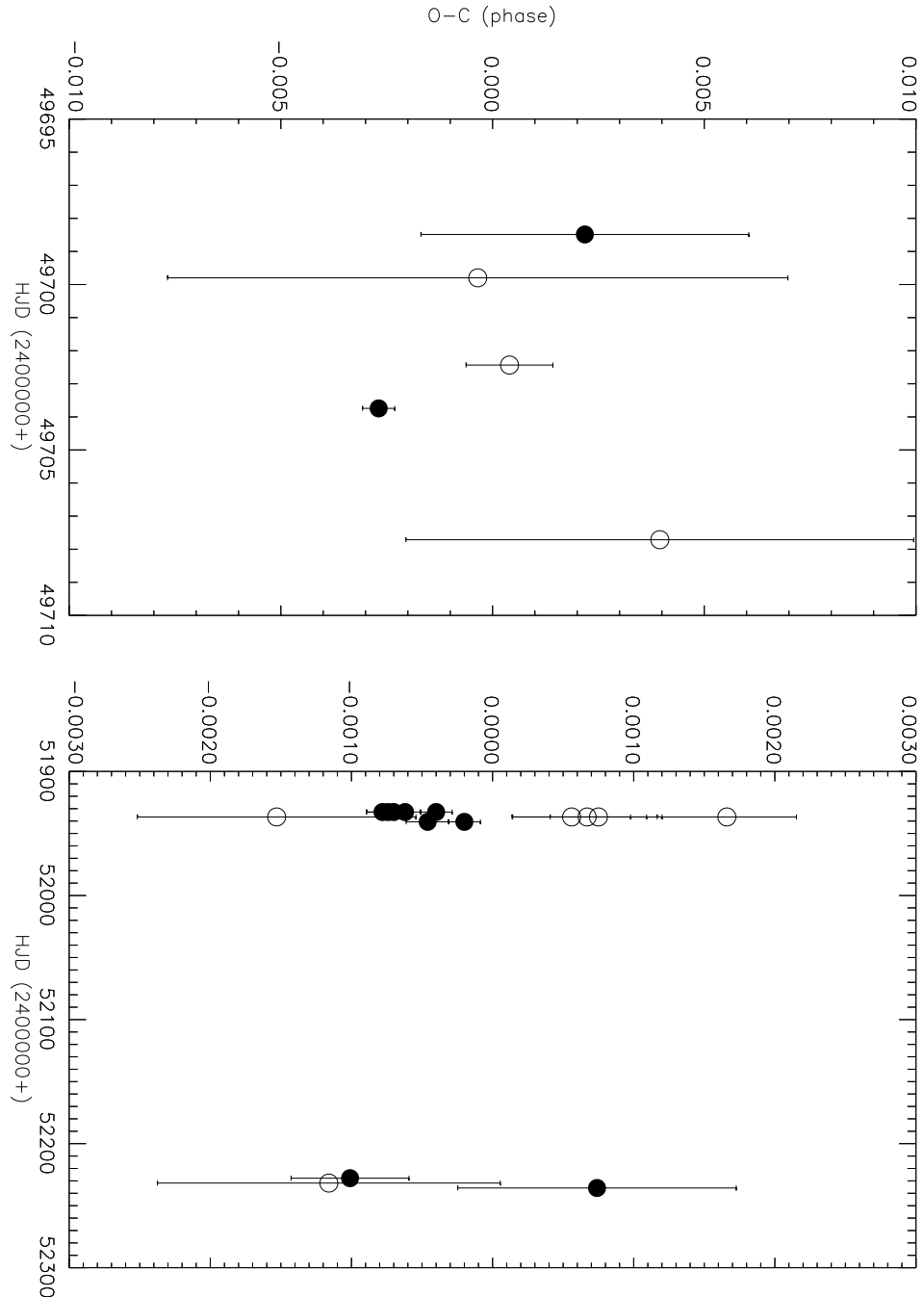


Fig. 8.— The $O - C$ phase residuals of the eclipse timings of V1174 Ori are shown based on a best-fit period of 2.634727 days. Filled circles represent primary eclipses, open circles represent secondary eclipses. See Table 4.

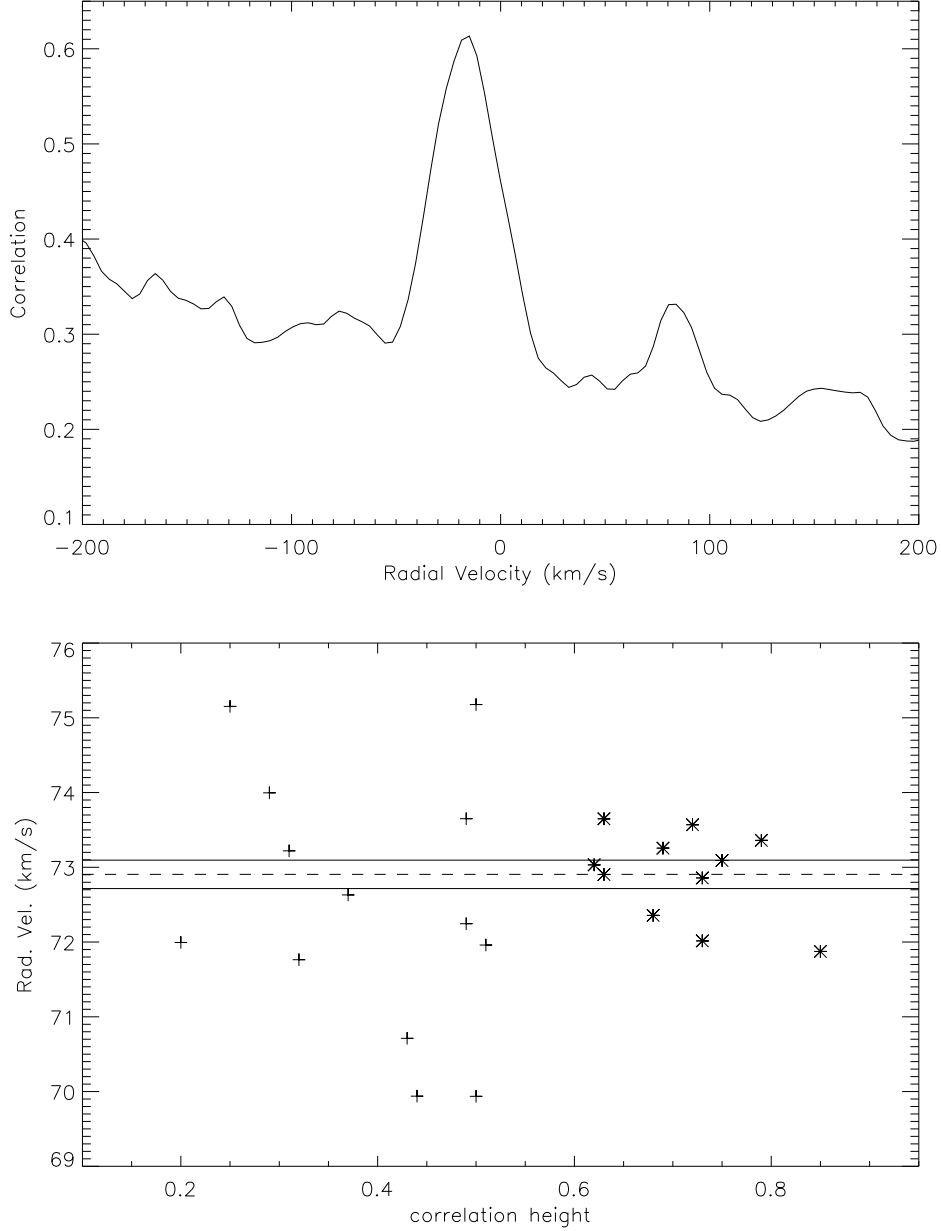


Fig. 9.— Example of our procedure for measuring radial velocities from cross-correlation. (a) Shown is the cross-correlation function from a single spectral order in the spectrum of UT 2002 Jan 28, in which we detect both the primary and the secondary peak. In a typical spectrum, most of the orders yield a velocity measurement for the primary, whereas only a few orders produce an unambiguous secondary peak, such as the one seen in this example. (b) Shown as a function of correlation peak height are the radial velocities (km/s) for the primary star. We use only velocities with correlation heights greater than 0.6 (asterisks), which we found empirically yield more reliable velocities. The horizontal lines indicate the mean velocity of the primary (72.91 km/s) and the standard deviation of the mean (0.19 km/s); see Table 5.

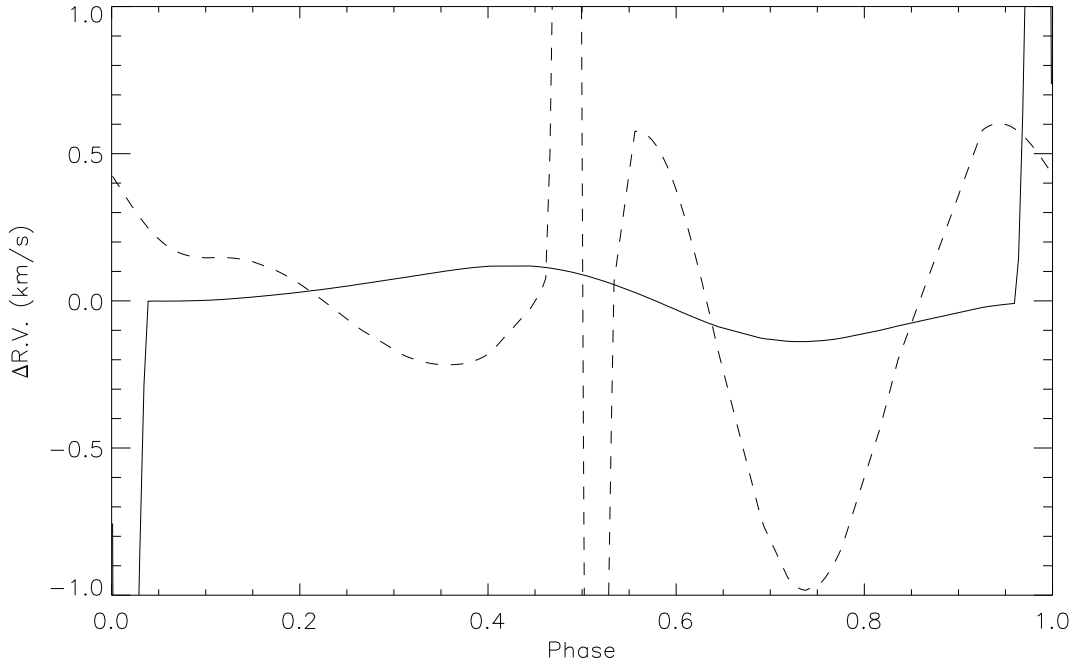


Fig. 10.— Illustration of distortions in observed radial velocities due to stellar occultation and the presence of surface spots. Distortions in the primary (secondary) star's radial velocities are shown by the solid (dashed) line. Note the strong distortion effects due to occultation at ± 0.05 phase around each eclipse (± 3.7 km/s and ± 4.8 km/s for the primary and secondary, respectively).

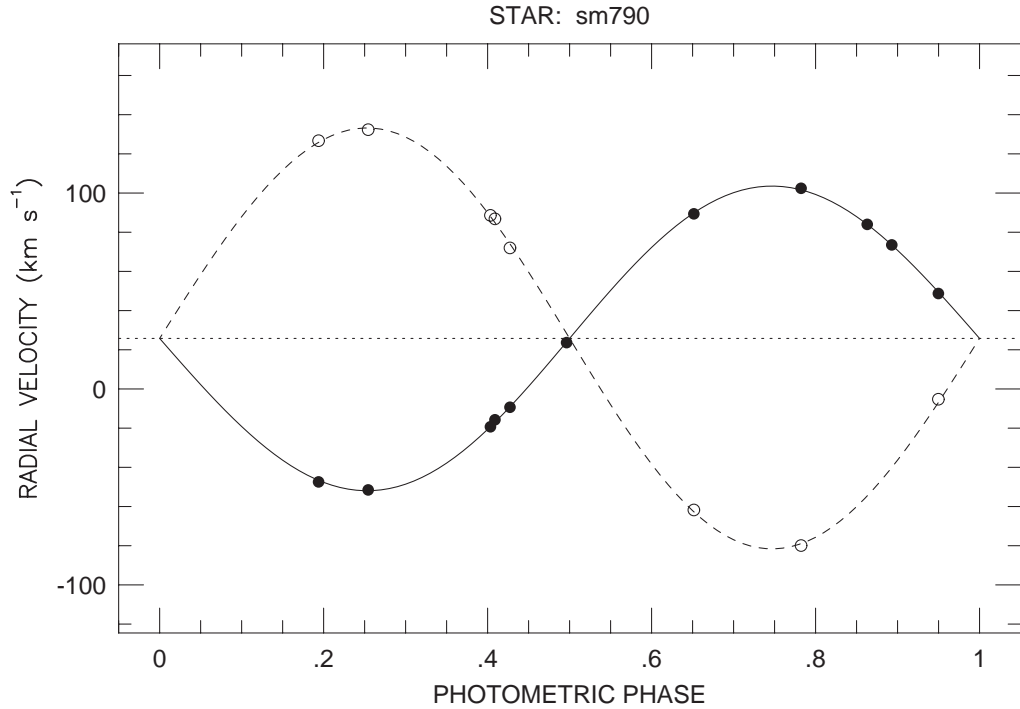


Fig. 11.— Orbit solution for V1174 Ori. Radial velocity measurements (see Table 5) for the primary (secondary) star are shown as filled (open) points. The solutions for the primary and secondary stars are shown as solid and dashed lines, respectively.

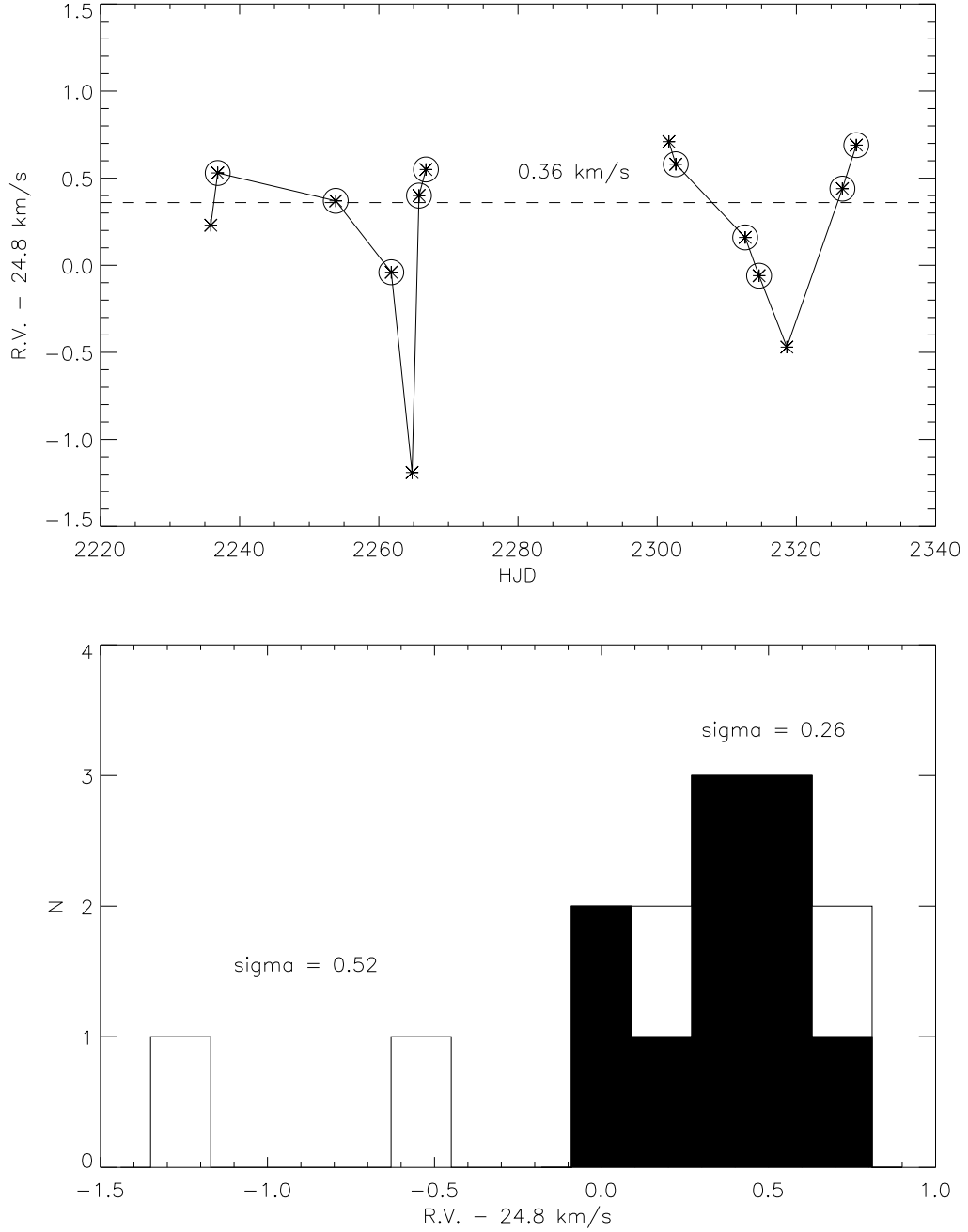


Fig. 12.— Our assessment of mechanical stability of the HET HRS. (a) Shown as a function of heliocentric Julian date are the radial velocities of the radial-velocity standard HD 26162 (see Table 5). Circled points represent spectra from the same nights that are used in our orbit solution of V1174 Ori. The horizontal dashed line indicates the mean of these points, which show a small systematic offset of 0.36 km/s, likely due to spectral mismatch between HD 26162 and the standard star (HD 18884) used in our orbit solution of V1174 Ori. (b) These same radial velocities of HD 26162 are shown as a histogram (open), with the circled points in (a) represented by the filled histogram. These latter measurements show an r.m.s. scatter of 0.26 km/s.

NOAO/IRAF V2.12.1-EXPORT keivan@A117023.N1.Vanderbilt.Edu Tue 11:31:34 04-
Separation step = 0.3

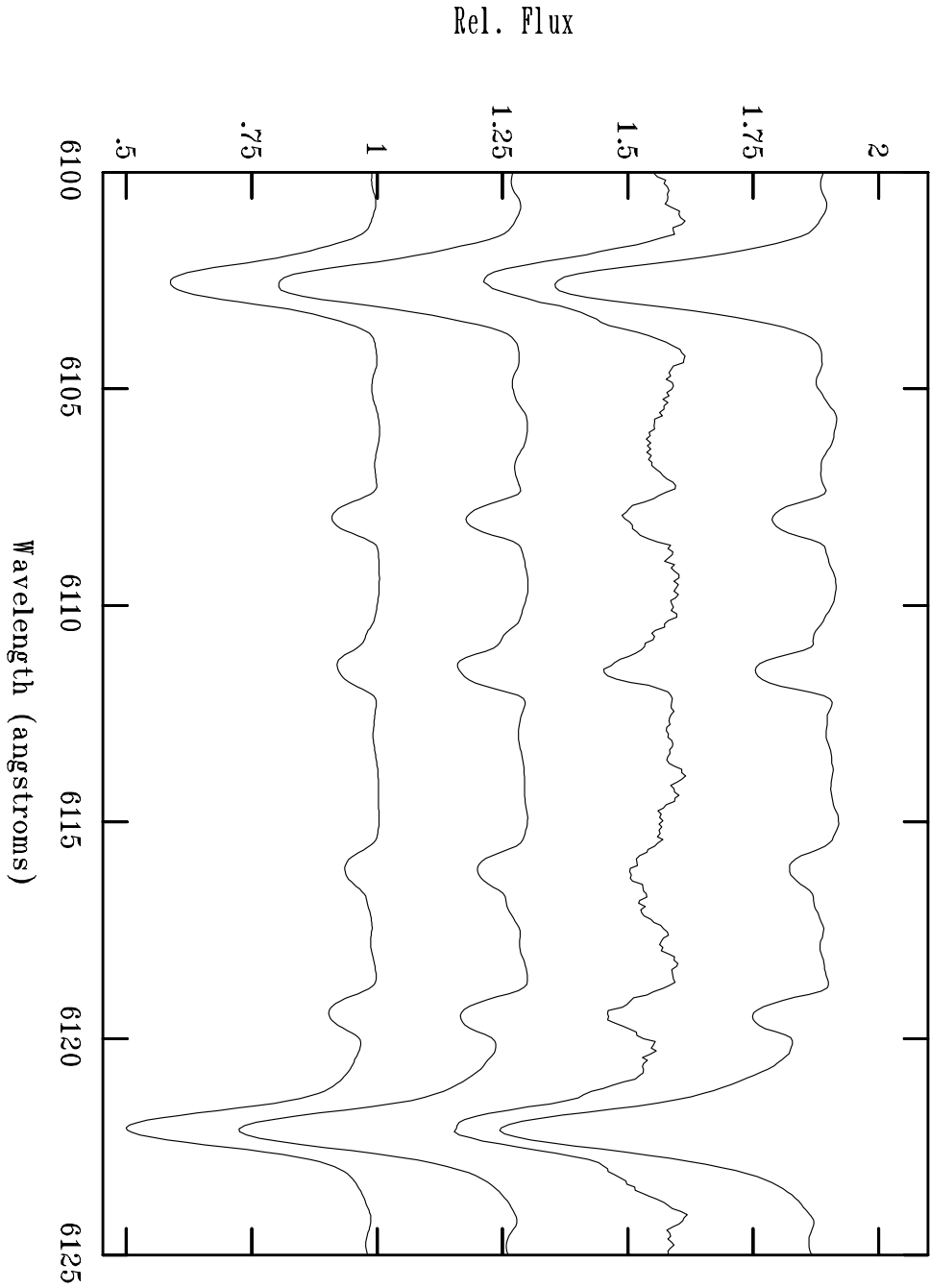


Fig. 13.— Shown is the UT 2002 Feb 07 spectrum of V1174 Ori (second from top) compared with three spectral standards of type K3 (bottom), K4 (second from bottom), and K5 (top). The spectral region shown includes the temperature-sensitive lines of Ni I at $\lambda 6108$ and V I at $\lambda 6112$, one of four line pairs that we use to determine the spectral type of the primary of V1174 Ori. Note that in this spectrum the primary star's V I is slightly contaminated by the secondary star's Ni I line. Also visible here are the temperature-insensitive lines of Ca II at $\lambda\lambda 6102, 6122$. In this spectrum of V1174 Ori, the secondary star's $\lambda 6102$ Ca II line is visible as the weak absorption feature between the primary star's $\lambda 6102$ Ca II and $\lambda 6108$ Ni I lines. The $\lambda 6102$ Ca II lines in this spectrum indicate a primary-to-secondary flux ratio of $\sim 6:1$ for V1174 Ori (see Fig. 14).

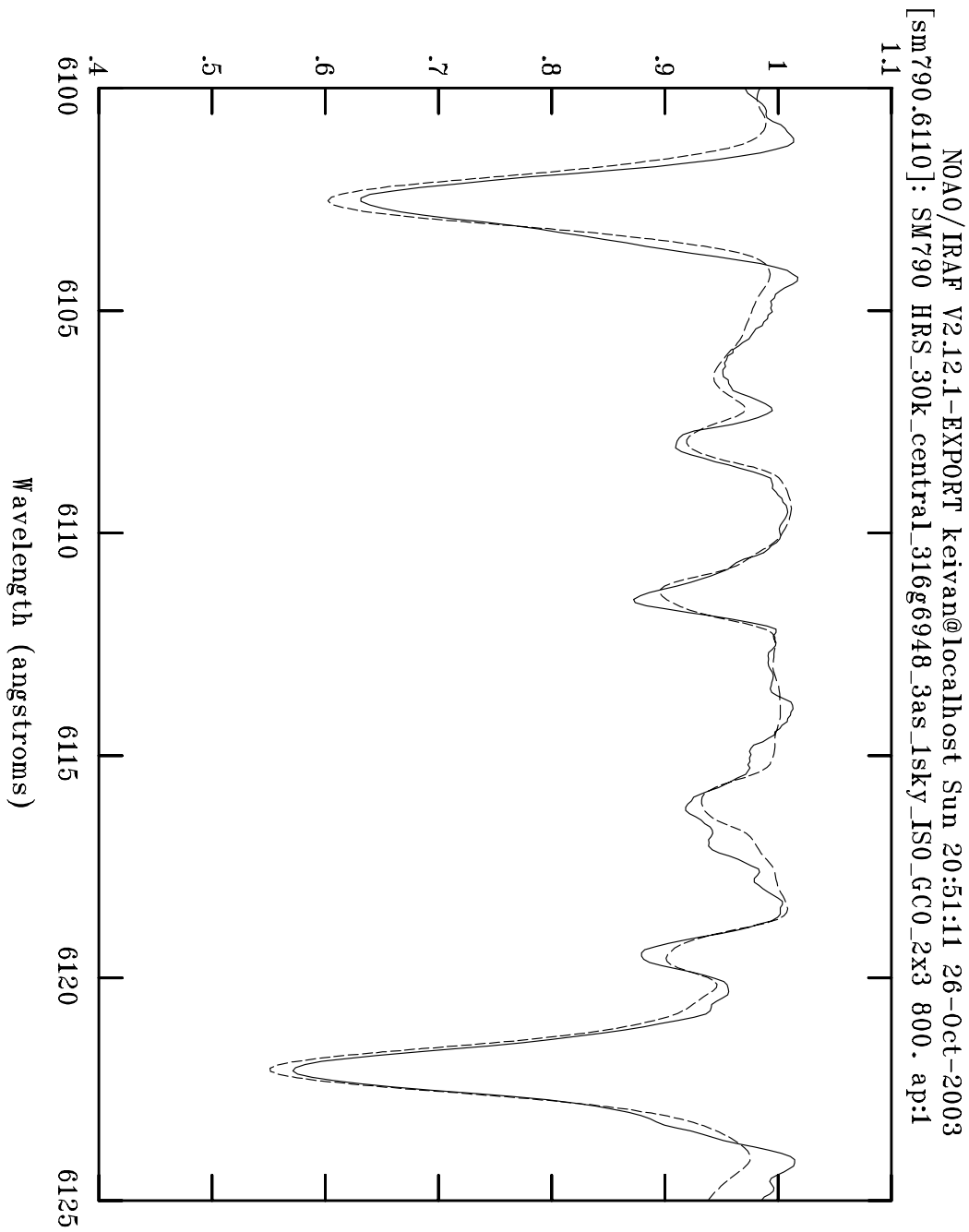


Fig. 14.— Determination of the primary-to-secondary flux ratio for V1174 Ori. The UT 2002 Feb 07 spectrum (solid line) is compared with a synthetic spectrum produced by combining the K3 and K7 standards in a 6:1 ratio (dashed line). The standards were first rotationally broadened (see §4.3.1) and shifted to the appropriate radial velocities (see Table 5).

NOAO/IRAF V2.12.1-EXPORT keivan@ctif1218.ctio.noao.edu Sun 22:11:33 22-D
 [sm790.0005]: SM790 HRS_30k_central_316g6948_3as_1sky_IS0_GC0_23x 600. ap:

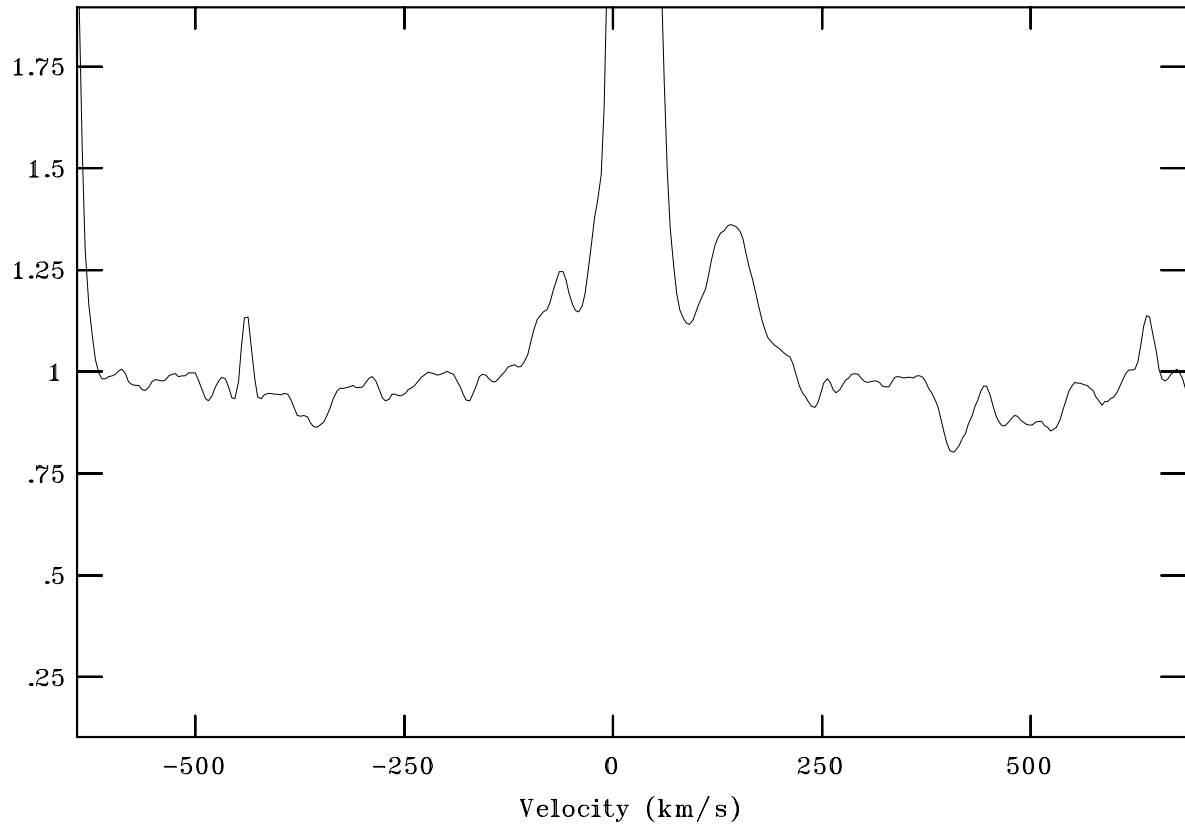


Fig. 15.— Determination of H α equivalent widths for the two components of V1174 Ori. Shown is the UT 2002 Feb 23 spectrum, plotted vs. heliocentric radial velocity. The strong emission line is nebular. Emission from the primary and secondary stars are visible just to the blue and red of the nebular line, respectively.

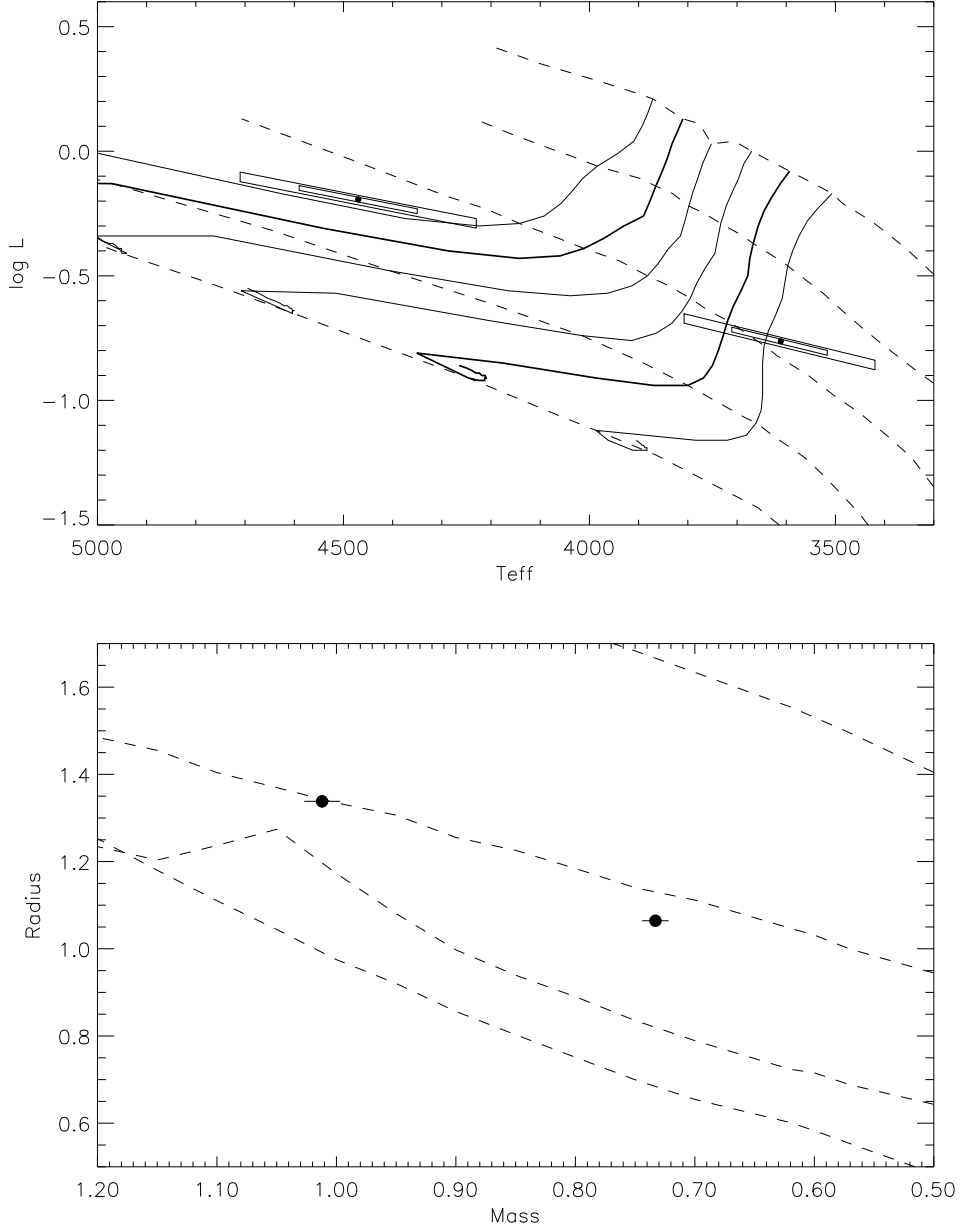


Fig. 16.— BCAH98 tracks with $l_{\text{mix}}/H_p = 1.0$. (a) H-R diagram ($\log L$ vs. T_{eff}), with isochrones at 1, 3, 10, 30, and 100 Myr, and mass tracks for 0.6, 0.7, 0.8, 0.9, 1.0, and $1.1 M_{\odot}$. Mass tracks at 0.7 and $1.0 M_{\odot}$, corresponding approximately to the masses of V1174 Ori, are thicker than the others. Points mark the best-fit values of T_{eff} and $\log L$, with nested boxes indicating confidence regions about those values. The inner box about the primary corresponds to 0.5 spectral sub-type uncertainty in T_{eff} (see §4.3.3) and 1σ uncertainty on the stellar radius. The outer box corresponds to uncertainties twice as large in each of T_{eff} and R , and should be taken as the region of high confidence for the primary. The nested boxes about the secondary are similar, but the range of T_{eff} here is determined by keeping the secondary-to-primary T_{eff} ratio fixed at the value determined from the light curve analysis (see §4.4). Note that the positions of the primary and secondary in this figure are highly correlated; adjusting the position of the primary necessarily adjusts that of the secondary. (b) Radius vs. mass in solar units. Points with error bars are the measurements for the two components of V1174 Ori; isochrones at 3, 10, 30, and 100 Myr are shown as dashed lines.

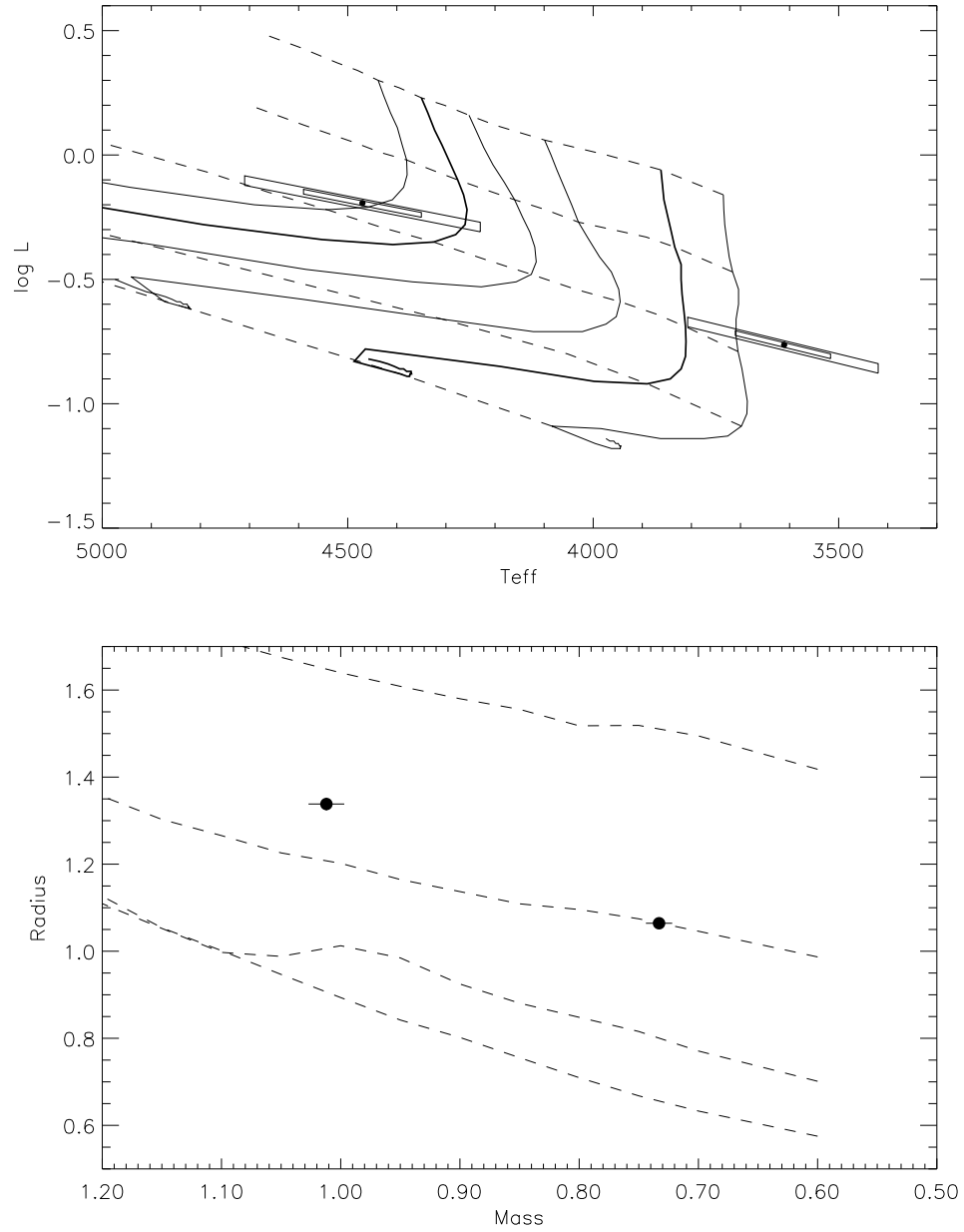


Fig. 17.— BCAH98 tracks with $l_{\text{mix}}/H_p = 1.9$. Symbols and lines are as in Fig. 16.

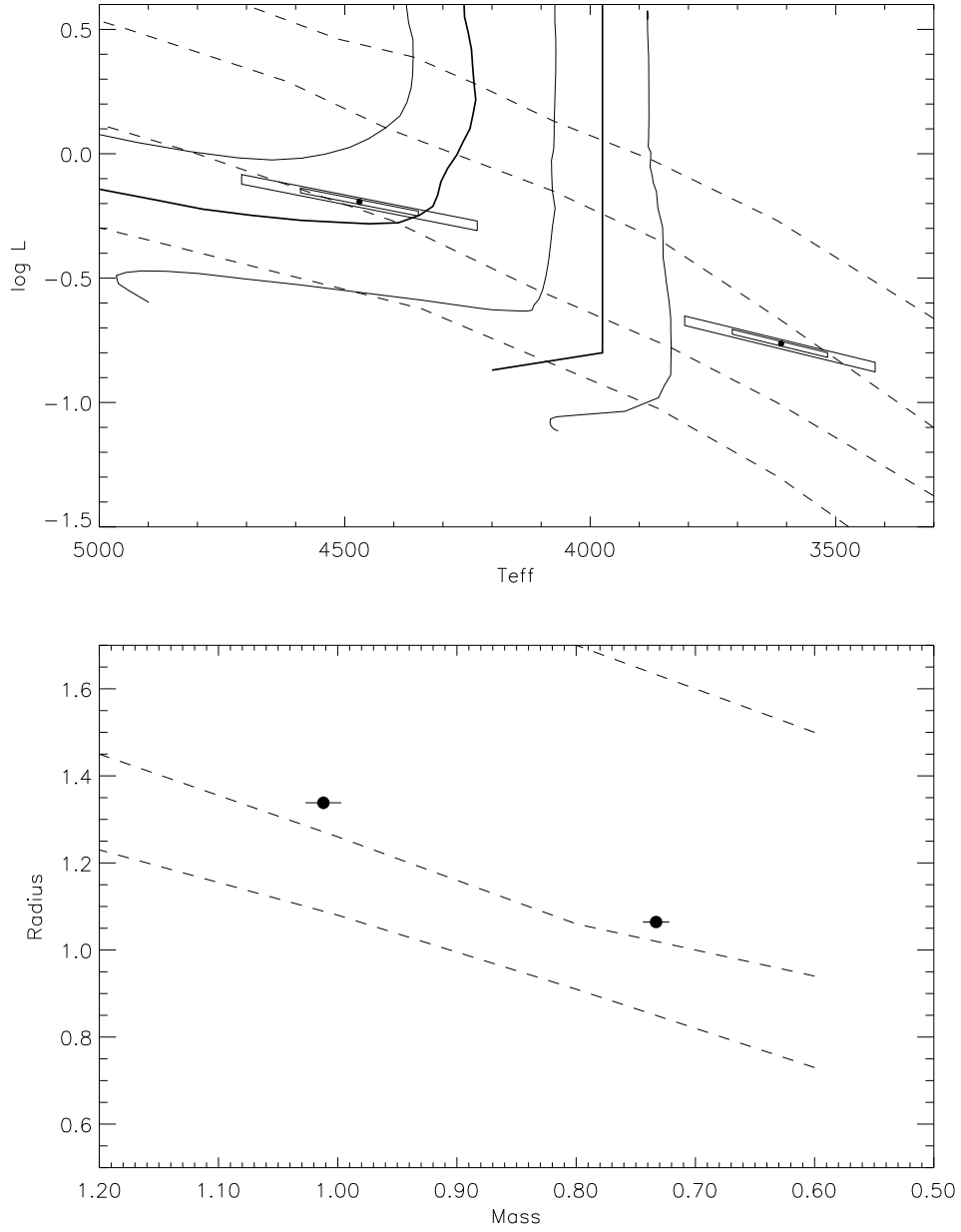


Fig. 18.— PS99 tracks. Symbols and lines are as in Fig. 16, except that (a) shows mass tracks at 0.6, 0.7, 0.8, 1.0, and 1.2 M_{\odot} and isochrones at 1, 3, 10, and 30 Myr. Note that the mass track at 0.7 M_{\odot} has been visually interpolated between the positions of the 0.6 and 0.8 M_{\odot} tracks. In (b) isochrones are shown at 3, 10, and 30 Myr.

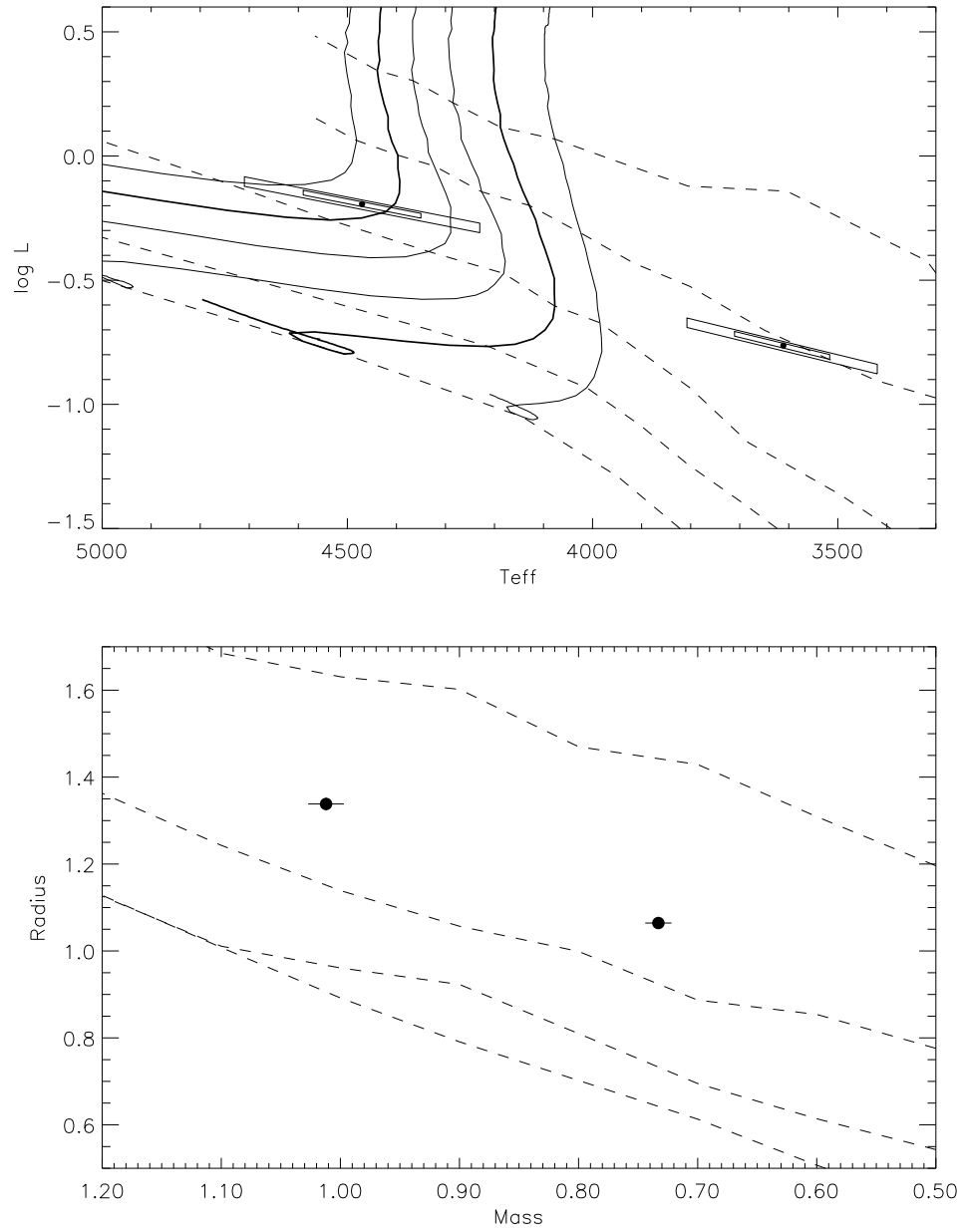


Fig. 19.— SDF00 tracks. Symbols and lines are as in Fig. 16.

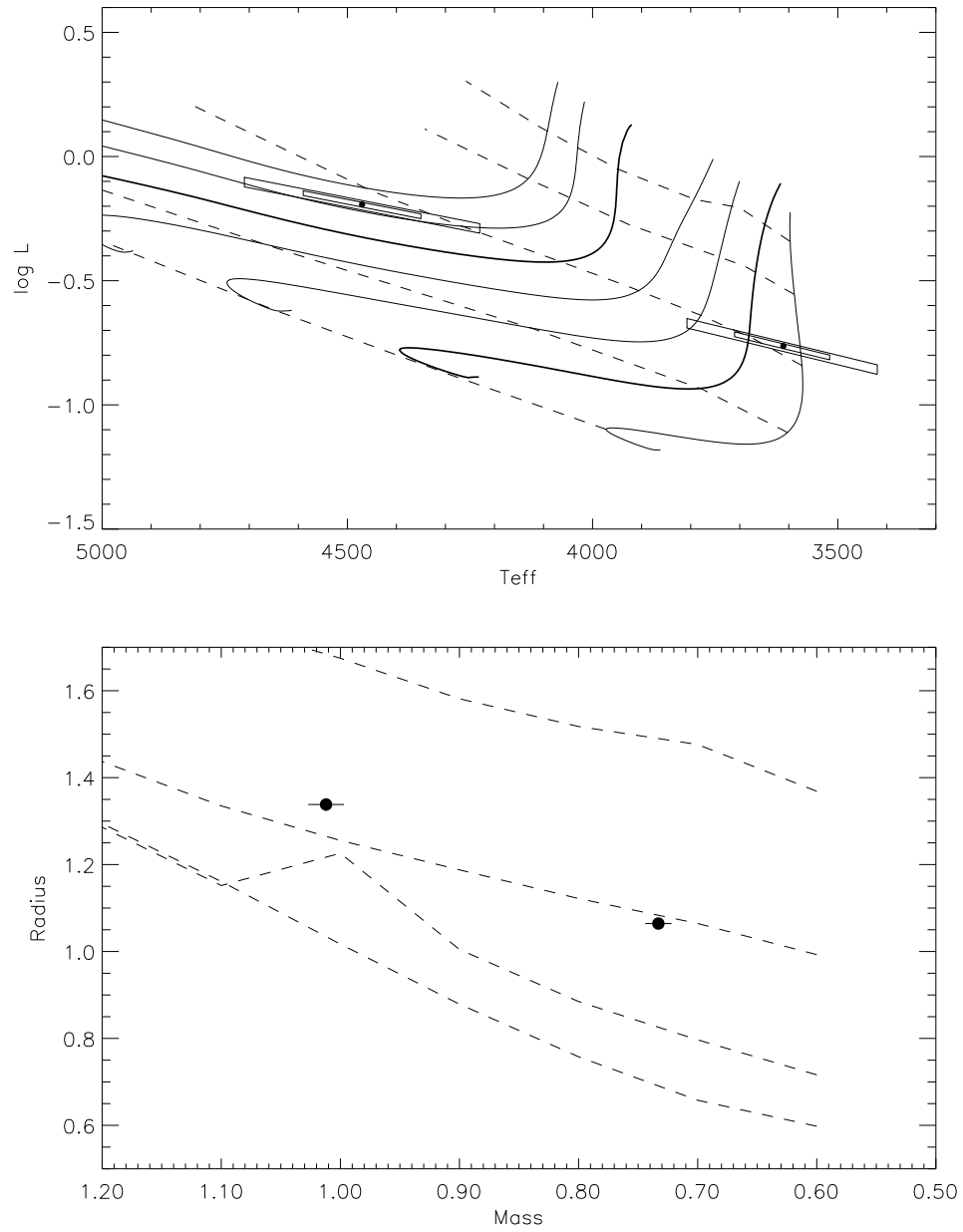


Fig. 20.— Montalbán et al. (2003) tracks with MLT convection ($\alpha_{\text{in}} = 1.0$, $\tau_{\text{ph}} = 3$) and NextGen atmospheres from Hauschildt, Allard, & Baron (1999). Symbols and lines are as in Fig. 16.

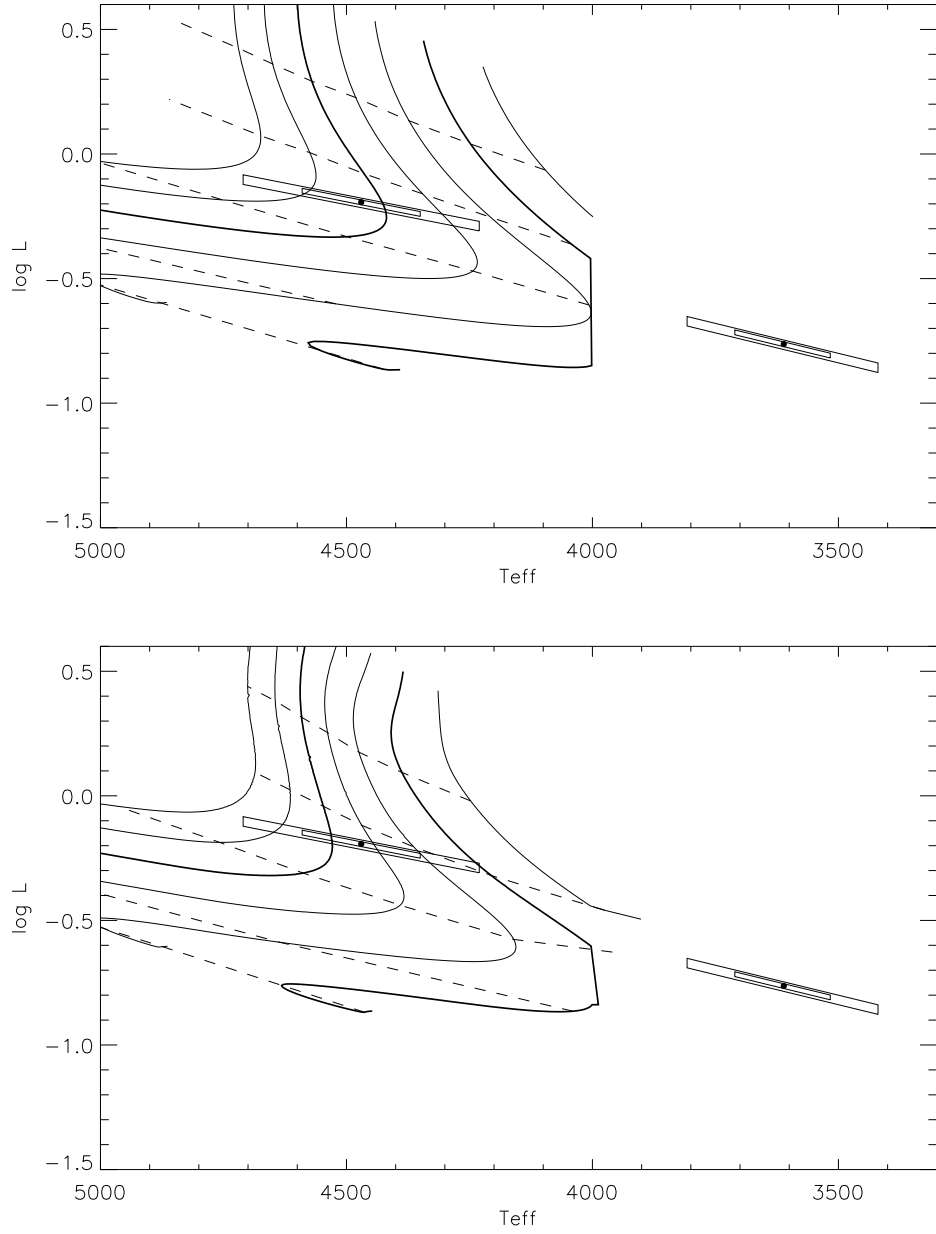


Fig. 21.— Montalbán et al. (2003) tracks with (a) MLT convection ($\alpha_{\text{in}} = 2.3$) and (b) FST convection. Both use the ATLAS9 atmospheres from Heiter et al. (2002). Symbols and lines are as in Fig. 16. Note that the tracks are truncated below 4000 K as the Heiter et al. (2002) atmospheres do not extend to cooler temperatures.

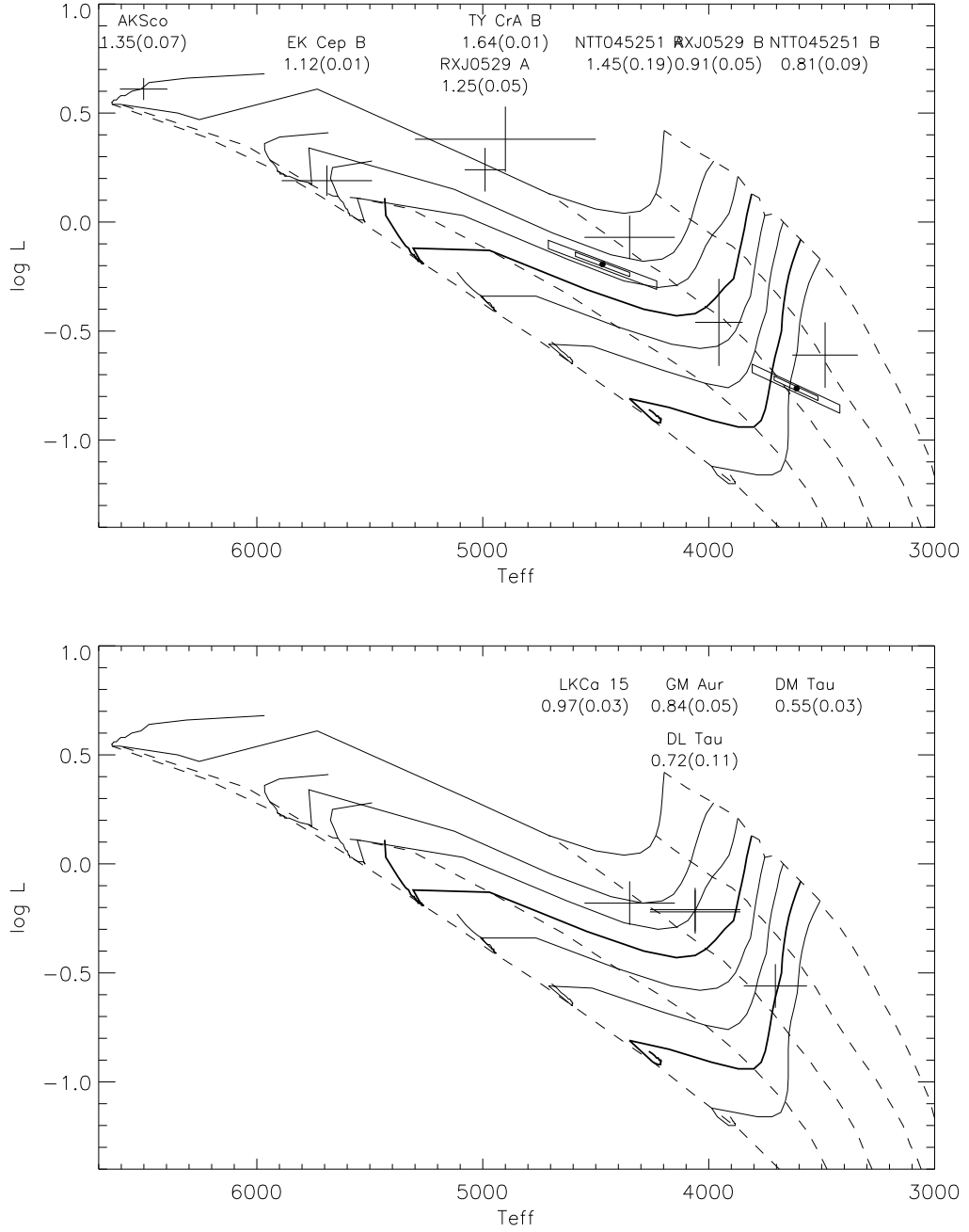


Fig. 22.— Comparison of all PMS stars with accurate empirical mass determinations and $M \lesssim 1.6 M_{\odot}$ with the tracks of BCAH98, $\alpha_{\text{in}} = 1.0$. (a) Stars in binary systems. Masses for each of these are indicated at the top of the figure. Mass tracks shown are for 0.6, 0.7, 0.8, 0.9, 1.0, 1.1, 1.2, and 1.4 M_{\odot} . (b) Same as above, but for single stars. Note that the uncertainties on the masses of the single stars do not include distance uncertainties, which can amount to $\sim 15\%$ (Simon, Dutrey, & Guilloteau 2000).

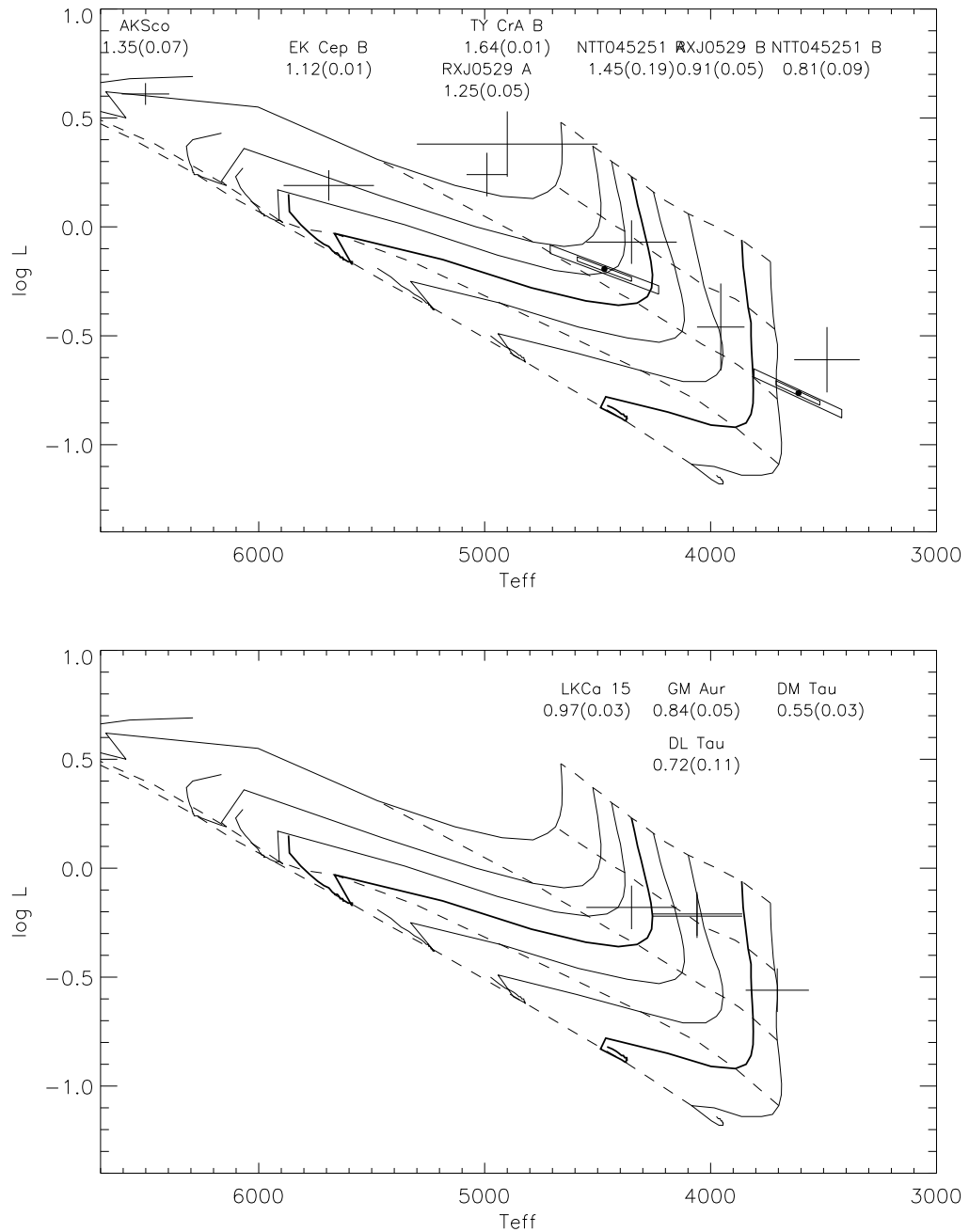


Fig. 23.— Same as Fig. 22 but for $\alpha_{\text{in}} = 1.9$ tracks.

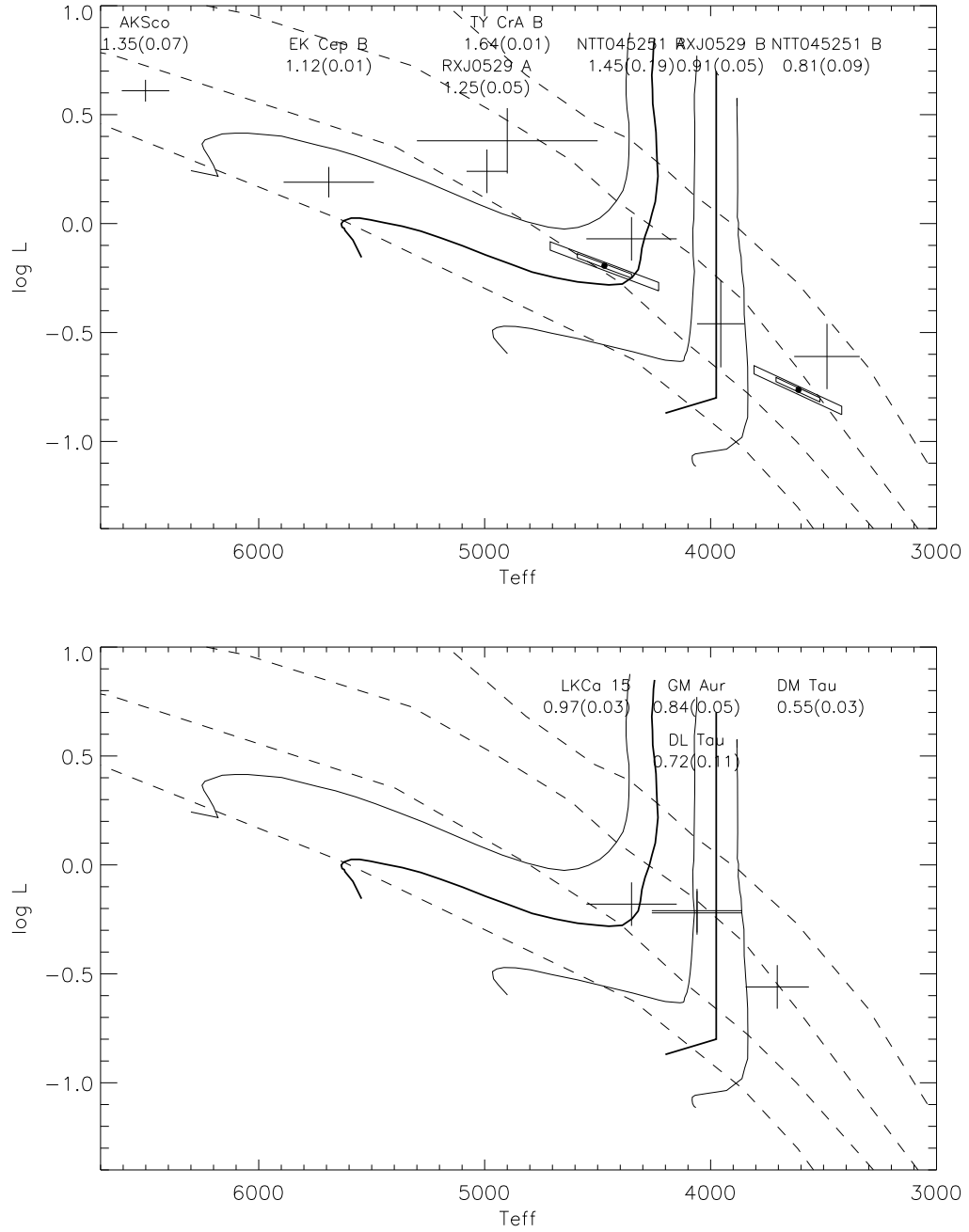


Fig. 24.— Same as Fig. 22 but for PS99 tracks. Mass tracks shown are for 0.6, 0.7, 0.8, 1.0, and 1.2 M_{\odot} .

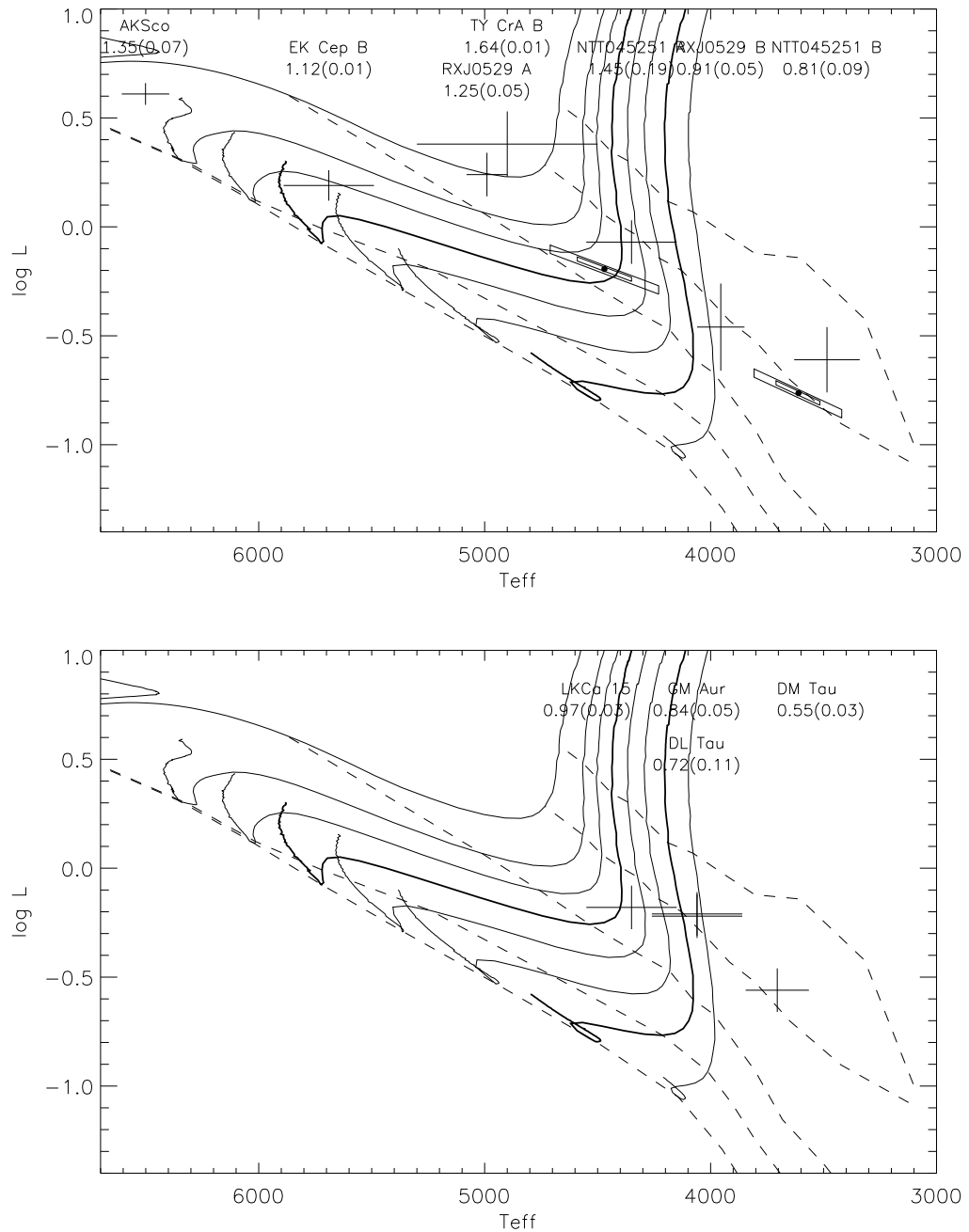


Fig. 25.— Same as Fig. 22 but for SDF00 tracks.

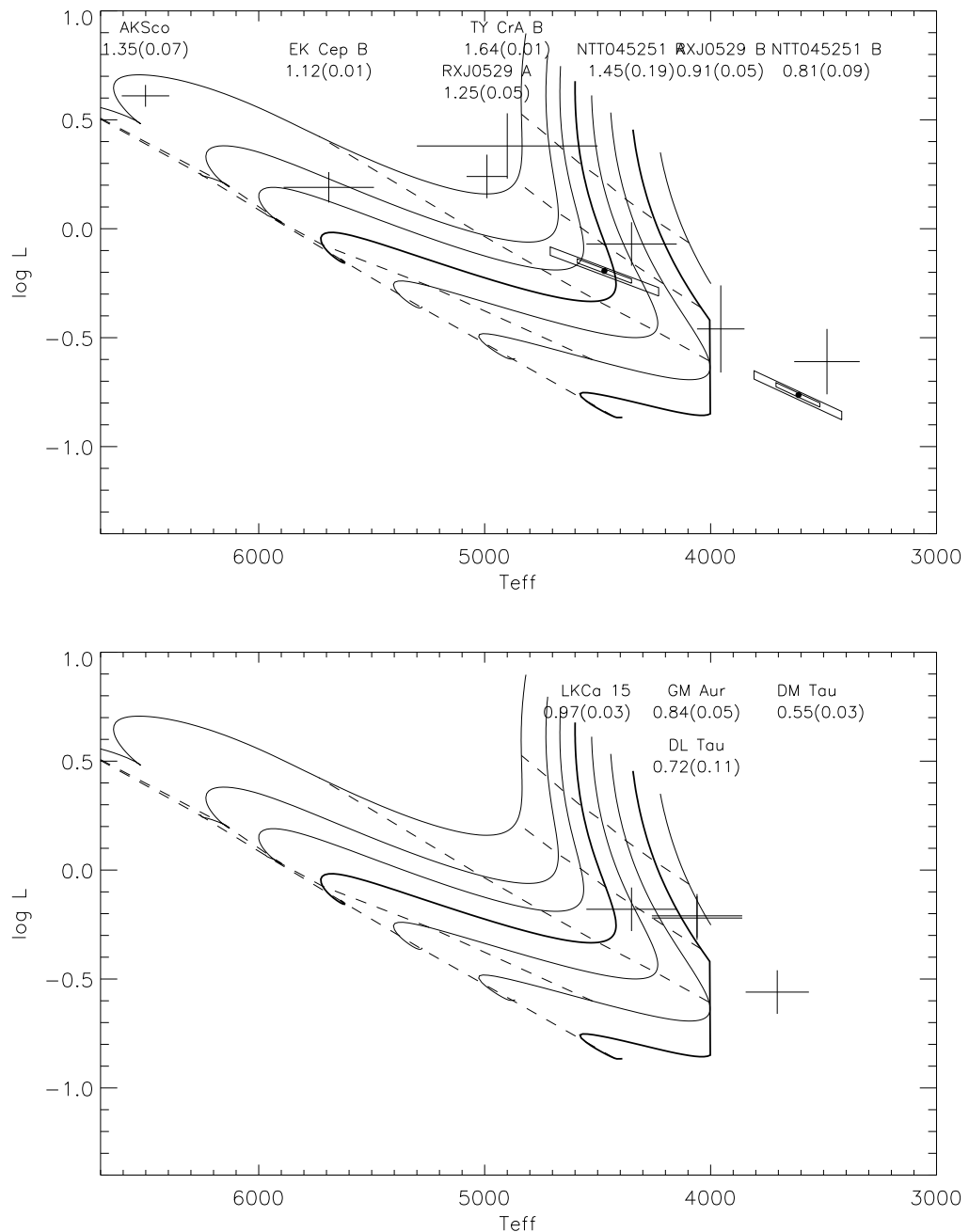


Fig. 26.— Same as Fig. 22 but for MDKH03 MLT ATLAS9 tracks.

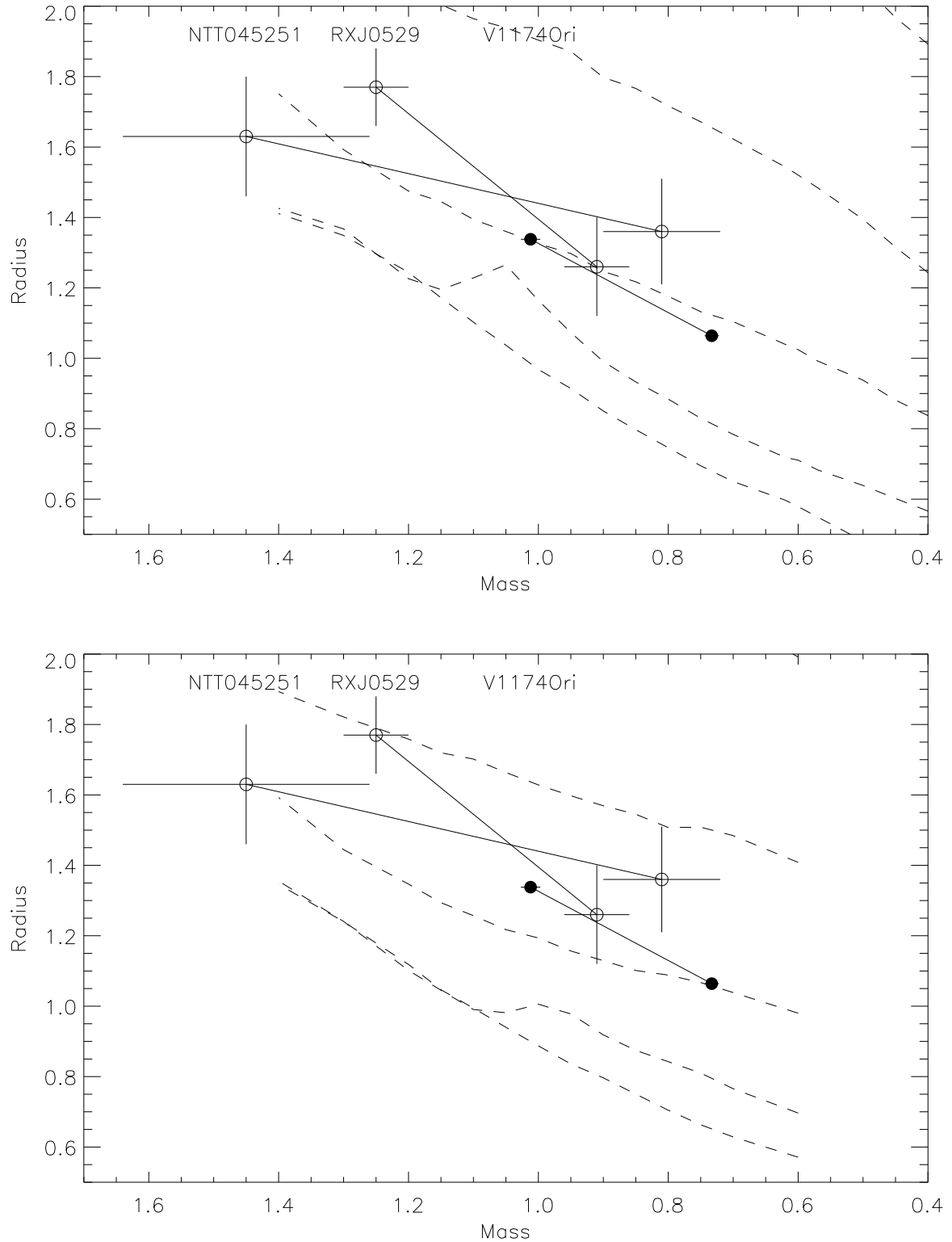


Fig. 27.— Mass-radius relationships (solar units) compared to BCAH98 tracks with $\alpha_{\text{in}} = 1.0$ (top) and $\alpha_{\text{in}} = 1.9$ (bottom).

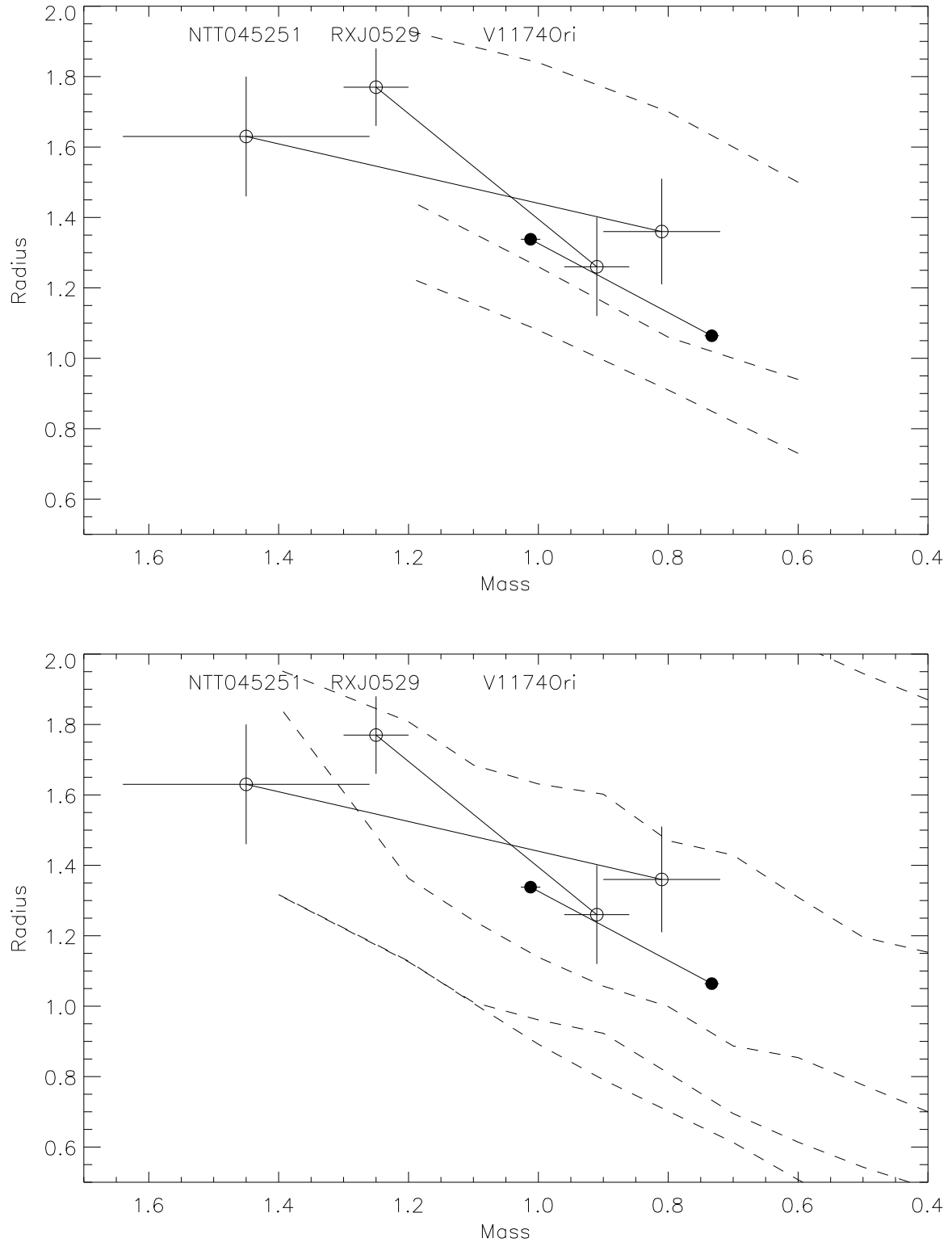


Fig. 28.— Same as Fig. 27 but for PS99 and SDF00 tracks.

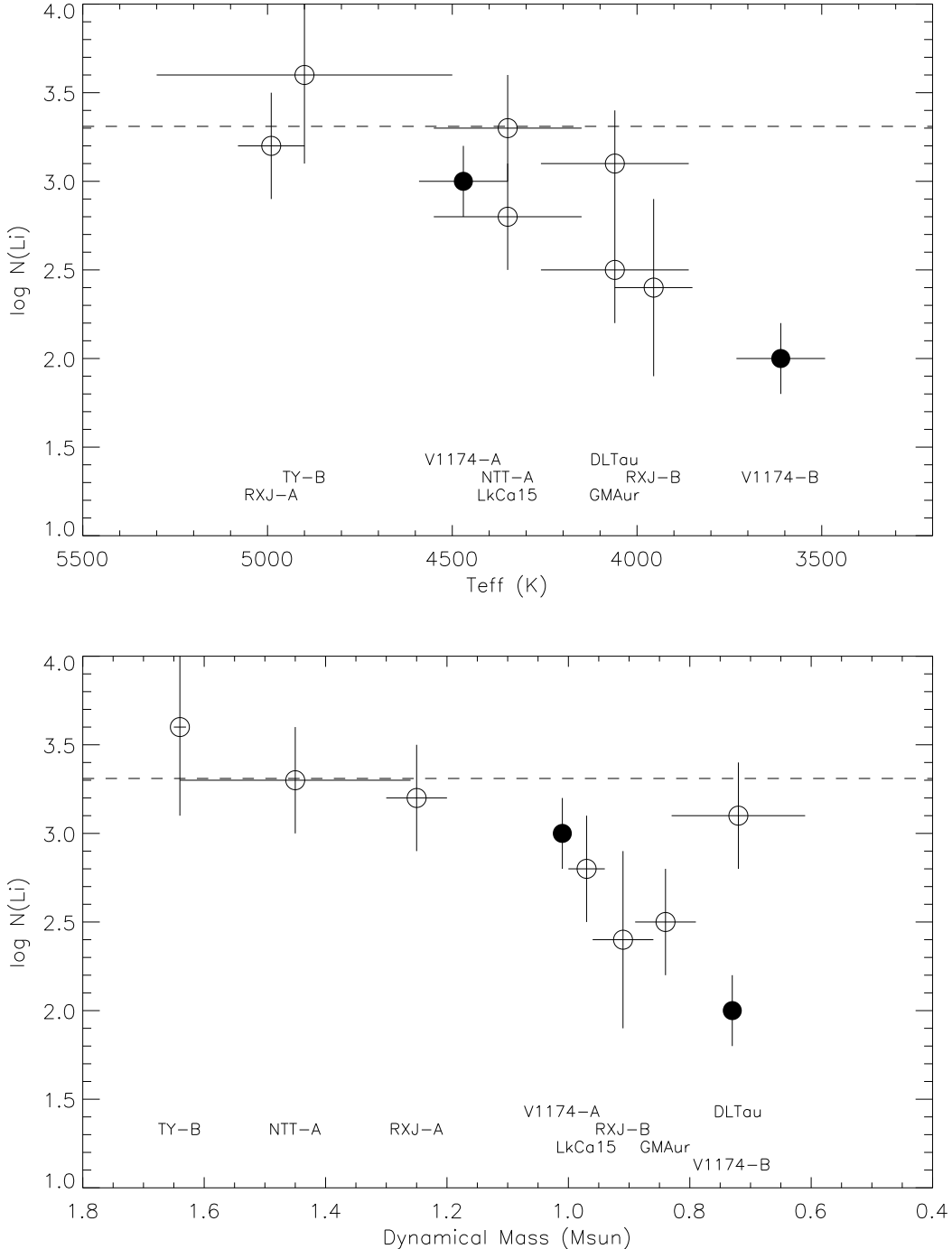


Fig. 29.— Li abundances of PMS stars with empirical mass determinations. (a) Li abundance plotted as a function of stellar T_{eff} (K). The two components of V1174 Ori are shown as filled circles, other stars are shown as open circles. (b) Li abundance plotted as function of empirical stellar mass (solar units). In both plots, the “cosmic” Li abundance of 3.31 is indicated by the horizontal line. Abundances are calculated from the observed Li equivalent widths, using the NLTE curve-of-growth calculations of Pavlenko & Magazzu (1996). References for the equivalent width measurements are as follows: V1174 Ori (this study); RXJ0529.4+0041 (Covino et al. 2000); NTT 045251+3016 A (Walter et al. 1988); TY CrA B (Casey et al. 1998); LkCa 15 (Martín et al. 1994); GM Aur (Basri, Martín, & Bertout 1991); and DL Tau (Basri, Martín, & Bertout 1991).